Thesis for the degree
Doctor of Philosophy

Submitted to the Scientific Council of the
Weizmann Institute of Science
Rehovot, Israel

עבודת גמר (תזה) לתואר
דוקטור לפילוסופיה

מוגשת למועצה המדעית של
מכון ויצמן למדע
רחובות, ישראל

By
Andrea Tesi

מאת
אנדראה טזי

פיתוח קונספטים חדשים של קריאת אור ומטען עבור גלאי חלקיקים מבוססי ארגון נוזלי

Development of novel light and charge readout concepts for liquid argon particle detectors

Advisor:
Dr. Shikma Bressler

מנחה:
שקמה ברסלר

September 2023

תשרי תשפ״ד

Contents

1 List of abbreviation

Acronyms

μ-CT Micro-computed Tomography. 39, 41, 42, 44, 83

ABS Acrylonitrile Butadiene Styrene. 55, 56, 71, 72, 74, 94, 95

CF4 Tetrafluoromethane. 16

CNT Carbon NanoTubes. 55, 74, 84

CsI Cesium Iodide. 16–18, 22, 83, 86

DHCAL Digital Hadron Calorimetry. 19, 20, 86

DLC Diamond-like Carbon. 45–50, 58, 68, 69, 71, 74, 76, 84

DM Dark Matter. 9, 10, 12, 17

DP Dual-Phase. 9, 10, 14, 17, 19, 34, 36, 71, 83, 84

DUNE Deep Underground Neutrino Experiment. 9, 10

EL Electroluminescence. 9, 10, 14–16, 18, 22, 23, 25, 26, 28, 29, 44, 84–86

FR4 Epoxy Fiberglass. 34–36, 39–41, 44, 46, 47, 49, 50, 90, 91

GEM Gaseous Electron Multiplier. 16–18, 44, 85, 86

GPM Gaseous Photo-Multiplier. 9, 16

HV High Voltage. 41, 59

IVC Internal Vacuum Chamber. 20, 21

LAr Liquid Argon. 8–10, 12, 14, 19–22, 24–29, 35, 36, 39, 44, 61, 68, 71, 81, 83, 85

LEM Large Electron Multiplier. 10, 16, 17, 19, 57, 71, 81, 82, 84

LHM Liquid Hole Multiplier. 17, 18, 20, 22–30, 36, 44, 83, 85, 86

LKr Liquid Krypton. 14

LN_2 Liquid Nitrogen. 46–52, 55

LXe Liquid Xenon. 8, 12–14, 22, 25, 26, 29, 44, 83

MPGD Micro-Patterned Gaseous Detectors. 17, 45, 56

Ne Neon. 16

NL Noble Liquid. 8–11

OVC Outer Vacuum Chamber. 20, 21

PDE Photon Detection Efficiency. 83

PETG PolyEthylene Terephthalate Glycol. 55, 56, 71, 72, 74, 95

PMT Photo-Multiplier Tube. 9, 22–28, 81, 84

RHI Relativistic Heavy-Ion. 8

RPWELL Resistive Plate WELL. 17, 19, 20, 56–58, 60, 61, 63, 64, 70–75, 83–85, 92–95

RT Room Temperature. 49, 52, 55, 83

RWELL Resistive WELL. 17, 19, 20, 56, 57, 60–62, 66–81, 83, 84

S/N Signal-to-Noise. 17, 70

SC Single Conical. 44, 86

SiPM Silicon Photo-Multiplier. 9, 18, 22–25, 29, 44, 83, 85, 86, 95

THGEM Thick Gaseous Electron Multiplier. 10, 16–19, 22, 23, 25, 26, 28–31, 43, 44, 56–58, 60–64, 71, 72, 74, 75, 81–85, 87, 90–92

THWELL Thick WELL. 17, 56, 57, 59, 61, 63, 71, 72, 74, 75, 82, 84

TPB TetraPhenyl Butadiene. 23–25, 81, 84

TPC Time Projection Chamber. 8–10, 13, 14, 17, 19, 61, 71, 83, 85

VUV Vacuum UV. 12, 17, 18, 61, 86

YSZ Yttrium-Stabilized-Zirconium. 20, 51, 53, 54, 74, 76, 84

2 Ackowledgements

I would like to express my heartfelt gratitude to all those who supported and assisted me throughout my Ph.D. journey.

In primis, I would like to thank my supervisor, **Dr. Shikma Bressler**, for granting me the opportunity to participate in a cutting-edge research project in radiation detection physics and **Prof. Amos Breskin**, for his unwavering guidance, support, and dedication - without their expertise and encouragement, the success of this work would not have been possible. I am particularly indebted to **Dr. Luca Moleri** for his invaluable assistance and countless hours spent together in the laboratory, as well as for engaging and meaningful conversations. I am also grateful to **Dr. David Vartsky** for being a great research partner and an excellent guide.

I would like to extend my appreciation to all my former and current lab colleagues and mates: **Dr. Sergei Shchemelinin**, **Dr. Artur Coimbra**, **Dr. Itamar Israel**, **Dr. Michael Pitt**, **Dr. Arindam Roy**, **Dr. Purba Bhattacharya**, **Dr. Dan Shaked-Renous**, **Dr. Eran Erdal**, **Dr. Gonzalo Martinez-Lema**, **Dr. Abhik Jash**, **Dr. Marina Borysova** and **Dr. Ryan Felkai**. Their insightful conversations and steadfast support have been instrumental throughout this journey. I am deeply grateful to **Ms. Darina Zavazieva** for her continuous support and for being an amazing friend.

I would also like to acknowledge my Spanish collaborators **Sara Leardini** and **Dr. Diego Gonzalez-Diaz** for all the insightful discussions and contributions that deeply influenced the success of this work.

Special appreciation goes to **Yehuda Asher** for his support, knowledge, and guidance in all mechanical aspects, to **Yigal Shachar** for his priceless help during emergency situations in the lab and to **Dr. Enrico Segre** for his assistance with simulations.

To the best administrative team that I could have ever imagined: **Hemda Atziz**, **Revital Ackler**, **Merav Basson**, **Natalya Leybovich**, **Nina Feldsohn**, **Hila Shtudiner**, **Yuri Yagudaev** and **Amir Bar-On**, for their precious assistance, for all the laughs and unique moments we spent together.

To my Israeli family, the best I could have ever dreamed of, **Robin**, **Amos**, **Barbara**, and **Albert**, and to all the friends that were part of this journey. And finally to my mother **Monica**, for always being with me from very far away.

3 Declaration

I hereby declare that this presented work summarizes my independent research.

The entire work was conducted in collaboration with colleagues from the Weizmann Institute of Science. In particular with Dr. Purba Bhattacharya, Dr. Eran Erdal, Dr. Abhik Jash, Dr. Luca Moleri, Dr. Enrico Segre, Dr. Dan Shaked-Renous and Dr. David Varskty.

The work on the cryogenic RWELL and on the cryogenic RPWELL was developed in collaboration with our colleagues Dr. Diego Gonzalez-Diaz and Sara Leardini from the University of Santiago de Compostela, Spain.

4 Abstract

Over the course of the past couple of decades, significant advancements have been made in the field of noble-liquid detectors. Particularly notable are the applications in the domains of neutrino physics and the exploration of dark matter. When particles interact within noble liquids, they produce distinct signatures in the form of light and charge, capable of traversing great distances with minimal losses. This high property, coupled with their exceptional density and potential for expansion, render noble-liquid detectors highly sought-after for experiments necessitating substantial target masses, negligible background interference, position reconstruction, and high sensitivity to low-energy radiation deposits. The most advanced version of these detectors is the dual-phase Time Projection Chamber (TPC), although concerns persist regarding the scalability of the various signal readout technologies associated with TPCs, particularly in the context of forthcoming multi-ton experiments (Darwin 50 ton LXe, DUNE: 100's of Kton).

The first part of this thesis work revolves around the innovative concept of the Liquid Hole Multiplier (LHM). The LHM represents a single-element sensor designed to simultaneously detect radiation-induced ionization charges and scintillation light within a noble-liquid detection medium. The underlying principle involves harnessing the phenomenon of electroluminescence (EL) generated in a gas bubble that is confined beneath a perforated electrode coated with Cesium Iodide (CsI) and submerged in the noble liquid. This enables the detection of both ionization electrons and UV-induced photoelectrons, opening up new possibilities for comprehensive radiation detection and analysis. In the second part, two additional concepts for charge multiplication, known as the cryogenic Resistive WELL detector (RWELL) and the cryogenic Resistive Plate WELL detector (RPWELL), were explored. Novel resistive materials, thin films (DLC) or plates (ceramics, thermoplastics), have been engineered for operation at cryogenic temperatures and incorporated into the detector assemblies. It was demonstrated, for the first time at liquid argon temperature, that embedding resistive materials into the detector assemblies results in a performance upgrade and in a protection against electrical instabilities.

5 Introduction

Noble liquid (NL) detectors have rapidly emerged as the leading technology for rare-event detection. Their wide-ranging applications encompass crucial scientific endeavors such as neutrino experiments [1], dark matter searches, and the investigation of rare phenomena like neutrino-less double beta decay [2], proton decay [3], and $\mu \rightarrow e\gamma$ decay [4]. These detectors have also found practical use in the medical field, where they have been employed as Compton medical-imaging cameras [5]. Furthermore, their potential extends to the civil sector, with proposals for gamma and neutron radiography applications to bolster homeland security measures [6–8]. The prominence of NL detectors stems from their unique properties. Particle interactions within these liquids induce significant light and charge signals that can propagate across vast distances with minimal degradation. This advantageous property, combined with the high density offered by noble liquids and their scalability, makes them the preferred choice for constructing large-volume experiments. NL detectors exhibit exceptional performance, boasting ultra-low background noise, precise positioning, and energy resolution, and remarkable sensitivity of some to low-energy depositions [9]. Their versatility and efficacy make them indispensable tools for advancing scientific research and addressing critical challenges in various fields.

5.1 The Time Projection Chamber (TPC)

The Time Projection Chamber (TPC), introduced by Nygren in the 1970s, is an advanced particle detection and tracking device used in the field of high-energy particle physics [10]. Its development was driven by the need to accurately measure and reconstruct in 3D the trajectories of charged particles produced in high-energy particle collisions to study the fundamental building blocks of matter. A TPC consists of a gas-filled chamber with sensitive electron multipliers that record the ionization produced by charged particles passing through the gas. As particles traverse the chamber, they create a trail of ionized gas atoms and electrons. The latter drift toward readout planes under an electric field. By measuring the 2D position and arrival time of these ionization signals, the TPC can reconstruct the particle tracks in three dimensions. Over the years, the TPC technology has evolved and improved, with advancements in detector materials, electron multipliers, electronics, and data analysis techniques. Modern TPCs have achieved impressive spatial resolution and particle identification capabilities, enabling scientists to precisely measure particle properties, such as momentum, energy loss, and particle identification, in complex particle collision events. The widespread adoption of TPCs in particle-physics and relativistic heavy-ion (RHI) experiments has contributed significantly to advancements in our understanding of fundamental particles and their interactions. In addition to the conventional gas-based TPCs, there have been significant advancements in TPC technology utilizing particularly NL, such as liquid argon (LAr) and liquid xenon (LXe). NL in TPCs provide several advantages. First, they have high density, making them excellent for precise energy

measurements and efficient particle identification. Additionally, these liquids have low ionization thresholds and excellent scintillation properties that allow for excellent spatial resolution, enhancing the accuracy of particle track reconstruction. NL-TPCs have been successfully deployed in various physics experiments, including neutrino oscillation studies [11], dark matter searches [12], and other rare event searches [13]. Notable examples include the LAr-TPCs used in the Short-Baseline Neutrino (SBN) program and the Deep Underground Neutrino Experiment (DUNE) [14]. The Xenon TPC (Xe-TPC) technology has been employed mostly in experiments; the most relevant are XENON, LUX, PandaX and the forthcoming Darwin 50-ton [15]. NL TPCs can be implemented in either single-phase or DP configurations.

Single-phase TPC The single-phase NL-TPC (depicted in Fig. 1, left) consists of a uniform volume of the noble liquid. Ionization electrons created by charged particles in the liquid medium drift towards and are directly detected by two parallel-wire readout planes immersed in the liquid. They drift towards and are collected at the second readout plane, without charge multiplication. The XY event position can be reconstructed by looking at these charge signals. The time elapsing between the particle-induced primary scintillation signal (S1) and the charge signal provides the Z coordinate, by knowing the drift velocity. This signal is usually referred to as "S2". Various experiments such as ICARUS [3], MicroBooNE [16], and DUNE [17] are based on this detection scheme where a comprehensive characterization of the interaction products and calorimetry are desired. Note that single-phase TPCs can detect only large charge deposits (e.g. by neutrino-induced muons). Without charge and/or light amplification, they are not suitable for DM searches.

Dual-phase TPC In a DP NL-TPC, the detector consists of two distinct regions: a liquid phase and a saturated vapor phase located above it. Two schemes of operation can be adopted: EL or charge multiplication. In the first case, see Fig. 1 middle, radiation-induced ionization electrons drift in the NL and are extracted into the gaseous phase where they undergo EL ("S2" signal) in a parallel gap [18]. EL photons are recorded by photosensors like vacuum photomultiplier tubes (PMT) [9] or solid-state based multi-pixel photon counter (MPPC, also referred to as silicon photomultiplier – SiPM) [19] thanks to their high single photon sensitivity and photon detection efficiency. Amongst other technologies are the avalanche photodiodes (APD) [20] and the cryogenic gaseous photomultiplier (GPM) [21, 22]. The XY position of the event is reconstructed according to the hit pattern on the top array of photosensors; the Z coordinate is calculated using the time difference between the S1 and the S2 signals. The DM experiments based on the DP technique are XENON1T [23], LUX [24] and Panda-X [25] using liquid xenon (LXe), and ArDM [26] and DarkSide [27] using liquid argon (LAr). In the second case, see Fig. 1 right, the electrons are collected into the holes of a perforated electrode where

they undergo avalanche multiplication. The amplification structure is called Large Electron Multiplier (LEM) and it is identical to a Thick Gas Electron Multiplier (THGEM) discussed below [28]. Multiplied electrons are detected electronically [29] and allow for low-energy detection thresholds compared to single-phase TPCs. In neutrino experiments, ~5,000 e^-/mm can be generated in LAr by a minimally ionizing particle, at 0.5 kV/cm [3], while in dark matter (DM) searches, given the low energies involved, a minimal number of detectable electrons are expected making this option not viable.

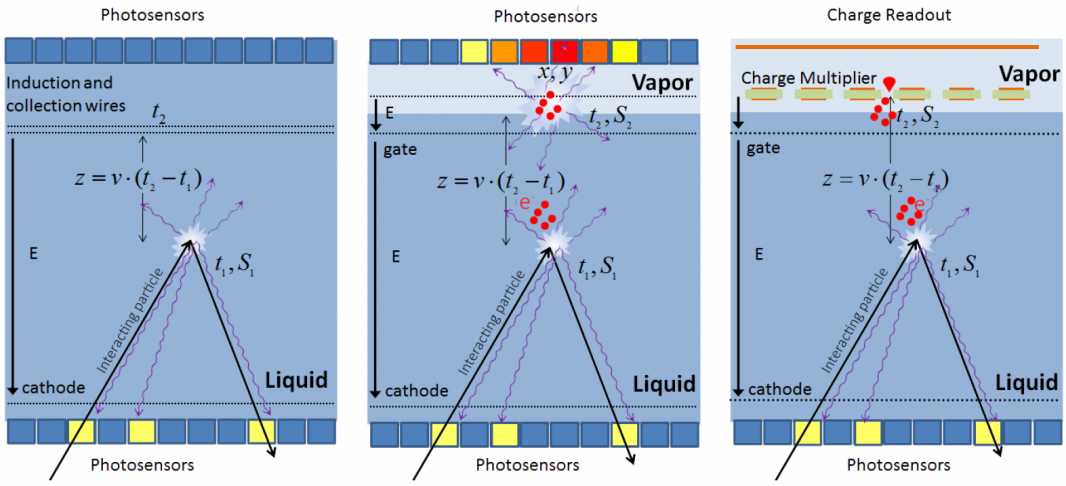

Figure 1: Operation principle of NL-detectors. Particles interacting in the detector leave a cloud of ionization electrons and scintillation photons in the liquid. The latter are recorded on two arrays of photosensors at the top and at the bottom of the cryostat. **a)** Single-phase TPC: electrons drift upwards to XY wire planes inducing signals (no multiplication). The Z coordinate is derived from the time difference between the primary scintillation and the charge signal. **b)** DP-TPC: electrons drift to and are extracted from the liquid to the gaseous phase and they induce EL in a high electric field. Photons are recorded by the top array of photosensors used in XY and the depth is derived from the time. **c)** DP-TPC with charge amplification and readout in the vapor phase with a perforated electrode (LEM, THGEM). Picture taken from [30].

Next generation detectors Scaling up of NL-detector size, although a well-motivated natural step-forwards from the physics point of view, poses technological challenges from the points of view of construction, reliable operation, and signal readout [17, 31]. Specifically, scaling up detector size necessarily causes a reduction in the detectable radiation-induced scintillation-light and charge signals, causing an increase in the intrinsic noise of the readout thus affecting the signal-to-noise ratio. Combining these with the cost of today's state-of-the-art ultra-sensitive light sensors and low noise charge readout, one is highly motivated to look for new solutions and concepts for future large-scale experiments [32]. The flagship experiment of neutrino physics, DUNE [17], plans to reach 150 kton of liquid argon. The design will include three modules based on single-phase TPC with wire readout and a fourth, with a vertical-drift single-phase TPC. The original idea of adopting a DP-TPC was discarded due to technical problems resulting in severe charge

gain limitations [33].

5.2 Physics of noble liquid TPCs

Interaction with the noble liquid The interaction of particles and radiation in NL detectors results in the production of charged particles, ionization, and excitation. The primary interaction mechanism varies depending on the particle, its energy, and the cross-section for different processes. In the case of photons, their interaction with matter predominantly occurs through photoelectric absorption, Compton scattering, or pair production processes [34]. All these three processes, as a final outcome, culminate in the emission of an electron in the liquid volume. Neutrons, instead, primarily interact by scattering off the nuclei present in the liquid [23]. Interactions can be elastic (nuclear recoil) and inelastic, for energies in the MeV scale or higher. As detailed in [17], neutrinos can exhibit different interaction channels depending on their flavor and energy. Specifically, GeV-scale electron neutrinos (ν_e) predominantly interact via three main channels:

- Elastic scattering off electrons: In this process, the electron neutrino scatters off an electron within the medium without changing its flavor. This type of interaction typically involves a transfer of momentum and energy;
- Charge current interaction resulting in inverse beta decay: this interaction occurs when the electron neutrino undergoes a charge current interaction with a nucleus, leading to an inverse beta decay process. The neutrino is absorbed by a nucleon, transforming it into a neutron and emitting a positron.
- Neutral current interaction resulting in a π^0 decay: in this scenario, the electron neutrino undergoes a neutral current interaction with a nucleus. This interaction can lead to the production of a neutral pion (π^0), which subsequently decays into two gamma particles. These gamma particles then go on to interact with the noble liquid at a distance from the original interaction point.

On a separate note, Weakly Interacting Massive Particles (WIMPs), which are hypothetical particles investigated in various dark matter experiments, are expected to cause elastic low-energy nuclear recoils within the noble liquid. This recoil phenomenon arises from the interactions between WIMPs and the NL nuclei.

As charged particles are emitted during the primary interaction, they traverse through the medium, leaving behind a trail of energy deposition in the form of ionization and excitation. The average energy loss per unit distance experienced by charged particles along their path was initially characterized by the Bethe-Bloch formula [35]:

$$< \frac{dE}{dx} >= -\frac{4\pi}{m_e c^2} \cdot \frac{nz^2}{\beta^2} \cdot (\frac{e^2}{4\pi\epsilon_0})^2 \cdot [ln(\frac{2m_e c^2\beta^2}{I \cdot (1-\beta^2)}) - \beta^2] \tag{5.1}$$

where m_e is the electron rest mass, c is the speed of light, n is the mean electronic density, β is the relativistic velocity and I is the mean excitation potential. The energy loss depends directly only on β, this implies that different particles traveling in the liquid with the same energy will show different ionization patterns. This is relevant for particle identification and background suppression in noble liquid detectors.

Scintillation signal In the absence of an external electric field, the electrons liberated by the decelerating charged particle recombine with the ions and the excited atoms return to their ground state. These processes however are not direct and involve a long chain of chemical reactions, the end of which are the formation of excited bound states of two atoms called excimers. Excimers can be formed either in a singlet or in a triplet molecular bound state. The dissociation of the excimer into two neutral atoms is accompanied by the emission of an energetic photon in the VUV range. This light pulse is normally referred to as prompt scintillation or S1 pulse. The processes are shown in detail in Table 1 below from [9].

Ion recombination	**Deexitation**
$R^+ + R + R \rightarrow R_2^+ + R$	$R^* + R \rightarrow R_2^{*,\dagger}$
$e^- + R_2^+ \rightarrow R^{**} + R$	$R_2^{*,\dagger} + R \rightarrow R_2^* + R$
$R^{**} + R \rightarrow R^* + R + \text{heat}$	$R_2^* \rightarrow R + R + h\nu$
$R^* + R + R \rightarrow R_2^* + R + \text{heat}$	
$R_2^* \rightarrow R + R + h\nu$	
(R_2^* - purely electronic excitation)	($R_2^{*,\dagger}$ - excited states including vibrational states)

Table 1: Deexcitation and recombination processes in LAr and LXe. R stands for LAr or LXe atom. Taken from [9].

The timescales for photon emission (i.e. of the excimer dissociation) depend on the molecular bound state (R_2^* in Table 1. Excimers in the singlet state decay faster than those in the triplet state. The wavelengths and relevant time scales for the scintillation processes in LXe and LAr are summarized in Table 2. The ratio of excimers found in the singlet state to excimers in the triplet state is strongly correlated with the ionization density. In principle, the denser the ionization is, the more excimers are found in the singlet state. Specifically in LAr, as can be seen in Table 2, the two emission timescales differ by two orders of magnitude making it easy to measure. Therefore, the primary ionization density can be inferred by measuring the ratio of the long-lived to the short-lived excimers. This effect can be used, for example in LAr-based DM detectors, to distinguish between the densely ionizing nuclear recoils (the signal the detector is looking for) and more sparsely ionizing electronic recoils (background) [27].

	LXe	**LAr**
Liquefaction temperature (@ 1 bar)	165 K [36]	87 K [36]
Scintillation wavelength	175 nm [9]	128 nm [9]
Scintillation timescale (singlet / triplet, E = 0)	34/34 ns [9]	6.5 ns / 1000 ns [9]
Scintillation timescale (singlet / triplet, E ≠ 0)	2.2 ns / 27 ns [9]	5 ns / 860 ns [9]
Refraction index for scintillation wavelength	1.69 [37]	1.36 [38]
Scintillation yield (5.5 MeV α particle, E = 0)	$3.1{\cdot}10^5$ [18]	$2.0{\cdot}10^5$ [18]
Energy gap for electrons: liquid-to-vapor	0.67 eV [9]	0.2 eV [9]
Electroluminescence threshold (vapor @ 1 bar)	1.6 kV/cm [9]	2.1 kV/cm [9]
Electroluminescence threshold (in liquid)	~ 400 kV/cm [39]	~ 3 MV/cm (th) [40]
Charge multiplication threshold (in liquid)	~ 725 kV/cm [39]	~ 7 MV/cm [41]

Table 2: Summary of important physical parameters of LXe and LAr.

Ionization signal When an external electric field is applied, some of the liberated electrons from the primary interaction are able to escape recombination and can be detected. The detection can occur either directly or through an amplification process. The energy deposited during the primary interaction is distributed between scintillation and ionization, resulting in an anti-correlation between the two signals. This anti-correlation between scintillation and ionization signals is utilized in many experiments to more accurately determine the energy deposited in the interaction [9, 18]. The denser the ionization, the lower the fraction of electrons that are able to escape recombination. In the context of WIMP searches based on LXe, this effect is crucial for distinguishing between signals caused by nuclear recoils (resulting in sparser ionization and a lower light-to-charge ratio) and background electronic recoils [23, 31].

The limited diffusion of electrons from the interaction site to the readout region retains the ionization pattern of the event to some extent. By utilizing a charge readout system with spatial resolution, it becomes possible to reconstruct the event topology in the XY plane. Additionally, incorporating the time of arrival information, usually relative to the prompt scintillation signal, and considering the known drift velocity of electrons in the liquid, enables a complete three-dimensional (3D) reconstruction of the event topology. This detection structure is known as a Time Projection Chamber (TPC) and serves as the foundation for most noble liquid detectors utilized today [9, 18].
Understanding the structure of energy deposition, particularly its spatial distribution, offers several advantages in detector applications. Firstly, it enables the calibration of the detector's energy response based on the event location. This information helps to accurately measure the deposited energy in different regions of the detector. Secondly, the knowledge of energy deposition structure allows for the reconstruction of event topology. This capabil-

ity is particularly crucial in experiments using LAr for neutrino studies. By reconstructing the identity, direction, and energy of all outgoing particles following an energetic neutrino interaction, a comprehensive understanding of the event can be achieved [17]. Thirdly, the information about energy deposition structure can be utilized to exclude events based on their location. For instance, in searches for Weakly Interacting Massive Particles (WIMPs) as dark matter candidates, only events occurring within a central volume, known as the "fiducial volume," are considered as potential signal events. Events occurring outside this region are more likely to be background events generated by neutrons [23, 26]. However, not all the free electrons generated at the interaction point are able to reach the readout system. Impurities present in the noble liquid, particularly species with high electron affinity such as oxygen and water, have a tendency to capture these free electrons, converting them into negatively charged ions that drift at a significantly slower pace compared to free electrons. Over a long drift path within the liquid, this leads to an exponential attenuation of the charge signal originating from the interaction point toward the readout. The extent of this attenuation is commonly quantified in terms of "electron lifetime," which represents the time required for a drifting charge to decrease by a factor of 1/e. Continuous purification processes are employed to reduce the concentration of electron-capturing impurities, thereby extending the lifetime of electrons in the liquid. Notably, the XENON1T experiment reported a lifetime of 650 μs in LXe [42], while the protoDUNE demonstrators achieved a lifetime of up to 4 ms [29].

Electrons extraction to vapor phase EL and avalanche multiplication can hardly take place in liquid because they require extremely high electric fields due to their higher density. Threshold values for EL in LXe were reported to be ~400 kV/cm for LXe, higher fields are required for avalanche multiplication [39]. The solution is, therefore, to extract electrons from the liquid phase and transfer them into the gas, where EL and avalanche multiplication are easier to achieve. Regarding the process of electron extraction, when a free charge is present, it polarizes the liquid generating a potential well [43] (note that this behavior is observed in LAr, LKr and LXe but not in liquid neon or liquid helium [43]). The depth of the potential well is 0.2 eV in LAr and 0.69 eV in LXe [9]. So far, several studies were conducted in the context of DP-TPCs to understand better the extraction process. This led to the measurement of the extraction efficiency as a function of the electric field (see Fig. 2 taken from [9]). The time structure was measured by [44] only in LAr showing a slow (few μs) and a fast (less than ns) emission component corresponding to the thermo-ionic emission of cold electrons and to hot electrons heated by the electric field, respectively. No slow component has been observed in LXe and LKr, probably due to the larger potential well ([45]).

Parameter	Ar	Xe
α [V^{-1}]	0.0819	0.137
β [$bar^{-1}{\cdot}cm^{-1}$]	139	177
γ [cm^{-1}]	30.6	45.7

Table 3: EL parameters for Xe and Ar vapor. From [9].

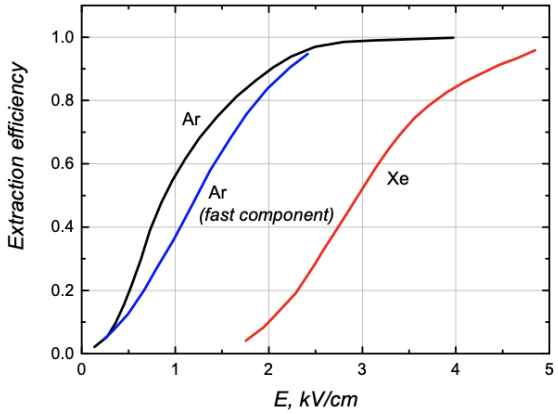

Figure 2: Extraction efficiency of electrons from the liquid phase into the vapor above it, as a function of the electric field in the liquid. Figure taken from [9].

Electroluminescence Once electrons have crossed the interface into the gas phase, EL can occur in the gas phase, under appropriate field intensity. In order for EL to occur, electrons accelerating under the influence of the electric field need to accumulate enough energy between consecutive collisions with the gas atoms to excite the atom they collide onto. EL occurs above threshold field values; the threshold depends on the gas and on its pressure (or density); the photon yield, i.e. the number of photons emitted (to 4π) per unit drift length is given by the following formula [9]:

$$\frac{dN_{ph}}{dx} = \alpha E - \beta P - \gamma \tag{5.2}$$

Where E is the electric field, P is the pressure and the parameters α, β, γ depend on the gas and are given in Table 3.

The EL process is linear with the electric field; the threshold value (E_{th}) can be computed by solving the equation:

$$0 = \frac{dN_{ph}}{dx} \tag{5.3}$$

The total EL yield is then given by the integration:

$$\int \frac{dN_{ph}}{dx} \cdot dx \tag{5.4}$$

along the trajectory of the electrons, and is valid only where the electric field is larger than the threshold field.

5.3 THGEM and WELL-based detectors

The THick Gas Electron Multiplier (THGEM), also referred to as a Large Electron Multiplier (LEM), was introduced in [46–48], as a more robust version of the GEM. See Fig. 3a:

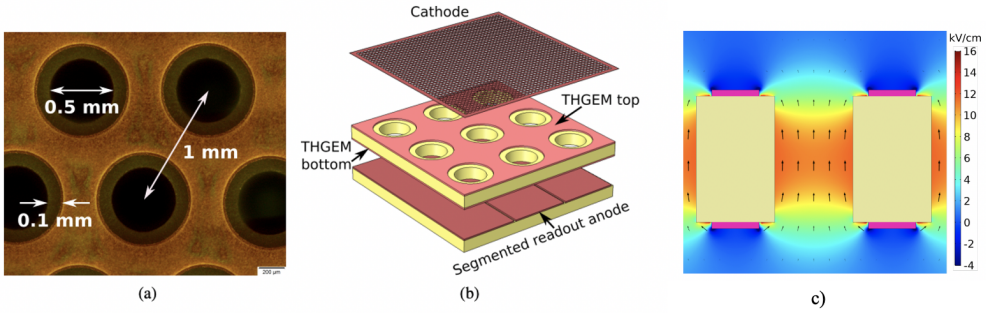

Figure 3: : (a) A THGEM electrode with typical parameters. (b) Schematic of a standard THGEM configuration. (c) Characteristic electric field map of a THGEM electrode for $\Delta V_{\mathrm{THGEM}}$ = 1 kV, induction field E_i = 1 kV/cm, and drift field E_d = 0.5 kV/cm. Arrows represent the field direction. Figures taken from [49].

Its attractiveness derives from the possibility of manufacturing these perforated structures in a relatively economical way. Being simple and robust, THGEM detectors have been the subject of extensive studies and continuous development for various applications requiring radiation detection with submillimeter localization accuracy and a few ns time resolution over a large area [50, 51]. When coated with a photosensitive material (e.g., CsI), the THGEM electrode top face can be used as a photocathode with a relatively small dead area, making these detectors attractive gaseous photomultipliers (GPMs) [51–53]. A standard THGEM-detector configuration comprises a conversion-and-drift gap and an induction gap, followed by a readout electrode, as depicted in Fig. 3b. Fig. 3c depicts the electric field map for the THGEM electrode. In this configuration, the majority of the charge multiplication occurs within the holes. This closed geometry limits photon feedback effects so that stable operation is achieved even in noble gases [54] or highly scintillating ones like pure CF4 [55]. Under the most common conditions, detecting soft x-rays using Ar- and Ne-based gas mixtures at room temperatures, gas gains of the order of several thousand can be reached. The gain in high purity Ar is low, reaching values of a few tens [56]. Besides their most

common operation at standard temperature and pressure, THGEM-based detectors have shown good operation properties from low to high gas pressures [57] and at cryogenic conditions [22, 58, 59]. For applications requiring thinner configurations, the induction gap can be eliminated by directly coupling a THGEM electrode with a metal clad on its top side only to the readout anode in a so-called THick-WELL (THWELL) configuration [60]. Intermediate resistive layers are often deployed to mitigate the detrimental effect of discharges, and this is called Resistive WELL (acrshortRWELL) [60]. When a resitive plate is present, the concept is called Resistive Plate WELL (RPWELL) [61]. The presence of discharges in non-resistive micropattern gas detectors MPGDs can inhibit the detector operation and damage both the electrodes and the readout electronics [62]. Segmented readouts featuring strips and pads were also explored to speed up the charge propagation. Such a variant was called Segmented RWELL (SRWELL) [63, 64]. In the context of neutrino physics, LAr (DP) Time Projection Chamber (TPCs) technology equipped with amplification elements called Large Electron Multipliers (LEMs, also known as THGEMs) in the vapor phase able to improve the detector signal-to-noise (S/N) [65]. Several attempts were made to investigate this technology, amongst them [66–70]. Despite the possibility of amplifying the primary charge, LEMs suffer from the presence of instabilities mostly due to photon feedback effects (discharges, sparks) that can degrade the performance and from a low maximum achievable stable gain [71]. In consideration of such a scenario, the adoption of a spark-protected readout could favorably tackle these weak points and provide a reliable solution for long-time operations.

5.4 PhD projects

This Ph.D. work focuses on the R&D of novel ideas for charge and light detection in future large-volume noble liquid detectors. The Liquid Hole Multipliers (LHM) offer a solution for the combined detection of scintillation light and ionization charge in a single module immersed in the noble liquid, e.g. from DM searches. The cryogenic Resistive WELL (RWELL) and Resistive-Plate WELL (RPWELL) [21] detectors were proposed as a possible solution for stable, enhanced avalanche-gain charge readout in future large-volume dual-phase (DP) argon TPC detectors, e.g. for neutrino experiments.

The Liquid-Hole Multiplier (LHM) project The bubble-assisted LHM is a recent concept, proposed for the combined detection of ionization electrons and primary scintillation photons generated along charged-particle tracks in noble liquids [72–75]. A conceptual scheme of an LHM module is depicted in Fig. 4. It consists of a perforated electrode, e.g., a gas electron multiplier (GEM) [76], or a thick gas electron multiplier (THGEM) [51] immersed inside the noble liquid, with a bubble of the noble gas trapped underneath. The top surface of the electrode is optionally coated with a VUV-sensitive photocathode such as cesium iodide (CsI). Heating elements (such as a plane of heating wires) below the electrode generate the bubble on demand. Once formed, the bubble fills the space below the electrode and remains stable as long as the system is in a thermodynamic steady state,

with buoyancy pushing it upward and surrounding walls confining it from its sides. The top and bottom surfaces of the electrode, as well as the heating wires, are held at different potentials, creating a dipole-like field in the electrode's holes and a transfer field between the electrode bottom and the wire plane. The drift field above the electrode is set by the potential difference between the top surface of the electrode and a distant drift electrode (cathode plane) above. Particle interactions in the liquid lead to a prompt VUV (e.g.125 nm in LAr) scintillation signal (S1) and to the release of ionization electrons. These drift towards the LHM and are focused by the local field into its holes. Once they cross the liquid-gas interface into the bubble, they induce EL light (S2) in the gas, in the high-field region close to the bottom of the hole. Similarly, S1 photons impinging on the photocathode release photoelectrons (PEs); these are focused into the LHM holes, inducing an EL signal (S1') shortly after S1 (and typically long before S2). The S1' and S2 EL signals can be recorded by a position-sensitive photon detector (e.g., a Silicon Photomultipliers, SiPM, array) located below the bubble.

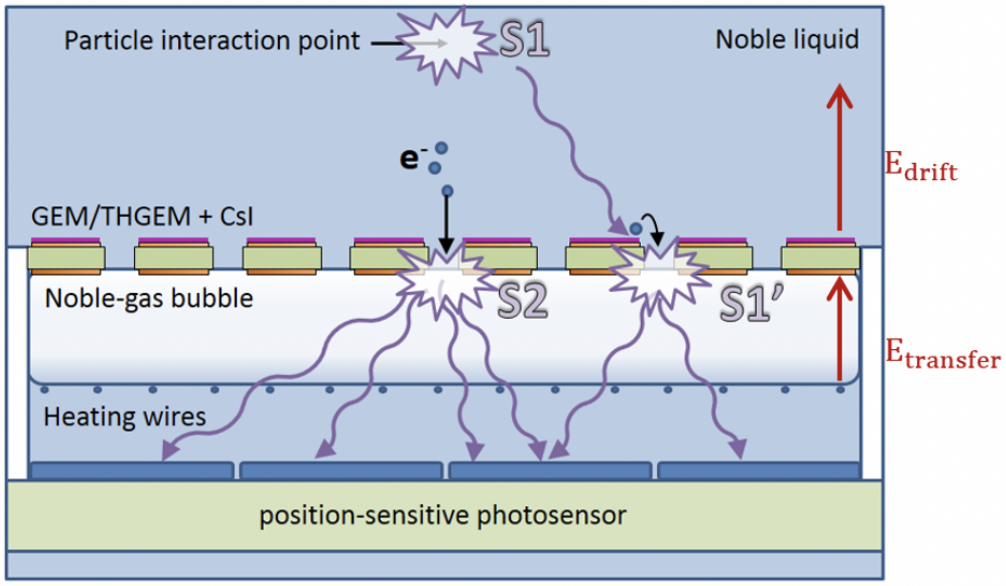

Figure 4: Conceptual scheme for an LHM module, comprising a perforated electrode (e.g., GEM or THGEM) coated on top with a photocathode (e.g., CsI), a grid of heating wires for forming the bubble and a position-sensitive photon detector below. The bubble is supported by buoyancy against the bottom of the electrode. Ionization electrons focused into the holes create EL light (S2) once they cross the liquid-gas interface into the bubble. Primary VUV scintillation (S1) photons impinging on the photocathode release photoelectrons which are focused into the holes and create similar EL signals (S1'). The lateral coordinates of the S2 and S1' signals are reconstructed by the position-sensitive photon detector. Figure taken from [77].

This research work aimed at deepening the understanding of the properties of the bubble-assisted LHM detector in liquid argon.

The Cryogenic RWELL and RPWELL projects The RWELL and RPWELL detectors (see Fig. 5) are a single-stage gas avalanche multiplier combining a single-sided THGEM electrode coupled to the readout anode via a resistive layer or a resistive plate, respectively, in a "well" configuration (the holes closed by the resistive plate form "wells"). Primary ionization charges drift from the ionization volume into the THGEM electrode's holes, where they undergo avalanche multiplication in the high field region. The charge generated in the holes induces a current on the anode. In the RWELL case, the current is evacuated via the resistive layer to the ground; in the RPWELL case, it reaches the anode. As this current increases, the resistance causes a momentary voltage drop at the "head" of the avalanche, thus quenching further multiplication. The RWELL and RPWELL concepts have been developed in our group as a potential sampling element for future digital hadronic calorimeters (DHCAL)[78].

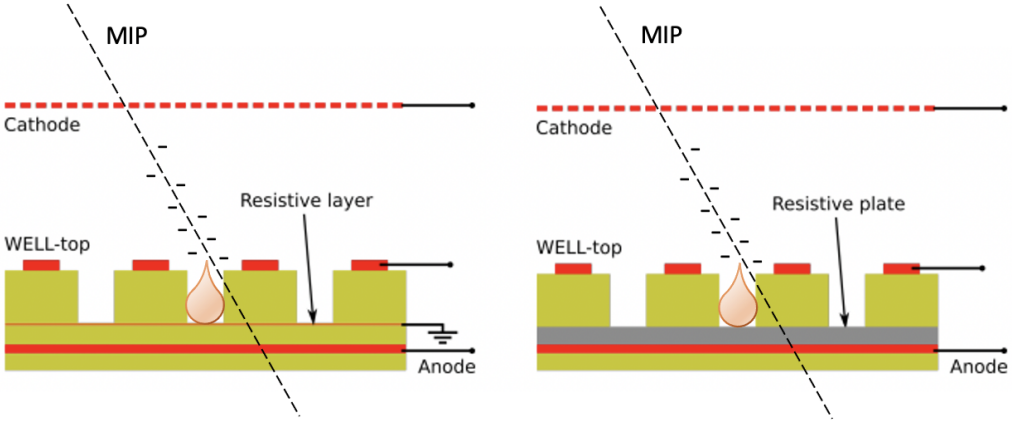

Figure 5: **Left**: scheme of an RWELL detector; **Right**: scheme of an RPWELL detector. Figure taken from [79].

The stability and discharge immunity of these protected charge readouts depend primarily on the resistivity of the plate screening the top THGEM electrode from the anode. A material with too low resistance would exhibit quenching of the discharge's energy but will not prevent it and a material with too high resistivity will result in charging up of the detector leading to significant rate-depending gain variations. These studies of RWELL and RPWELL detectors as possible charge-amplifying elements in DP LAr-TPCs (≈90 K) aim at validating the possibility of reaching more stable, high-gain operation in Ar vapor phase – compared to presently employed THGEM (LEM) elements [28]. These detectors necessitate other appropriate resistive materials.

6 Research Overview

6.1 Liquid Argon Bubble-assisted LHM

The work done during this Ph.D. on the bubble-assisted LHM can be coarsely divided into two subchapters. The first part consists of the main results obtained from the operation of the bubble-assisted LHM in Liquid Argon (LAr), and the second is the study of the physical processes underlying the detector operation.

6.2 Cryogenic RWELL and RPWELL

The work done during this Ph.D. covers the development of the cryogenic RWELL detector. This includes the studies related to the characterization of the resistive layers and the operation of a resistive detector at cryogenic temperature, the investigation of the discharge quenching capabilities, and its performance in comparison to non-resistive readouts.

In the direction of the cryogenic RPWELL, the main results obtained from the characterization of the ceramic (Fe_2O_3-YSZ) resistive plates are reported as well as the in-detector performance. Studies of RPWELL based on 3D-printed materials will also be discussed.

6.3 Extra

In addition, during the Ph.D., I contributed to additional projects whose results were eventually published: i) a systematic study of different electrode geometries and the exploration of the bubble-assisted LHM imaging capabilities in liquid xenon; ii) the operation of a novel single-UV photon RPWELL detector operated at room temperature in $NeCH_4$; iii) the fabrication of a novel sampling element for the DHCAL project based on RWELL and its operation in a dedicated test-beam facility at CERN.

7 Summary of main results

All the experiments were conducted in a dedicated LAr cryostat, WISArD (Weizmann Institute Liquid Argon Detector). The cryostat was composed of an outer vacuum chamber (OVC) and an internal vacuum chamber (IVC), where the latter comprised a 100 mm in diameter, 150 mm tall cylindrical chamber fillable with ~250 ml of LAr. The two elements were separated by an interstitial gap connected to a Turbo Vacuum Pump[1] whose purpose was to provide stable thermal insulation to the IVC from the environment. Three viewports pointing at the assemblies were present, as shown in Fig. 6: the central one, oriented in a perpendicular way, offered the possibility to look at the assembly in a frontal fashion while the other two viewports were respectively above and below the central one and formed an angle with IVC wall of +30° for the superior window and -30° for the inferior one. The rest

[1] PFEIFFER HiCube 80

of the volume was equipped with various sensors, with the detector assembly suspended from the topmost flange where an additional viewport was installed.

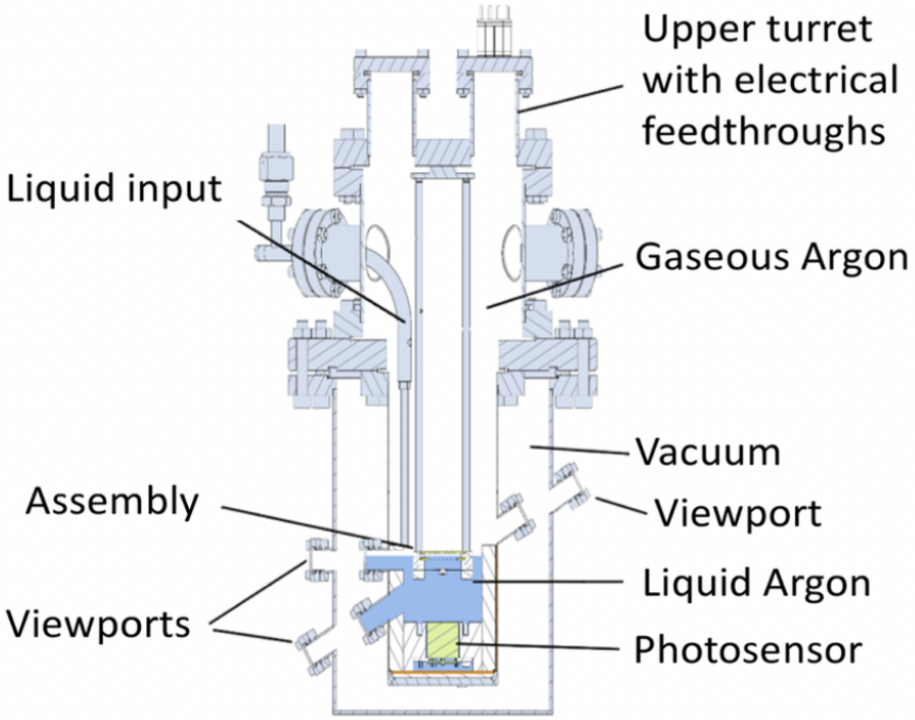

Figure 6: General scheme of Wisard's modified cryostat. An IVC containing liquid Argon is incorporated in an OVC and separated from the latter via an insulation vacuum. Three viewports are present and offer the possibility to inspect the assembly.

Argon liquefaction is done on cooling fins cooled by a pulse tube refrigerator[2]. The temperature of the liquefaction fins is maintained by a closed-loop feedback using a temperature controller[3]. The liquefied argon flows in through a 1.5 m long double-wall, vacuum-insulated transfer tube into the chamber. During operation, LAr is continuously extracted through a tube immersed within the liquid, evaporated, and circulated through a hot getter[4] at 2-5 standard liters per minute. The purified Ar gas returns to the liquefaction fins where it is liquefied and is let to flow back into the chamber. In these conditions, the expected properties of argon are: density of liquid argon ρ_l = 1395.4 kg/m^3, density of gaseous argon ρ_g = 1.784 kg/m^3, surface tension γ = 11.83 mN/m, dielectric coefficient of liquid argon ϵ_l = 1.504, dielectric coefficient of gaseous argon ϵ_g = 1.000516 [80].

[2]Cryomech PT90
[3]CryoCon Model 24
[4]SAES PS3-MT3-R

7.1 Bubble-assisted LHM

7.1.1 First operation of the LAr-bubble-assisted LHM

LHM assembly The LHM detector assembly is described in Fig. 7. It consists of a 0.4 mm thick THGEM electrode (hexagonal holes pattern 0.3 mm in diameter, 0.7 mm apart). In this proof-of-principle study, the THGEM electrode was not coated with CsI, making the detector sensitive only to ionization electrons. An LHM equipped with a THGEM electrode is sub-optimal in terms of light yield and photon detection efficiency. Nevertheless, it was chosen for this first demonstration for its mechanical and electrical robustness. An ^{241}Am alpha source was placed 4.7 mm above the THGEM electrode. The source had an activity pattern of an annulus ~0.5 mm broad and ~3.9 mm in diameter with total activity of ~190 Bq. A grid of heating wires (Ni-Fe, 55 μm in diameter, 2 mm spacing) was placed 1.6 mm below the THGEM. It was used to generate the bubble and to define the "transfer field" ('E_t'), i.e. the field between the bottom face of the THGEM and the wires. Since the cryostat used in this set of measurements did not have a side window allowing for the observation of the bubble (as in previous LXe work [81]), the existence of the latter was inferred from the response of the EL signals to sudden pressure changes.

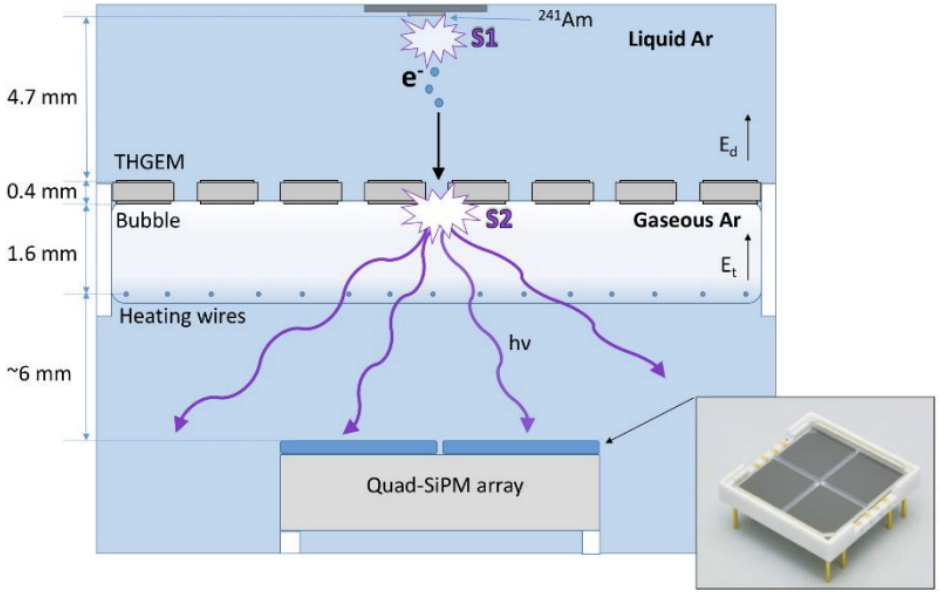

Figure 7: Schematic view of the experimental setup. A 0.4 mm thick THGEM electrode (with 0.3 mm in diameter holes spaced by 0.7 mm) is immersed in LAr; the gas bubble underneath is formed by a grid of heating wires, spaced 2 mm apart, located 1.5 mm below the electrode. Photons were recorded either by a PMT or by a Quad-SiPM array (shown here), located at ~6 mm under the wire grid. Ionization electrons focused into the holes induce EL light (S2) in the bubble; a fraction of the primary scintillation photons (S1) traverses the holes and is detected as well. Figure taken from [82].

Readout of the EL photons was done by direct digitization of the signals from the pho-

tosensors, located ~6 mm below the wire grid, using a Tektronix[5] oscilloscope. Two photosensors were used: (1) a PMT[6] vacuum-coated with ~300 μg/cm^2 of TPB[7] wavelength shifter and operated at -800 V. The PMT has a fast response and therefore allows for signal shape reconstruction. (2) A four-elements windowless SiPM[8] (total area 12x12 mm^2); the quad-SiPM permitted 2D event-position reconstruction. The SiPM was operated at -46 V as per the manufacturer's recommendation. However, a full study of its operation at cryogenic temperatures has not yet been performed. Therefore, the resolutions quoted here are preliminary and may improve in future work. The recorded waveforms were analyzed using dedicated Matlab scripts. The position of the event was reconstructed by a center-of-gravity technique, as described in [82].

Results Prior to biasing of the THGEM electrode, the current was driven through the heating wires in order to generate a bubble (30 V across 61 Ω for ~ 10 s). Once formed, no further heating was applied to the wires. The EL signals disappeared upon the sudden rise in the pressure and reappeared immediately after its sharp decrease. While not being able to visually see the bubble in the present setup, this confirmed its existence. All measurements were conducted at a liquid temperature of 90 K, corresponding to a vapor pressure of 1.365 bar.

Typical signals With the LHM detector polarized to ΔV_{THGEM} = 3kV (keeping E_d = 1 kV/cm and E_t = 0 kV/cm) typical signals as recorded with the TPB-coated PMT are shown in Fig. 8; Fig. 9 depicts signals recorded from the four SiPMs' pads. The green marked pulses are that of the fraction of primary scintillation light (S1) infiltrating through the THGEM holes, see Fig. 7; the red ones originate from the EL photons from the bubble (S2). One can observe a longer S2 decay constant (3-4 μs) compared to that in LXe (0.5 μs e.g. see [83]); these are due to different de-excitation processes in LAr, with longer time scales than in LXe. First, Ar has two decay constants for the scintillation or EL signal, 5 ns and 860 ns, as opposed to Xe where the longest timescale is 27 ns [84]. These two different timescales correspond to the two specific molecular bound states that can be formed during the process of recombination. The shorter timescale is associated with the singlet state and the longer one with the triplet. Then, the transition of electrons from liquid to gas has, according to [44] both long and short timescales, respectively less than 1 ns and larger than a few µs. None of them, however, can explain the 3-4 μs decay constant, observed with the two different sensors; this would require further studies.

[5]MSO 5204B
[6]Hamamatsu R8520-506
[7]Tetraphenyl butadiene
[8]Hamamatsu VUV4 MPPC S13371- 6050CQ-02

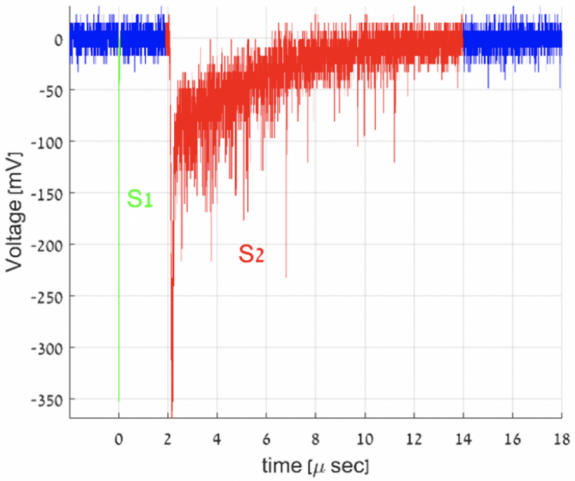

Figure 8: Example of alpha-particle induced single-event waveform, recorded by the TPB-coated PMT. Figure taken from [82].

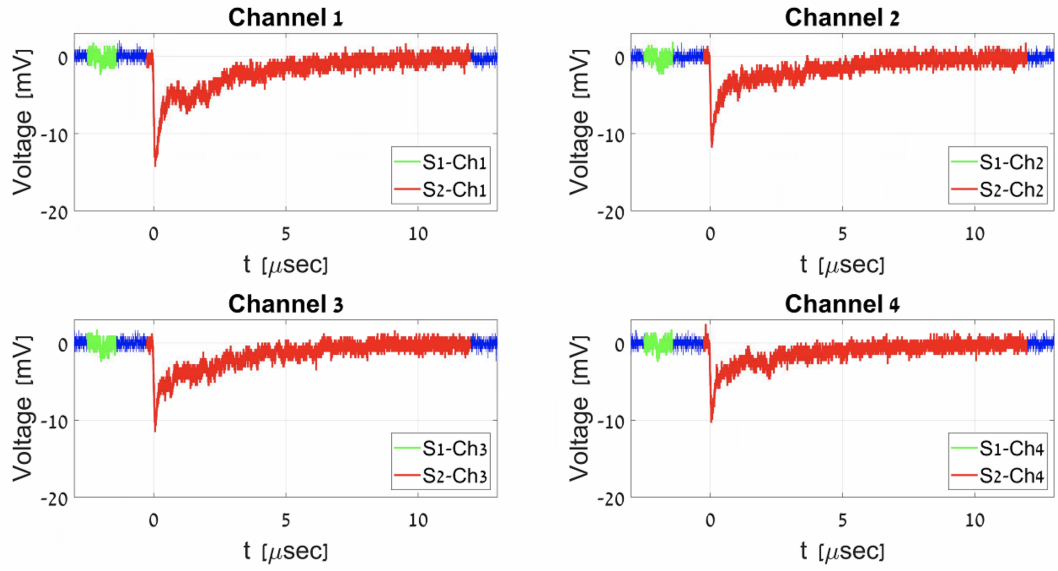

Figure 9: Example of alpha-particle induced single-event waveforms, recorded in the LAr-LHM setup of 7, by the four SiPM pads. V_{SiPM} = -46 V. Figure taken from [82].

Energy Resolution The pulse area under each waveform was computed and a pulse-area histogram was plotted. An example recorded with ΔV_{THGEM} = 3 kV, E_d = 1 kV/cm and E_t = 0 kV/cm, recorded with the PMT at a liquid temperature of 90 K is shown in Fig. 10. A Gaussian fit was applied for deriving the resolution and the mean value.

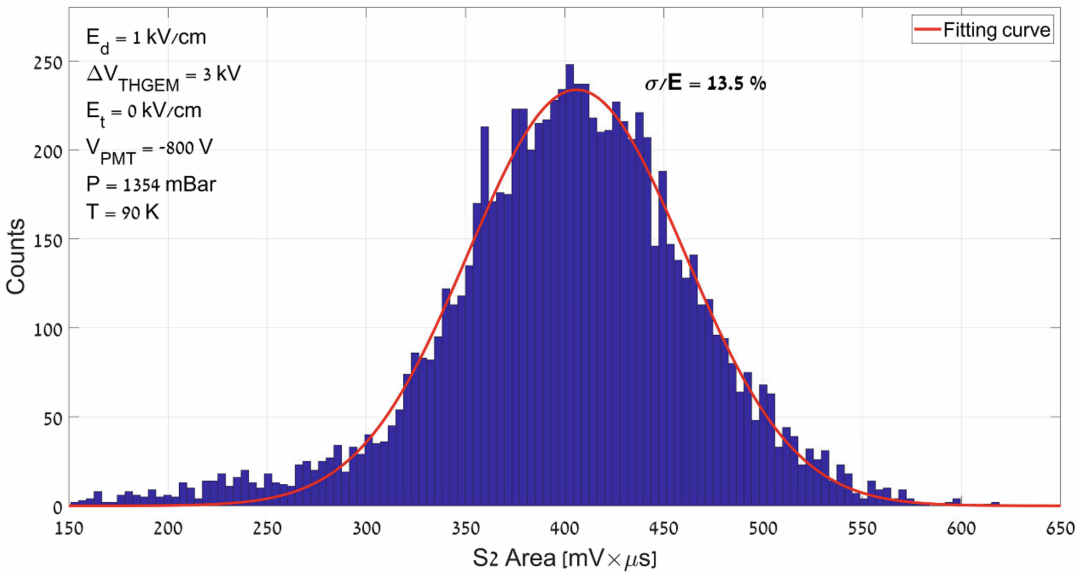

Figure 10: Area distribution of alpha-particle induced EL pulses recorded with the PMT, in the LAr-LHM setup of Fig. 7, at ΔV_{THGEM} = 3 kV, E_d =1 kV/cm and E_t = 0 kV/cm, at a temperature of 90 K. A Gaussian fit was applied to the data, for deriving the mean value and the RMS resolution. Figure taken from [82].

LAr-LHM response Fig. 11a shows the pulse-area as a function of the voltage across the THGEM electrode (keeping E_d = 1 kV/cm and E_t = 0 kV/cm) and Fig. 11b shows the RMS resolution. The linear trend shown in Fig. 11a indicates EL without charge gain. The RMS resolution at the plateau was measured to be 13.5%. This value is ~2-fold worse than the one achieved in LXe [77]. While additional optimization of the electrode is required for the LAr-LHM, the smaller number of primary electrons generated by the alpha particle represents an intrinsic limitation to the energy resolution [9].A similar response to that measured with the TPB-coated PMT was confirmed with the windowless quad-SiPM.

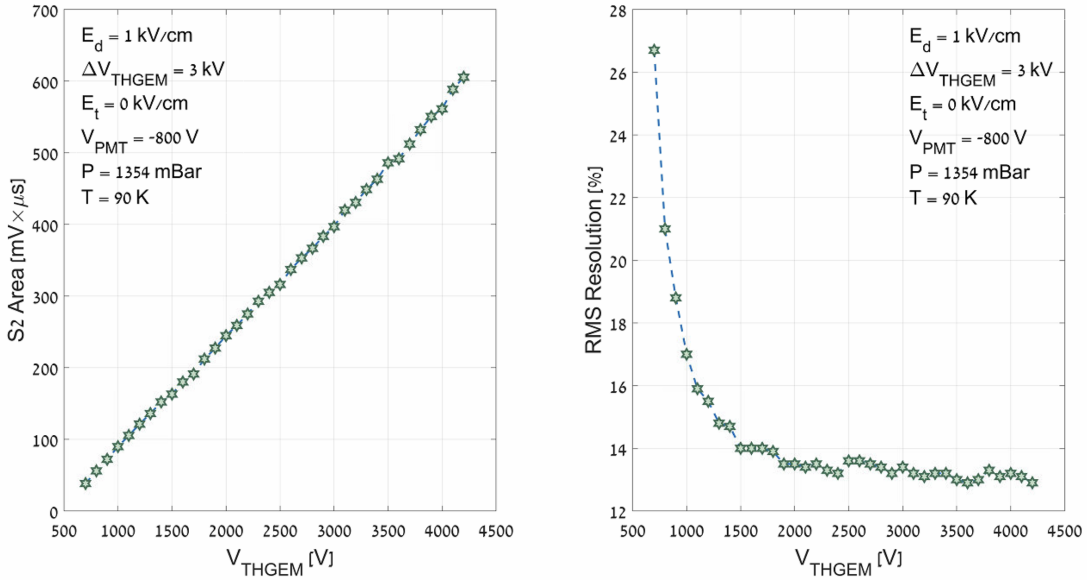

Figure 11: Response of the PMT to alpha particles, of the LAr-LHM detector of Fig. 7. (a) S2 mean area as a function of the voltage across the THGEM electrode. (b) RMS resolution of the area distribution. Figure taken from [82].

Amplification in the transfer gap As already discussed for the LXe-LHM case [77], the light yield can be boosted by increasing the electric field between the bottom of the THGEM electrode and the heating wires beneath (E_t). At moderate values of E_t (~2 kV/cm), this results in EL generated at the vicinity of the heating wires in addition to the one occurring mainly at the bottom of the holes (at high fields). At more intense fields, the electrons generate EL all along their path within the bubble: from the bottom of the hole to the wires. Fig. 12 shows the average pulse- shape obtained at different E_t values. One can clearly see the addition of a second EL pulse, occurring ~ 0.5 μsec after that originating from the vicinity of the THGEM hole; it results in a significant increase in signal magnitude, though at a slower response.

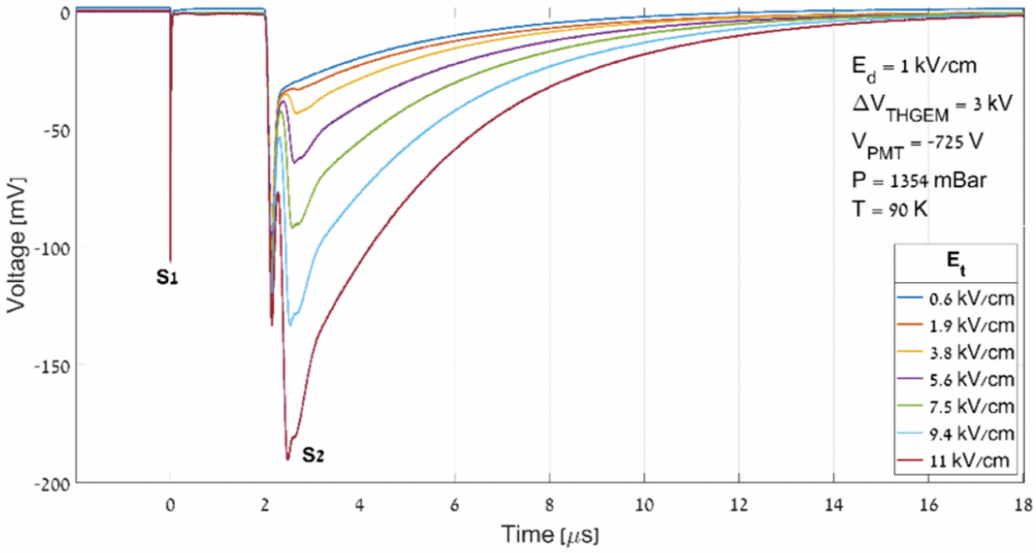

Figure 12: Average pulse shape recorded by the PMT from the LAr-LHM detector, at different values of the transfer field, E_t. ΔV_{THGEM} = 3 kV and E_d = 1 kV/cm. Figure taken from [82].

An example of the resulting pulse-area spectrum recorded with the PMT with E_t = 15 kV/cm is shown in Fig. 13. It is interesting to observe that at such a high E_t value, pulses resulting from the 59.5 keV gamma particles (emitted by the ^{241}Am) become visible. The data was recorded here with V_{PMT} = -725 V to avoid signal saturation. One should notice that although the gamma- and the alpha-particles differ in their energy by almost two orders of magnitude, their response in the LAr-LHM detector differs only by a factor ~4.5. This is due to the known different recombination probabilities of the ionization electrons, between the dense alpha-induced ionization and sparse density of electrons induced by the gamma-rays [9, 18].

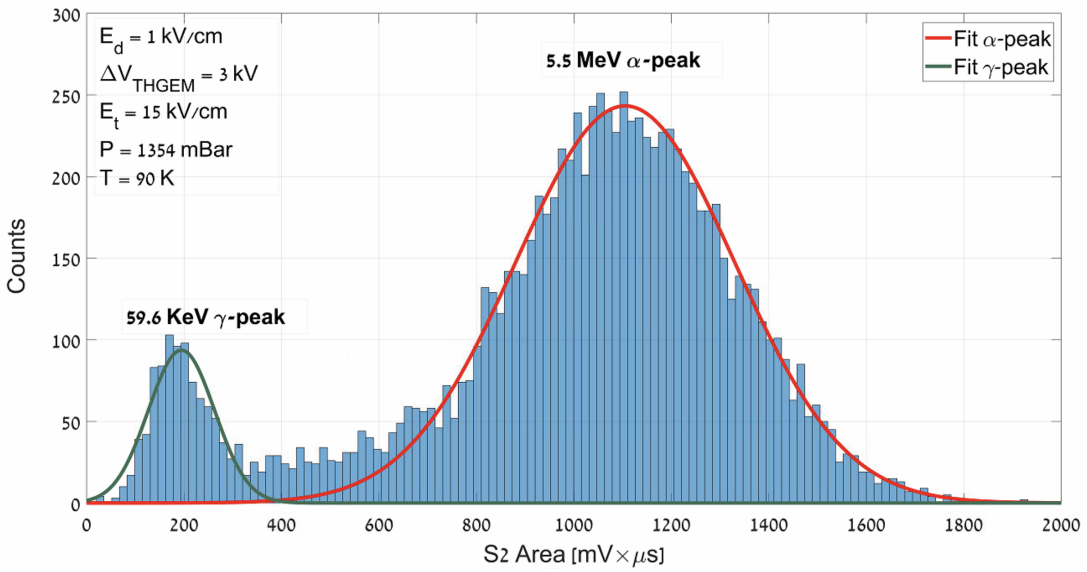

Figure 13: Pulse-area spectrum recorded by the PMT from the LAr-LHM detector with EL occurring in the THGEM holes, in the transfer gap and near the heating wires. One Gaussian fit (red) corresponds to the 5.5 MeV alpha particles and the second one (green), to the 59.5 keV gamma interactions in LAr. Figure taken from [82].

The peak position of the Gaussian fit is depicted in Fig. 14, as a function of E_t. One can clearly see that above ~4 kV/cm, the pulse-area grows exponentially, indicating upon modest (~10-fold) charge-avalanche multiplication at the vicinity of the heating wires.

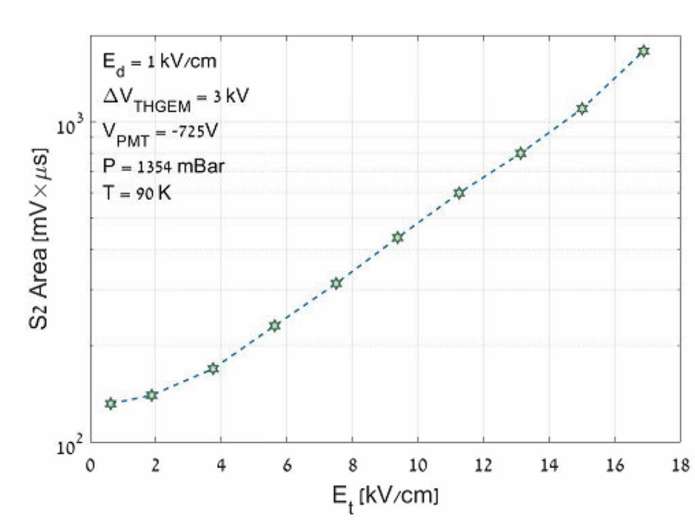

Figure 14: Signal magnitude of the alpha particle peak of Fig. 10, as a function of the transfer field. Figure taken from [82].

Position reconstruction Similar to the methodology presented in [77], the integral of the pulse from each of the four SiPM pads was computed for each event. The event position was then reconstructed by a center-of-gravity method [82]. An auto-radiographic image (using a Fuji phosphor-imager scanner model FLA-9000, plate model BAS- TR2040S) of the ^{2}41Am alpha source used in our experiments is shown in Fig. 15a. The 2D histogram of the derived event positions is shown in Fig. 15b. This very preliminary qualitative image reproduces the annular shape of the alpha source. However, the reconstruction resolution is, at this point, poorer in comparison to the ~200 μm RMS one, recorded with LXe-LHM [77], primarily due to lower EL light yield in Ar, to non-optimal ionization-electron collection into the holes and low efficiency of electron transfer into the gas bubble.

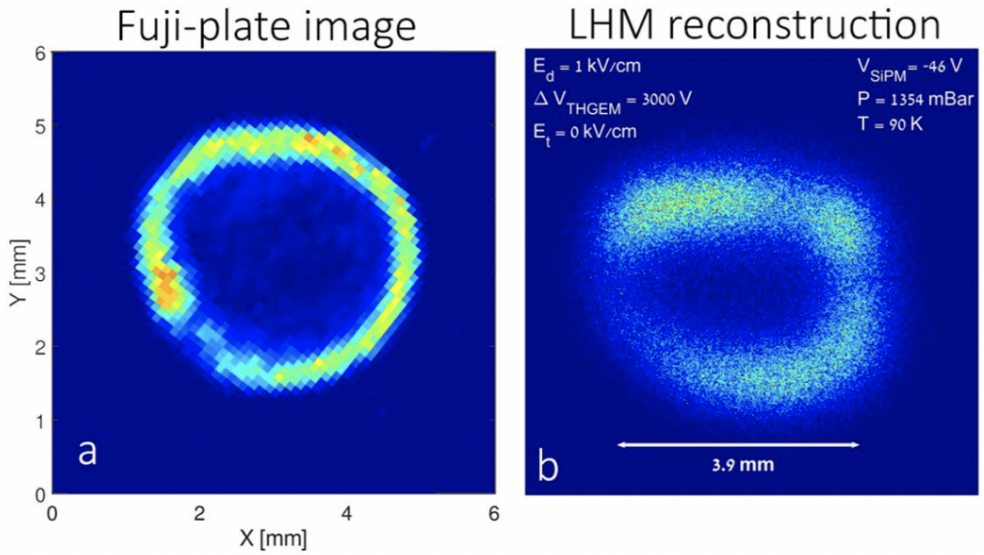

Figure 15: (a) The auto-radiographic alpha-source image, recorded with a Fuji phosphor-imaging plate. (b) 2D histogram of the EL photons emitted at the vicinity of the liquid-gas interface, recorded with the Quad-SiPM LAr-LHM detector. Figure taken from [82].

7.1.2 Bubble electrodynamics in LHM detectors

Theoretical background We examine the properties of a gas bubble formed and sustained under a THGEM, assuming that the gas and the liquid phase of the fluid are in static equilibrium [85]. The equilibrium shape of the bubble represents the solution obtained without considering the effect of non-stationary perturbations, such as convection within the cryostat or pressure fluctuations due to the coalescence of bubbles.
In an ideally single-hole THGEM the upper meniscus of the bubble can penetrate the hole, with or without protrusion out of it depending on the equilibrium configuration. The bottom side of the bubble is supposed to be essentially flat and horizontal, with a thickness

of the bubble H imposed by the amount of gas trapped.

The upper meniscus is the only free material surface within the fluid. Depending on its location and shape a different portion of the THGEM hole can be occupied by the gas, affecting in this way the performance of the LHM as a particle detector. At rest, all forces in the bulk and at the boundaries of the fluid are in equilibrium, see Fig. 16. These are:
a) the dielectrophoretic force F_d, due to the presence of a local electric field E and to a different value of the electric permittivity ϵ in the liquid, ϵ_L and in the gas, ϵ_G;
b) the Archimedean lift F_a, due to the different densities of the gas and the liquid phase;
c) the containment forces exerted by the solid support, F_c;
d) the surface tension F_S, acting at the interface between the two phases. Viscous forces, due to the differential motion of the fluid parcels, are absent in static conditions;
The dielectrophoretic force $\vec{F}_d$ is a body force, in general, expressed as the divergence of the Maxwell stress tensor $\vec{T}$, in this way: $\vec{F}_d = \nabla\vec{T}$. The Maxwell stress tensor explicitly reads: $\vec{T} = \epsilon\vec{E}\cdot\vec{E} - \epsilon\vec{E}^2\delta$. In the ideal case of perfect dielectrics with no volume charge, the only surviving contributions come from boundary terms at the material interfaces (see [86, 87]):

$$\vec{F}_d = -\epsilon\frac{\vec{E}^2}{2}\vec{n} \tag{7.1}$$

where $\vec{n}$ is the local normal at the domain boundaries.
Under some simplifying assumptions, we can derive analytically the stability conditions for the upper meniscus, in the absence of dielectrophoretic force ($\vec{F}_d = 0$), which will be discussed later. In purely hydrostatic conditions, the Archimedean lift F_a is compensated everywhere in the bulk of the fluid by the local pressure p. The first three forces, F_d, F_a and F_c, are effective as boundary terms. On the solid immobile boundaries, a local constraint force balances the pressure, keeping the boundary still. The force F_S acting on the interfaces between liquid and gas is the Young-Laplace pressure

$$\vec{p}_L = \vec{p}_L\vec{n} = \frac{2\gamma}{r}\vec{n} \tag{7.2}$$

where γ is the surface tension between the two phases and $r = 1/\kappa$ is the local radius of curvature of the interface. We consider r as a signed quantity, with the convention that $r > 0$ if the center of curvature is on the liquid side of the meniscus. With this convention, p_L is positive if the force acts in the direction of the liquid. Referring to Fig. 16, all menisci depicted in green have $r < 0$, which implies downward pressure forces and $p_L < 0$. A static meniscus implies

$$p_L = p_1 - p_2 \tag{7.3}$$

where p_1 is the relative hydrostatic pressure exerted by the liquid out of the bubble and p_2 that is exerted by the gas. The signs take into account the opposite directions of the interface normal. At the bottom of the bubble, which we assumed flat, $p_{L,b} = 0$, and thus $p_{1,b} = p_{2,b}$. This in turn is equal to the hydrostatic pressure ρlgH at the bottom height (ρ_l

being the density of the liquid and g the acceleration of gravity). Inside the bubble, the pressure varies with height as p(z) = $p_{2,b}$ - ρ_gg(z+H). Here ρ_g is the density of the gas, which is treated in first approximation as incompressible. The smallness of the vertical sizes of the system and the small variations of absolute pressure, when compared to the ambient pressure (the saturation pressure of Ar at the operating temperature. The z-axis is drawn upward, with origin at the bottom of the THGEM plate. At the top of the upper meniscus (z_t) we have thus

$$p_{L,t} = \rho_L g z_t - p(z_t) = (\rho_g - \rho_l) g (z_t + H) \tag{7.4}$$

We interpret this as a condition imposing the radius of curvature of the meniscus as a function of its height z_t:

$$r = \frac{2\gamma}{(\rho_g - \rho_l) g (z_t + H)} \tag{7.5}$$

We note that even for the simple case of an axysimmetric meniscus inside a circular vertical tube (the capillary rise problem), no general analytical solution exists (a reference numerical solution is given by [88]). To further simplify, we neglect the piezometric height differences along the meniscus, which in our case are small, of the order of the radius of the THGEM's hole R, typically smaller than the capillary length $\sqrt{\gamma/g(\rho_l - \rho_g)}$. We thus approximate menisci as circular caps of homogeneous radius r. The location of the upper meniscus is determined by a further geometrical constraint, the attachment line on the solid substrate. On this contact line the meniscus forms a prescribed contact angle θ (for us, measured at the liquid side) with the wall. This angle is an intrinsic feature of the chosen material triad, i.e. the gas, the liquid and the substrate material. Fig. 16 schematically shows possible meniscus positions realizing this constraint. To define a deterministic attachment point at the edge of the hole, an arbitrary smoothing of the bore rim is depicted. The meniscus settles on a position which, additionally to the prescribed θ, presents a downward concavity with the radius of curvature balancing the bubble pressure, and realizing a stable equilibrium with respect to movements in z. An approach for solving Eq. 7.4 respecting the constraint is presented in Appendix. In summary,

- for $\theta < 90°$, two equilibrium configurations are possible: the meniscus protruding from the top of the hole, or pinned at the bottom edge;
- for $\theta \geq 90°$, only a solution with the meniscus protruding from the top is acceptable.

Explicit expressions for the intervals of the existence of the equilibrium solutions in terms of the parameters of the problem are complicated and partially reported in [85]. It was found that the bubble thickness evaluates to 0 mm $\geq$ H $\geq$ 7.7 mm if the meniscus is pinned at the bottom edge and 7.3 mm $\geq$ H $\geq$ 11.1 mm if the meniscus protrudes from the top of the hole.

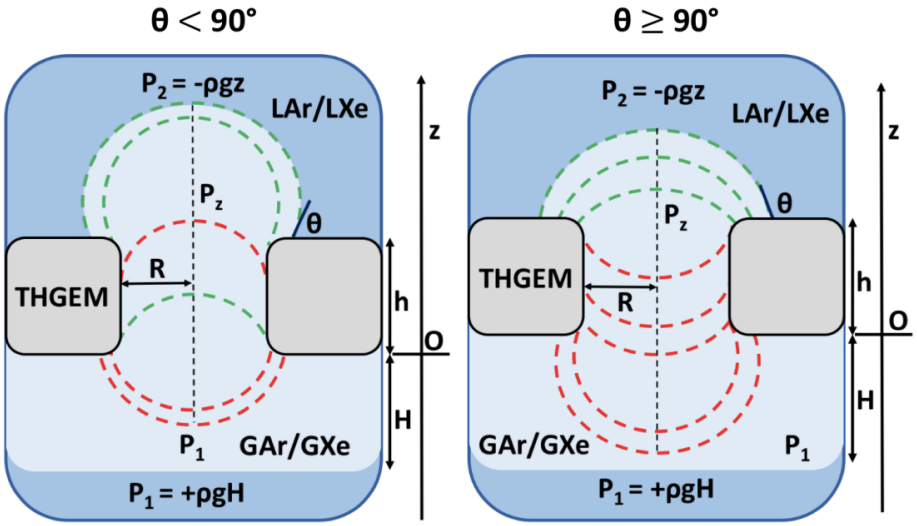

Figure 16: Interface configurations for a) contact angle $\theta < 90°$, b) contact angle $\theta = 90°$, c) contact angle $\theta < 90°$. In green, the acceptable equilibrium configurations are shown. Figure taken from [85].

The electric field $\vec{E}$ adds the term Eq. 7.1 to Eq. 7.3 and Eq. 7.4, transforming them into

$$p_L = p_1 - p_2 - \frac{\epsilon_1 \vec{E}_1^2 - \epsilon_2 \vec{E}_2^2}{2} \tag{7.6}$$

and thus changing the balancing value of the meniscus curvature. Formally, the electric force ($\vec{F}_e$), which acts normally to the interface too, can be assimilated to a local pressure force. In contrast with the piezometric term, the spatial dependence of the electric field is nontrivial for complex electrode geometries, and it is not as easy to define viable analytical approximations as for pure hydrostatics. We, therefore, resort to numeric computation.

Contact angles measurements

Methodology All the experiments to measure the contact angles were conducted in the following way:

- The materials under study consisted in discs of ~7 mm diameter and ~1.5 mm thickness. Before being investigated, the discs underwent ultrasonic cleaning (15 minutes in petroleum ether, 15 minutes in acetone (whereas possible), and 15 minutes in ethanol);
- A grid of resistive wires (Ni-Fe, 55 μm in diameter, 2 mm spacing) was fixed 5 mm below the discs. The wires were heated by a current generator, to form bubbles in the noble liquid and they were trapped under the disc's surface (Fig. 17);

- A CALTEX VIP-50-HD60 camera was coupled externally to the central viewport of the cryostat (Fig. 17);
- The setup was illuminated through the remaining viewports by appropriate lamps.

A standard technique to measure contact angles is the so-called "captive bubble method" [89], where the angles are reconstructed from the images of the bubbles trapped underneath a solid material. In order to reconstruct the contact angle formed between the bubble and the chosen substrate, we recorded multiple sets of images (1000 frames/set) using the external digital camera and operating it in an automatic acquisition mode (sampling rate of 1 frame/s). Each set of images was then processed using a dedicated Python script with the purpose of adjusting the contrast and brightness, converting the color code (from RGB into greyscale) and cropping opportunely the bubble. Each set of images was subsequently manually analyzed and a selection of 200 frames containing visible and distinct bubbles was then performed. All the images containing blurring effects due to bubble movements or to light reflections were discarded. Each sample was analyzed using the drop-shape analysis extension "DropSnake" [90] of the software ImageJ [91]. The shape reconstruction was done with an interactive spline method where the knots were placed by hand on the bubble interface [92].

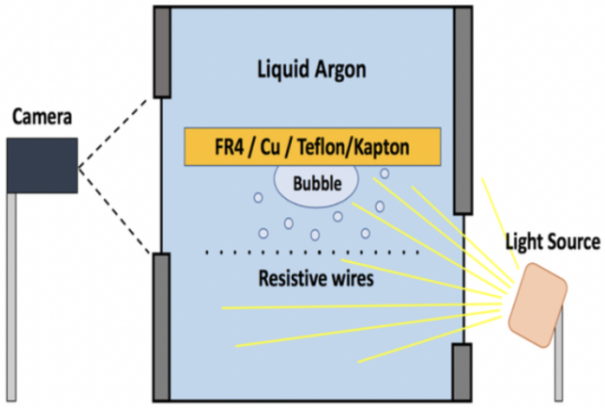

Figure 17: Scheme of the setup used to perform the materials characterization. Figure taken from [85].

This offered us a rather straightforward and reliable way to reconstruct the bubble shape, providing two values of the contact angle for each frame, respectively the left one and the right one. Each statistical sample resulting from this analysis was thus composed of 400 values. A histogram was formed, with the resulting distribution being fitted with a dedicated Matlab script.

Results Here follow the results obtained from the characterizations of four materials commonly present in detector assemblies, namely Copper, Epoxy fiberglass (FR4), Teflon and Kapton. According to the contact angle value, different equilibrium configurations can be allowed and a distinct behavior of the bubble inside the hole can become manifest. Conventionally, in analogy with the nomenclature adopted for material characterizations performed in water, we will define the solid material to be:

- argon-phobic, if $\theta > 90°$, meaning that the local gaseous phase tends to adhere and spread over solid substrate;
- argon-philic, if $\theta < 90°$, meaning that the liquid has the tendency to wet the solid material.

The prefix "argon" in the definitions makes explicit reference to the liquid phase, since in DP noble liquid detectors both phases are composed by the same material. From our analysis, an argon-philic behaviour was observed with FR4, Copper and Kapton, see as an example Fig. 19 (top), while Teflon exhibited an argon-phobic tendency, as shown in Fig. 19 (bottom). In the first case the presence of small and escaping bubbles was favored while in the second case the bubbles were able to coalesce into a larger one and spread over the slab surface. Therefore, these measured contact angles are "dynamic contact angles" since the bubbles were not static on a sufficiently long observation timescale and represent an average between the advancing contact angle and the receding one. Precise values of static contact angles not surprisingly are usually contained in an interval of values bounded by the advancing/receding contact angle [93].

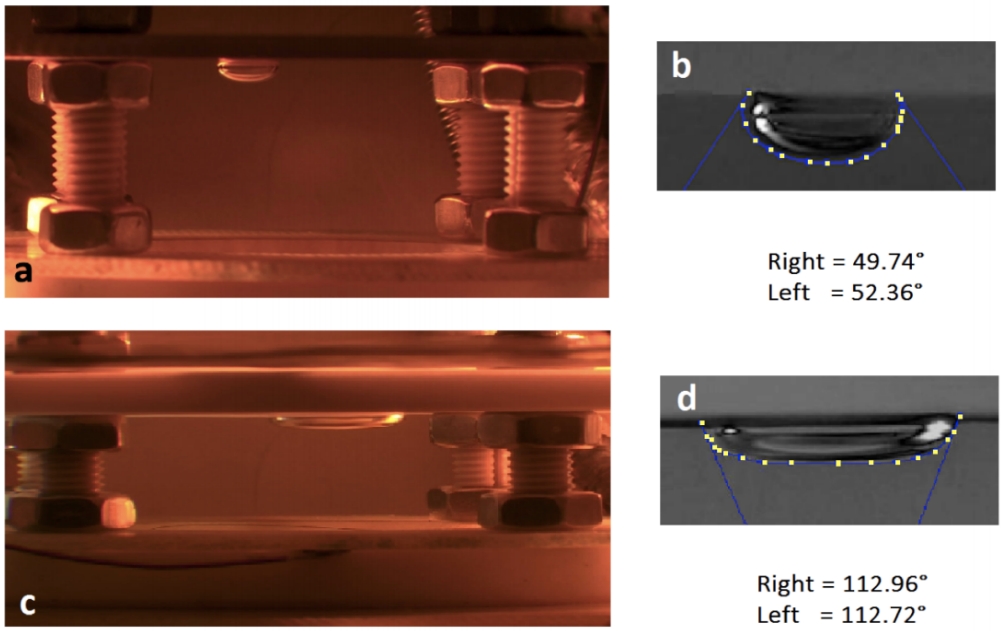

Figure 18: a) Observation of a bubble trapped underneath a Copper slab immersed in LAr; b) Example of bubble reconstruction of the image depicted in a) processed according to the discussed methodology. The results for the left and right contact angles are also reported. c) Observation of a bubble trapped underneath a Teflon slab immersed in LAr; d) Example of bubble reconstruction of the image depicted in c) processed according to the discussed methodology. The results for the left and right contact angles are also reported. Figure taken from [85].

In Fig. 19, as an example, we report the Gaussian-fitted histogram for the FR4 characterization.

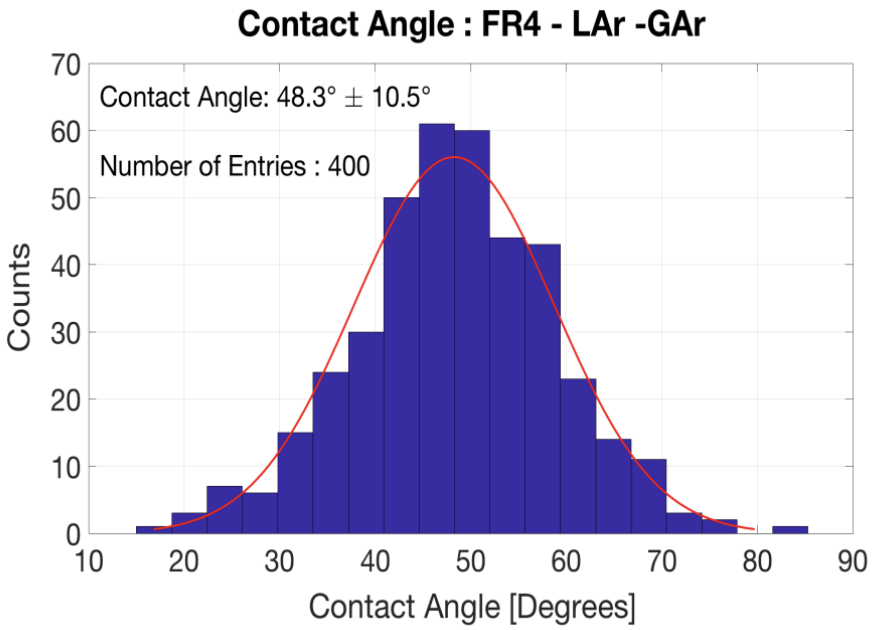

Figure 19: Example of a fitted histogram showing the contact angles measured from bubbles sustained underneath a slab of FR4 immersed in liquid argon. Figure taken from [85].

In Table 4 we report all the results of the material characterizations performed according to the methodology discussed above:

Material	Measured θ	Behaviour
Copper	45.5° ± 8.5°	Argon-philic
FR4	48.3° ± 10.5°	Argon-philic
Teflon	108° ± 6.5°	Argon-phobic
Kapton	59.3° ± 9.3°	Argon-philic

Table 4: Contact angles measured in LAr, for bubbles sticking to different substrate-material surfaces.

Little can be said in quantitative terms about the effects of the environment surrounding the bubble (presence of fluid motions, convection, pressure gradients, spontaneous bubbles...) - we observed that the bubbles were "breathing" (cyclic deflation and swelling) and were able to escape from the field of view in the measurement timescale. The only way we achieved trapping a consistent quantity of gas underneath our slab was via the insertion of a containment, i.e. a thick ring that could be fixed underneath slab or the electrode. This proved to be the only reasonable way to see a stable local DP, confirming thus the necessity to introduce this element in LHM detectors. These results for the dynamic contact angles, measured for the first time, offered the possibility to bypass analytical limitations due to

the complexity of the electric field in the proximity of the holes and paved the way for the numerical simulations of the bubble electro-hydrodynamics

Numerical simulations Numerical simulations were carried out in order to determine the equilibrium bubble shape in an electrostatic field. The electric field, induced by the voltages applied to the operative electrodes, depends on the medium (liquid, gas or substrate material), and on its spatial distribution. At the same time, the dielectric forces on the fluid affect the location of the bubble. In order to solve the problem, the two effects need to be coupled. Because of the non-trivial spatial dependence of the electric field, we addressed the problem computationally. The solution gives us, in addition to the equilibrium shapes, full information about the field within the detector. In Fig. 20 we show a set of final meniscus positions obtained varying the electrode potentials, for menisci pinned at the top and bottom of the hole, corresponding to the horizontal series of symbols in Fig. 63. Both sets use values H of the bubble depth for which pure hydrostatics guarantees stable solutions at $V_0 = 0$ V (see eqs.(8, 11) in [85]). In the present geometry, at both meniscus locations, the electric pressure (eq. 7.1) always acts from the liquid toward the gas, which is downwards. Consequently, it increases the value of the curvature κ (cfr. eq. 7.2) as V_0 increases, reducing the downward concavity of the meniscus, or even turning it to upward concave when admissible. Detailed analysis of the electric field, not reported here, shows that the electric pressure is nonuniform along the meniscus, as well as the resulting balancing curvature; the interface may deviate significantly from the idealized spherical shape. For $\theta < 90°$, the meniscus can attach to the bottom edge of the hole with a larger range of curvatures than the range allowed at the top. On the lower face, both convex and concave menisci are allowed (cnfr Fig. 12a and Fig. 12c in [85]). This is reflected in the larger range of voltages that can be applied while maintaining equilibrium in the former case. We remark however that the analysis done here is essentially static; the existence of parameter ranges for which one or the other meniscus solution is stable does not by itself imply which position is preferred, or that a destabilized bubble settles to a given position once some amount of gas is added at the bottom or escapes through the hole. All these are dynamical effects which should be addressed by a more complete analysis.

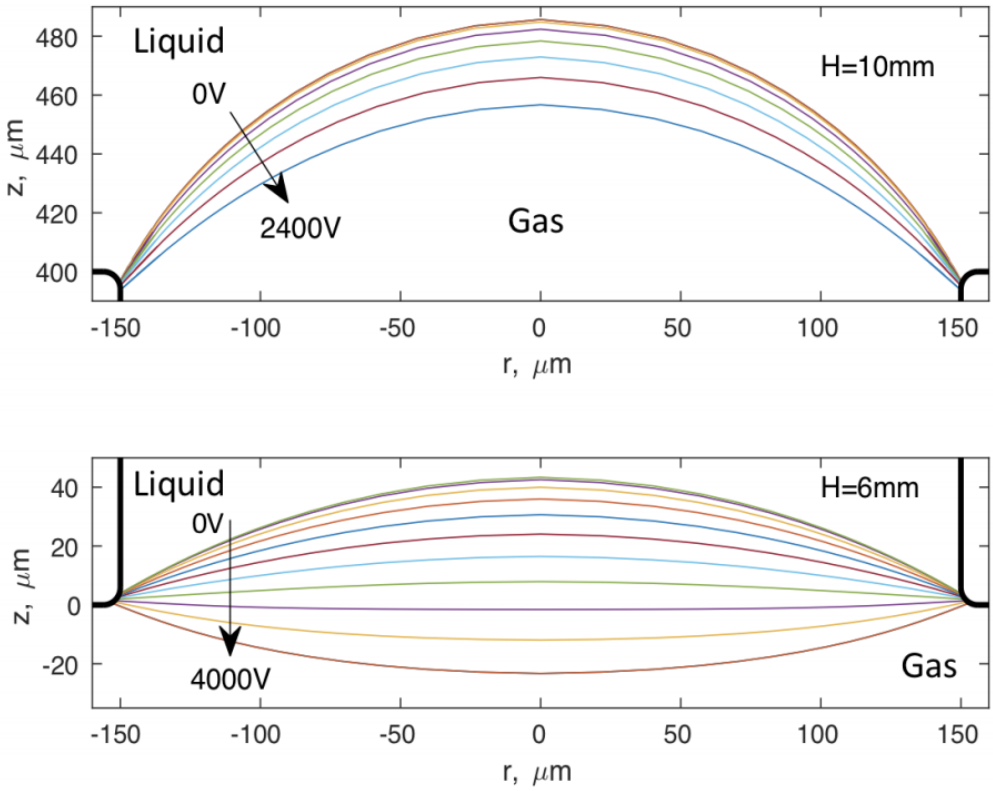

Figure 20: Relaxed meniscus profiles at top and bottom of the hole. Profiles are obtained at fixed H and varying V0 in steps of 400 V. Figure taken from [85].

The electric field map allowed us to compute the trajectories of charged particles within the detector. In particular, the electrons produced by scintillation are supposed to have negligible inertia and thus follow the lines of the field of $\vec{E}$, see Fig. 21 left. According to Eq. 4.9 of [9], the number of photons N_ν produced per unit of length of the trajectory of an electron is a function of the local electric field E and gas pressure p:

$$\frac{dN_\nu}{dx} = aE - bp - c \tag{7.7}$$

with a, b and c characteristic constants of the gas considered. One such realization is exemplified in Fig. 21, right. Once the number of photons is integrated along the trajectories, and weighted by proper angular photon-collection factors, it is possible to predict the signal produced by a detectable particle event. While this is deferred to further work, this information is essential for predicting and eventually optimizing the detector performance.

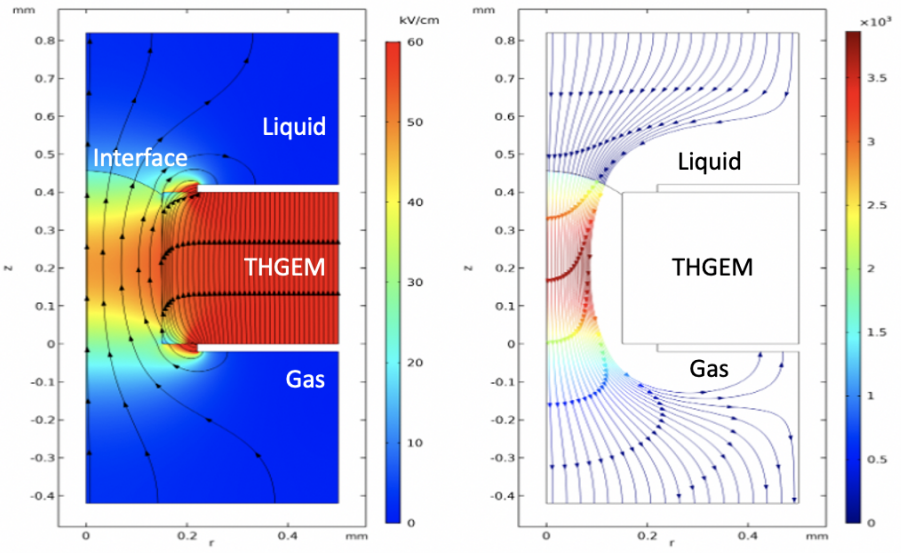

Figure 21: Left panel: electric field for the case of meniscus at the top of the hole, for H = 10 mm and V = 2400 V. Right panel, trajectories of electrons entering the top domain boundary. The trajectories are color-coded according to their photon emissivity $(dN_\nu)/dx$, in photons/cm.

Micro-computed tomography (μ-CT) In order to validate the results deriving from the model presented in the previous sections, the bubble interface inside the holes had to be directly observed or reconstructed. This posed a major difficulty since it was impossible to devise an optical way to inspect inside the holes. An original solution to this problem was proposed, called X-ray microtomography (μ-CT) [94]. The μ-CT is a 3D-imaging technique using X-rays to reconstruct an object structure by looking at the different attenuation paths: density differences result in a different X-rays absorption according to the law $I(t)/I_0 = e^{-\mu t}$, where I_0 is the initial intensity of the beam, I is the attenuated intensity and μ represents the mass attenuation coefficient. The creation of cross-sections of a physical object can be used to recreate a virtual 3D model of the object without destroying the original object itself, where the prefix "micro" stands for the possibility offered by this technique to achieve very high resolutions (up to few μm). It is widely used in the field of medical imaging and in industrial computed tomography. As far as the validation of the model is concerned, a direct validation in LAr was discarded for obvious reasons of complexity and control of the experiment. It was thus decided to proceed in the direction of performing experiments using other materials with known parameters (water, siliconic oil) at room temperature. Upon a successful validation of both the bubble hydrostatics and bubble electrodynamics in these materials, the model predictions for LAr would be trusted with higher confidence. The studied sample was a 0.4 mm thick perforated FR4 disc (no Cu) of 13.9 mm diameter with 0.5 mm diameter holes, spaced by 1 mm. The structure was installed in a special home-made plexiglass electrode holder. The latter was opportunely drilled on one side in order to allow for the inflation of the bubble. After the

gas insertion, an ad-hoc cork was inserted in the gas input with the aim of preventing the liquid from spilling out. See Fig. 22. Two liquids were selected for the investigation: water and siliconic oil (Dow Corning diffusion pump oil - 704). The latter was chosen because of its electrical insulating properties, representing thus a viable liquid candidate for the validation of the bubble electrodynamics (i.e. in the presence of electric fields) at room temperature.

A picture of the assembly is reported in Fig. 22.

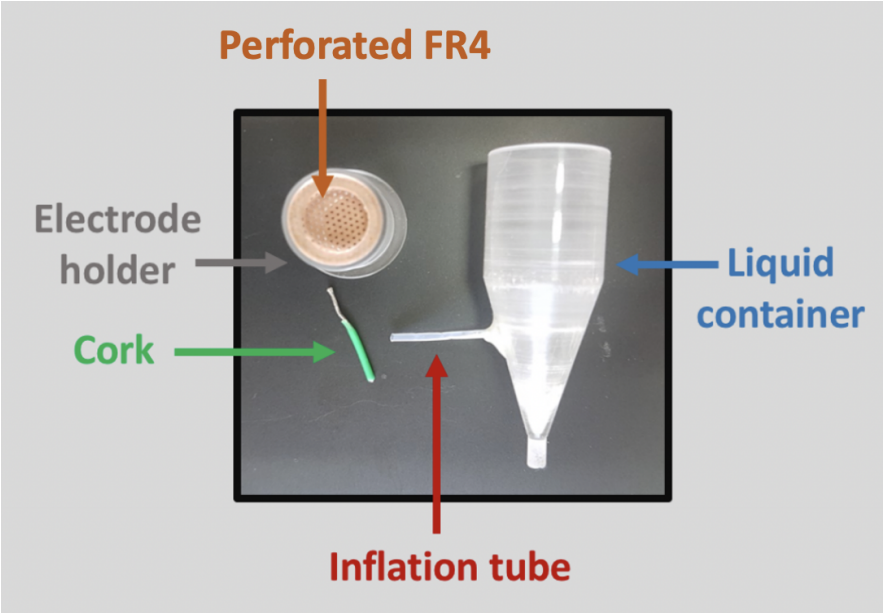

Figure 22: Perforated FR4 disc installed into a dedicated Plexiglass electrode holder. Figure taken from [85].

The assembly was subsequently introduced in an Xradia micro-CT scanner (1 μm resolution, X-Ray source: 20-90 kV) and a scan was performed. Reconstructions of the bubble interface protrusions into the holes obtained in the two investigated liquids are illustrated in Fig. 23. The bubble interface penetrates into the 0.5 mm diameter holes by $\approx$16.5 μm and $\approx$37 μm in water and oil, respectively. These values are in good agreement with our respective model predictions of 16 μm and 35 μm. The thickness of the bubble in these experiments was $\approx$4 mm. Estimations of the expected protrusions were computed for both liquids using the values of the contact angles measured on a FR4-substrate surface with a sessile drop method [95, 96]. From the contact angle measurements, it was found: $\sim$39° and $\sim$24° for water and silicone oil, respectively. Possible causes for the very small deviations ($\approx$6%) in the interface protrusion from our model prediction, might be related to uncertainties in the measured contact angles or other experimental systematic errors.

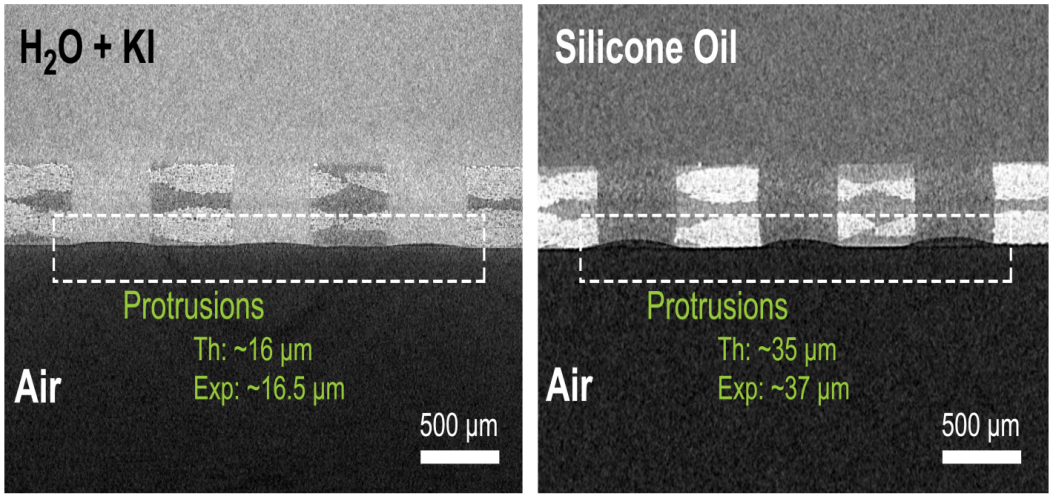

Figure 23: μ-CT cross-section images of air bubbles trapped underneath a bare perforated electrode immersed in Left) H_2O+5%KI; Right) Silicone oil. The theoretical and experimental values for the bubble protrusion into the 0.5 mm diameter holes are displayed. Note the laminated structure of the FR4 epoxy-resin plate. Figure taken from [85].

Following the hypothesis that the electric field at the interface should have an impact on its shape and the model-simulation results, led our experimental efforts to validate the bubble electrodynamics. Experiments were carried out in silicone oil, using the same container. To avoid X-ray beam hardening artifacts in the μ-CT reconstruction process, metal coating on the perforated electrode had to be avoided. Instead, the two surfaces of the perforated disc were evaporated with thin (10 nm) graphite films prior to hole drilling. In addition, the 1 mm thick FR4 perforated-electrode disc was designed with a 0.1 narrow Cu HV-contact ring. After graphite-film evaporation, holes of 0.8 mm diameter were drilled on the disc. The experimental μ-CT procedure is similar to the one described above. The voltage was supplied to the electrode by a CAEN N8315 NIM Power Supply. Tomographic scans were run at two different voltage configurations: ΔV= 0 kV and 3 kV (E = 0-30 kV/cm over the 1 mm thick disc). The tomographic scans were of 8 h duration and of an intrinsic resolution of 2.5 μm. It should be added that the contact angle of an air bubble trapped in silicon oil underneath a graphite surface was measured by x-ray transmission (see Fig. 24) in the microtomography system; it is an important parameter for the model simulations.

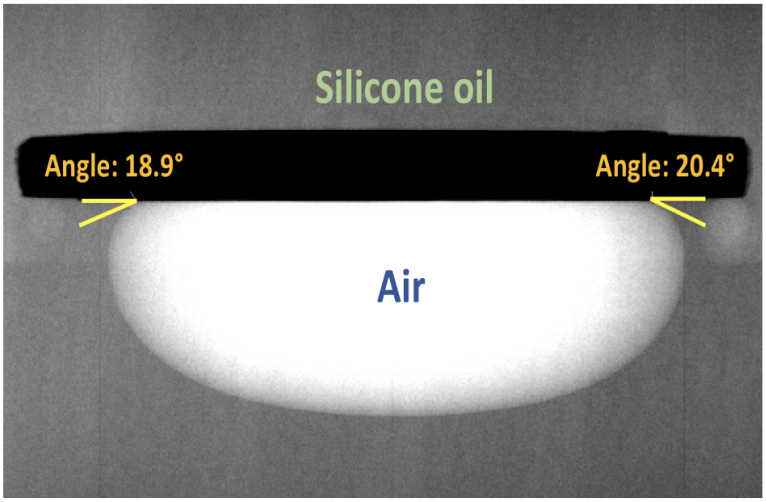

Figure 24: μ-CT reconstruction of an air bubble trapped underneath a graphite-coated disc immersed in silicone oil. The average measured contact angle equals to 19.6°. Figure taken from [85].

The measured average value for the contact angle of the air bubble sustained below a graphite-coated disc immersed in silicone oil is 19.6° and the measured bubble thickness is ≈3.4 mm. In order to implement our simulations, the following parameters were taken into account: the measured contact angle, the dielectric constant of air $\epsilon_{air} = 1$, of silicone oil $\epsilon_{SO} = 2.8$ ($\Delta\epsilon_r = \epsilon_{air} - \epsilon_{SO} = 1.8$) and the surface tension of silicone oil $\gamma_{SO} = 37.3$ mN/m, as reported in [97, 98]

A direct comparison of the reconstructed protrusions via μ-CT with the simulations was not possible because of the presence of surface imperfections stemming from the drilling process. Instead, we opted for the comparison of the reconstructed protrusion variations measured at the center with the electric field assuming ideal edges. The reconstructed images for the applied voltage $\Delta V = 0$ kV and 3 kV are shown in Fig. 25. The difference between the expected protrusion variation within the 0-3 kV range in simulations, ≈28 μm, and the measured one, ≈34 μm, is in agreement within ∼16% error.It is possible to observe that not only the interface re-adjusts itself to satisfy the new equilibrium set by the presence of the electric field, but also that the preferential configuration corresponds to a bubble protrusion into the hole from the bottom of the electrode. No bubble protrusion was observed in this work from the top side of the electrode. In Fig. 25, the reconstructed images for the applied voltage $\Delta V = 0$ kV and $\Delta V = 3$ kV are shown.

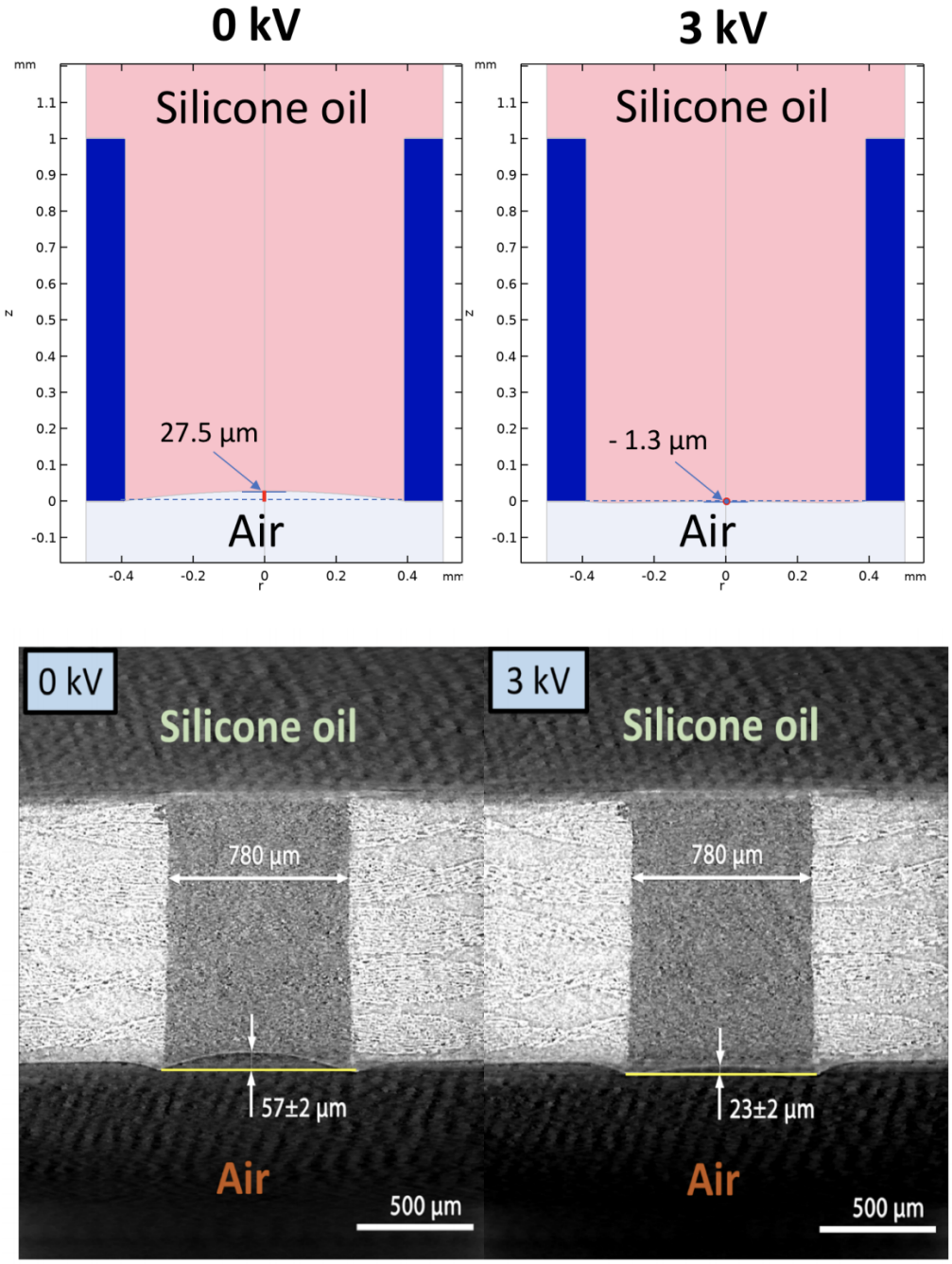

Figure 25: **Top**) Results of the simulation of an air bubble trapped under a graphite-coated THGEM hole immersed in silicone oil for two different voltage configurations; Left: 0 kV; Right: 3 kV. **Bottom**) Reconstructions of an air bubble trapped under a graphite-coated THGEM immersed in silicone oil for two different voltage configurations; 2.5 μm resolution scans. Estimations of the experimental bubble protrusion variations are displayed on each panel. **Left**: 0 kV; **Right**: 3 kV. Figure taken from [85].

Summary For the first time, the operation of the bubble-assisted LHM detector in LAr was demonstrated. A bubble was generated and sustained under a THGEM electrode. Alpha particle events were reconstructed by collecting electroluminescence light from the passage of ionization electrons through the argon bubble. The detector response was linear as a function of the applied voltage. Modest charge-avalanche multiplication was recorded from electrons drifting within the bubble towards the heating-wires. Imaging of the alpha-particle-induced EL photons was demonstrated, qualitatively, with the quad-SiPM, achieving a resolution of 13.5% rms, 2-fold worse than in LXe-LHM. While this requires additional optimization, an intrinsic limitation to the energy resolution stems from the material properties of LAr. Next steps in this direction might include the optimization of the electrode geometry. An investigation aiming at evaluating the nature of the interface of a gas bubble trapped in liquid under a perforated electrode was also carried out. Starting from the hydrostatic equations describing a bubble trapped in LAr underneath an electrode, the possible bubble equilibrium configurations were computed and the distinct behaviors (argon-philic/-phobic) dictated by the value of the contact angle were discussed. For the first time, bubbles in LAr were optically observed and their dynamical contact angles were measured in LAr on potential materials forming LHM electrodes: Cu, FR4, Teflon and Kapton. Numerical simulations were implemented to investigate the bubble equilibrium configurations in the presence of an external electric field: it was clarified that the electric fields at the interface vicinity contribute to the equilibrium balance as an additional pressure term. The results of the model-simulated bubble hydrostatics and electrodynamics in room-temperature water and silicone oil were validated by μ-CT imaging experiments. Using μ-CT it was shown that it is possible to reconstruct the interface of an air bubble trapped underneath an electrode immersed in water or in silicone oil within 6% agreement with the theoretical predictions. A validation of our bubble electrodynamics model was achieved in silicone oil, under different electric-field conditions; the observed interface-protrusion variations with the field were in 16% agreement with the simulations. The successful validation of our model in room-temperature liquids, should lay the groundwork for inferring the bubble-interface configuration in noble liquids. Further model-simulations studies are expected to shed more light on the interface modifications induced by shaping the electric fields in the holes' vicinity. These could serve as a solid base for the enhancement of the electron transfer efficiency from a noble liquid to the bubble in LHM detectors. An optimal field (and interface) shaping could also play a role in enhancing their electroluminescence (EL) photon yield. While currently, most of the EL-photons are emitted within a small portion of the bubble, at the vicinity of the bottom of a hole [83], conditions may be found to push the interface deeper into the high-field region within a hole, thus enhancing the EL-photon yield. To this regard, an optimization of the electrode geometry allowing for an equilibrium configuration of the meniscus located at the hole center could be investigated (e.g. SC-GEM).

7.2 WELL-based structures

7.2.1 Development of novel resistive materials

This part of the work was developed in collaboration with the University of Science and Technology of China for the production of the DLC layers and with the University of Santiago de Compostela in Spain for their characterization. The development of novel resistive ceramic plates was conducted in collaboration with the Galician Institute of Ceramics and with the University of Santiago de Compostela in Spain. Carbon nanotubes-doped 3D-printed materials were produced at the Hebrew University of Jerusalem and characterized at the Weizmann Institute of Science.

DLC layers for cryogenic applications Resistive materials were extensively studied at room temperature, where they proved to enhance the detector's performance while providing protection against electrical instabilities [62]. In radiation-detector science, there seem to exist at least three situations of recurring technological interest: i) stabilization of the gas-discharge process at high electric fields ('spark-quenching'), [64, 99–101]; ii) adjusting the charge-induction profile from moving charges to improve space resolution in tracking detectors [102–104]; iii) reducing local charging-up as well as suppressing surface discharges in, for instance, high voltage feedthroughs [105], some types of MPGD [106, 107], and field-cages in time projection chambers [108] (Fig. 26). While the response of a system in the above situations is dependent on the overall geometry, the main performance metric is usually the electrical resistivity of the material, either bulk resistivity ρ_v or surface one R_S. For linear, homogeneous and isotropic coatings, sheets or plates, they relate through $R_S = \rho_v/t$, where t is the material thickness. Approximate orders of magnitude can be found in Table 5, for either coatings ('films') or plates.

Case	R_S[MΩ/□]	ρ_V[GΩ·cm]
Ia	-	0.1-1 to 10^3 -10^4 [109]
Ib	10-1000 [110]	-
II	0.5-2.5 [102, 104]	-
IIIa	1000-10000 [108, 111]	-
IIIb	1000-10000 [105]	-

Table 5: Surface and bulk resistivity values employed by various authors in most typical applications. In I) the lower limit is imposed by loss of spark quenching and the upper one by loss of rate capability (charge build-up). For typical geometries, the values given in II) lead to cluster sizes at the mm's scale. In III) the lower limit is given by current consumption, the upper limit is setup-dependent.

With a 'too-conductive' material potentially leading to discharges, intolerable currents or the impossibility of localizing a moving charge (depending on the application), a 'too-resistive' material would lead, on the other hand, to surface charging-up and field defor-

mations. It thus follows that materials of interest to particle-physics instrumentation fall into the category of 'bad insulators' (e.g., [112] and references therein). Because of the low industrial interest on this type of materials, their availability is limited, calling for new materials and techniques for scientific use.

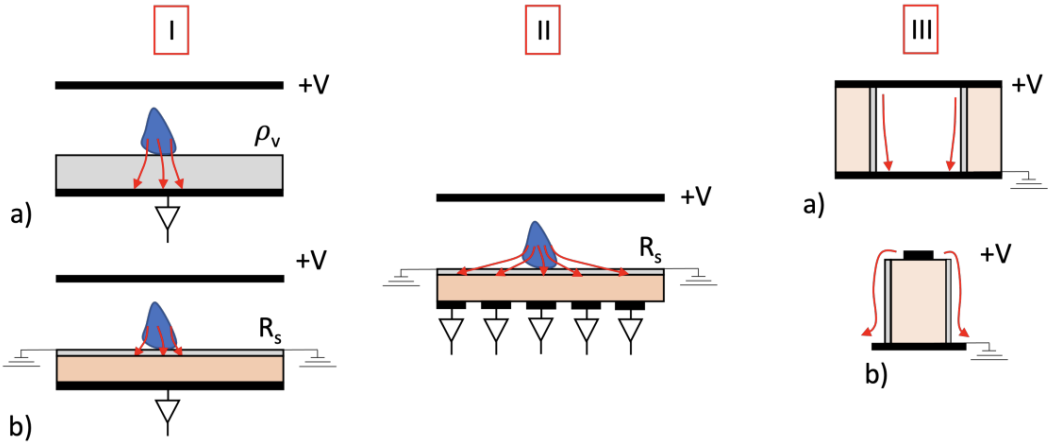

Figure 26: Most common situations of practical interest for use of resistive materials in gaseous and particle detectors. Ia-Ib) 'spark quenching': current flow is limited to a small area, reducing the electrostatic energy available in case an avalanche reaches a too large size. II) 'cluster-size tuning': current flow is adjusted in order to facilitate signal induction over a larger region, leading to oversampling and better spatial reconstruction of the charge centroid. III) 'mitigation of charging-up and surface discharges': current flow through uniform resistive materials minimizes charging-up and provides suitable boundary conditions matching the electrostatic potential in the active medium. Figure taken from [113].

One problem with DLC coatings, as with most insulating materials, is that their resistivity quickly rises at cryogenic temperatures: a material suitable for operation at room temperature can become a perfect insulator in cryogenic conditions, impairing operation. Thus in this work we consider thin DLC films made by sputtering on Kapton and FR4 substrates, and study their behaviour in the surface resistivity range 0.1-10^5 MΩ (tuned by adjusting the coating thickness and hydrogen doping), down to liquid nitrogen (LN_2) temperature. The chosen range is expected to cover most situations of practical interest.

Experimental methods

DLC coating DLC was deposited through magnetron sputtering [107]. A Teer 650 device (from Teer Coating Ltd) at the SKL in Hefei was used, allowing for evaporations up to surface dimensions of 25×25 cm^2. The substrates were cleaned with ethanol and dried in an oven at 70 °C. The sputtering lasted for about 20-60min, resulting in film thicknesses generally in the range 10's-100's nm. Evaporations were made on FR4 and Kapton, two common detector substrates of different mechanical and surface properties Fig. 27). As a reference, the thickness of the most conductive FR4 sample presented in this work was

estimated to be compatible with t = 160 ± 10nm, the uncertainty reflecting the variation between the in-situ measurement (with a step profiler) and the ex-situ one (by grazing-angle X-ray reflectometry on a twin sample evaporated on silicon substrate).

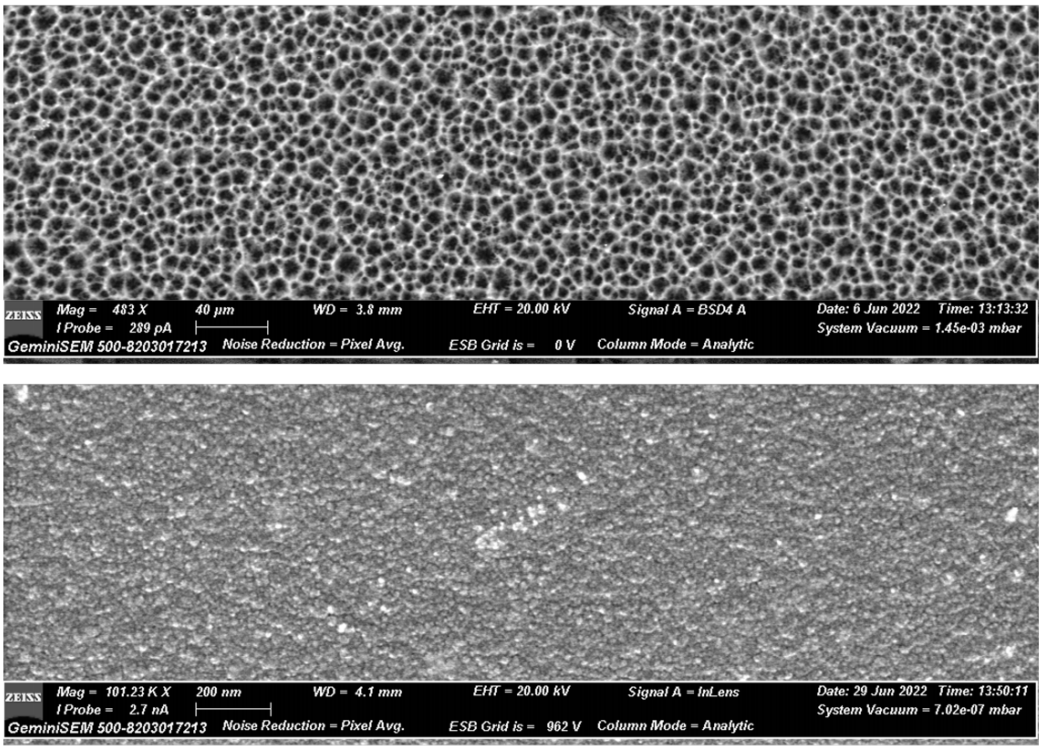

Figure 27: Images taken with scanning electron microscope of the DLC films on FR4 (40 μm scale, top) and Kapton (200 nm scale, bottom). The scales have been chosen to highlight the main features observed. Figure taken from [113].

Cryogenic setup The surface resistivity as a function of temperature was determined with a physical property measuring system PPMS[9], following a square four-point probe method over a ∼1 cm^2 area. Geometrical corrections were applied according to [114], amounting to about 30%. This PPMS assures thermal equilibrium at every measuring step, however, its sensitivity reaches just the lower-end of resistivities of interest (up to R_S = 30 MΩ/□, with □ = 1 cm^2), so a system was devised to cover the entire range. Measurements were made in this case by biasing a silver epoxy strip deposited on the sample and reading the return current on a second one, approximately forming a 1 cm^2, through a picoammeter[10]. The setup was assembled on a stainless steel vessel filled with a helium atmosphere (1.5 bar) and immersed in a LN_2-filled Dewar acting as a cryostat. To mitigate the effect of water freezing, the vessel was evacuated down to 10^{-3} mbar with a turbo-molecular pump[11]

[9] Quantum Design, Model 6000
[10] Keithley 6487
[11] Pfeiffer Duo 016B

prior to filling. The setup consisted of two spring-loaded probes in a PEEK frame, with a holding arm bolted to the vessel. The sample laid on the floor, electrically insulated with a thin Kapton layer and covered with APIEZON N grease to ease thermal coupling between sample and vessel. The temperature was sensed directly on the Kapton with a PT100 sensor, its resistance was measured through an Arduino micro-controller board. A sketch of the setup is shown in Fig. 28.

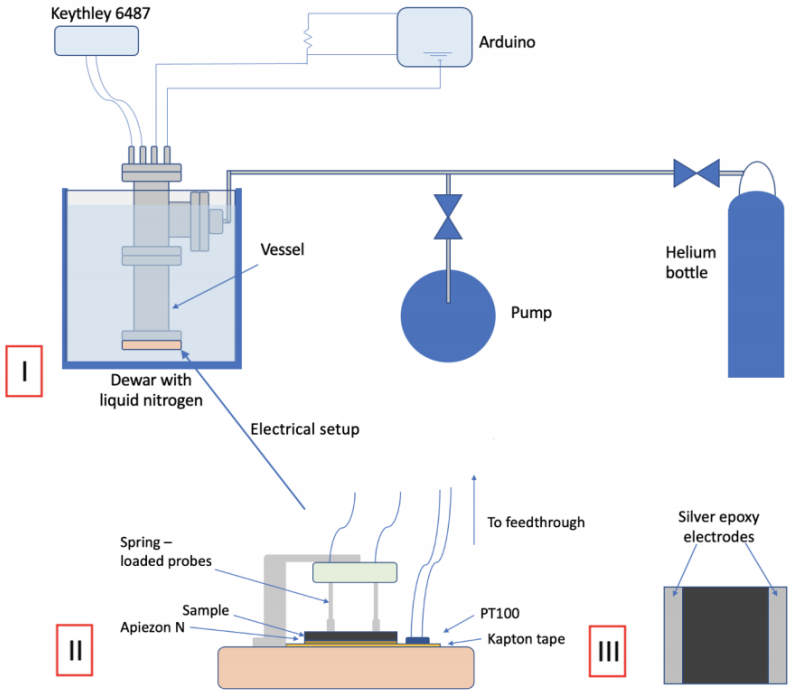

Figure 28: Scheme of the setup used for electrically characterizing DLC-coated samples. I) Full view: the sample is lying on the part of the vessel colored in orange. The vessel is immersed in LN_2 inside a Dewar, and connected to a pump and a helium bottle. It also communicates with a picoammeter and an Arduino via to the upper feedthrough. II) Close-up of the electrical setup inserted into the vessel: a Kapton layer electrically insulates the sample from the vessel bottom, while an additional layer of Apiezon N grease improves the thermal coupling. The sample is connected to two spring-loaded probes to measure the surface resistivity; close to the sample, a PT100 is used to measure the temperature inside the vessel. III) Top view of the sample: the two silver epoxy electrodes define a 1 cm^2. Figure taken from [113].

The experimental procedure was the following: the vessel was immersed into LN_2 until T = 77 K was measured in the PT100. At that point, it was taken from the bath and let warm up to room temperature through its thermal inertia ('drift' mode). A comparison with the PPMS results for the least resistive sample showed an agreement within 10%, confirming that a sufficiently good thermal equilibrium is reached in the DLC samples through this procedure (Fig. 29). Identical conclusions were extracted in a special PPMS run performed in drift mode, where the sample is also let to warm up in a helium atmosphere, unimpeded.

In the remainder of the text, error bars have been extracted from the standard deviation of two independent measurements.

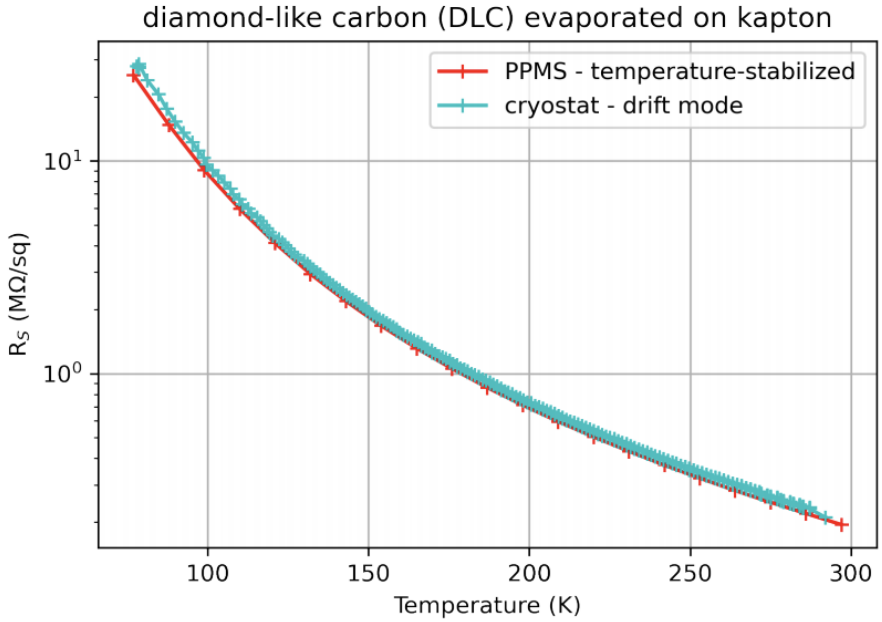

Figure 29: R-T curves for sample A as measured with PPMS (red) and with the dedicated setup depicted in Fig. 28, developed for high-resistivity measurements (light blue). Figure taken from [113].

Sample production In total, six DLC-coated Kapton samples of different surface resistivities were produced, named with letters A-F, and two DLC-coated FR4 samples, a and f, made with sputtering conditions similar to A and F. Different film thicknesses and resistivities were obtained by changing the sputtering time [113]. Kapton and FR4 are used regularly for manufacturing gaseous detectors, so they are interesting for understanding which role the substrate may play in the properties of the film.

I-V curves The characteristic I-V curves of the samples were obtained both at RT and LN_2 temperature (77 K), showing a perfect ohmic trend (Fig. 30 - lines represent the fit results). This simplifies the characterization as a function of temperature: the applied voltage was generally chosen to provide good precision for the resistivity measurement at LN_2 temperature (starting point of the scan).

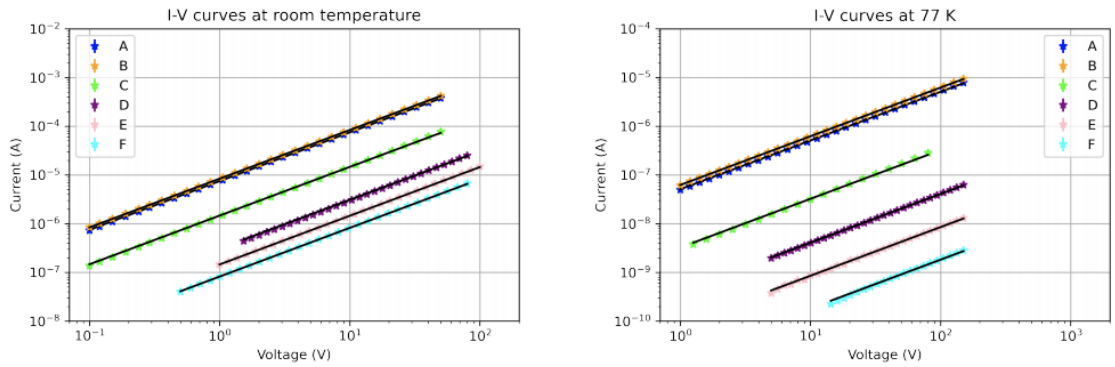

Figure 30: I-V curves of the DLC-coated Kapton samples at room temperature (left) and LN_2 temperature (right). Results for the FR4 samples (a, f) are not shown, but display the same trend. Super-imposed, the fit to I = V /R lines. Figure taken from [113].

R-T curves R-T curves are shown in Fig. 31, with error bars estimated from the deviation between two independent measurements taken with the setup described in Fig. 28 (for the A sample, the four available measurements from the PPMS were used instead).

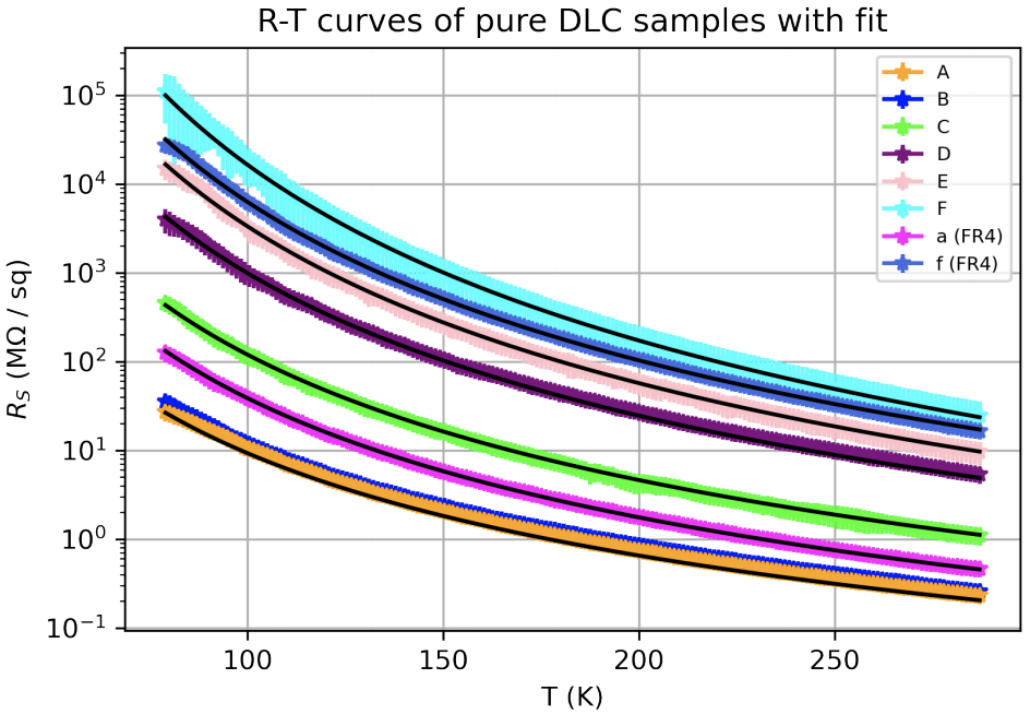

Figure 31: R-T curves for all DLC-coated samples, together with a fit to a 2-dimensional variable-range electron hopping model (black solid lines), following eq. 7.8. Figure taken from [113].

For thin coatings based on amorphous carbon it has been shown, using for instance percola-

tion theory, that the coating resistance is highly anisotropic with the following dependence:

$$R = R_{300} * \exp\left(\left(\frac{T_0}{T}\right)^a - \left(\frac{T_0}{300}\right)^a\right) \tag{7.8}$$

being $a = 1/4$ for the resistance across the bulk (3D) and $a = 1/3$ for the resistance over the surface (2D) [115]. The form of eq. 7.8 has been chosen such that the pre-factor R_{300} represents the surface resistance at 300 K (dubbed $R_{S,300}$ in the following). T_0 is an effective temperature given by:

$$T_0 = \frac{\beta}{k_B \cdot g \cdot r} \tag{7.9}$$

where k_B is the Boltzmann constant, β is an experimental factor of order 1, g is the density of states at the Fermi level of the film material, and r is the localization radius around it. Following the original naming by Mott, this type of conduction mechanism is widely known as variable range hopping (vrh), and we will consider it as the starting point for the interpretation of DLC data.

Ceramic materials for cryogenic applications A new material with tunable R_V was developed at the Instituto de Ceramicas de Galicia and produced for operation at LAr temperature [116]. This material, called Yttrium-Stabilized-Zirconium (YSZ), was a composite ceramic made of ZrO (zircon oxide) stabilized with Y_2O_3 (Yittrium oxide). The insertion of Fe_2O_3 (hematite) during the production process permitted to realize the value of the bulk resistivity according to the need, $10^9 < R_V < 10^{12}$ Ω·cm. Several ceramic plates with different bulk resistivities in this range were produced and their properties characterized up to LN_2 temperature (77 K).

Setup and Methodology After producing the ceramic plates, metallic electrodes were deposited on both faces of the resistive plates, and electrical measurements were conducted at room temperature and at cryogenic temperature, by immersing the resistive plates in a bath of LN_2. In the first case, current readout was performed with a multimeter while in the second case a picoammeter[12] supplied with voltages up to 500 V was used. These measurements permitted to assess the material properties and study the bulk resistivities of the ceramic materials in different conditions. In Fig. 32, the experimental setup built at University of Santiago de Compostela and used for the electrical measurements is illustrated:

[12] Keithley Model 6482

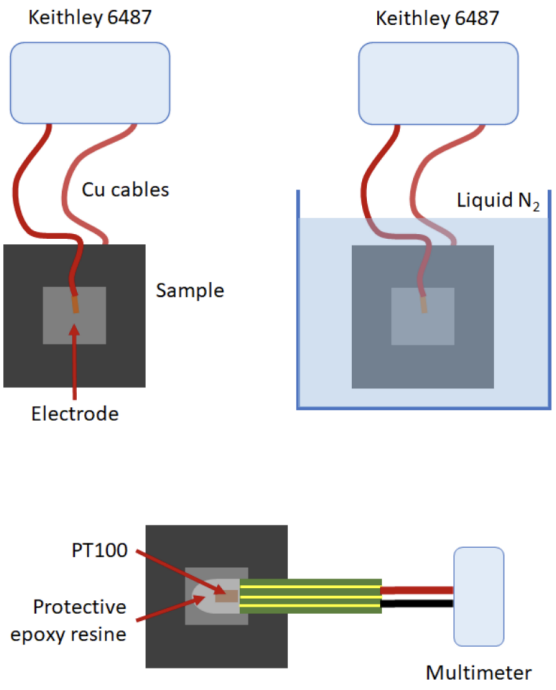

Figure 32: Description of the measurements of the electrical resistivity: electrodes were deposited on both faces of the sample and the readout was performed through a picoammeter. Top: configuration for RT (left) and LN_2 (right). Bottom: PT-100 epoxied to the sample for resistivity measurements as a function of temperature. Temperature measurements were directly recorded with a multimeter. Figure taken from [116].

For our purposes, it's worth mentioning:

- study of R_V as function of T;
- study of R_V as function of Fe_2O_3 concentration at 298 K and at 77 K;
- study of R_V as a function of the applied electric field E at 298 K and at 77 K;

The values for the currents and the sample resistivity were measured. R_V was measured by connecting the ceramic plate with electrodes realized on both sides of the sample with copper cables. Measurements were performed at controlled room temperature and at 77 K by introducing LN_2 in a small cryostat. To measure R_V as a function of T, a temperature sensor PT100 was fixed in the proximity of the ceramic plate and the T-R transient was recorded in drift mode after removing the sample from the LN_2 bath.

Results In Fig. 33, the bulk resistivity of several ceramic plates with different Fe_2O_3 concentrations is reported as a function of temperature, from 77 K to 298 K.

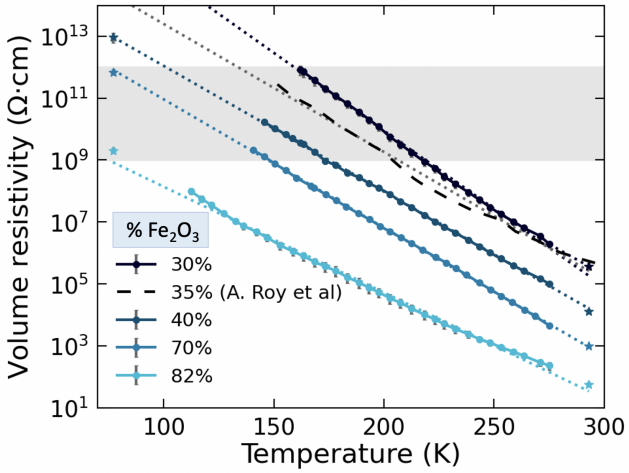

Figure 33: Characterization of the volume resistivity as a function of temperature for several ceramic plates with different Fe_2O_3 concentrations. Figure taken from [116].

It is possible to observe that the trend of R_V shown in the logarithmic scale linearly (exponentially, in the linear scale) decreases with increasing temperature. Experimental points match quite closely the dashed lines, connecting the points at 77 K to the ones at 298 K. The sample with a concentration in weight of 70% Fe_2O_3 is the only one that shows a value of bulk resistivity in the desired range, e.g. 10^9-10^{12} Ω·cm, at 90 K [21].

In Fig. 34, the bulk resistivity of several ceramic plates as a function of Fe_2O_3 concentration measured at different temperatures is reported. Solid lines represent measurements taken at a stabilized temperature, dashed lines were used to linearly connect the measurement points taken at a stabilized temperature over an evolving temperature transient. The value of R_V corresponding to a 30% Fe_2O_3 concentration at 77 K is outside the measurable range provided by the picoammeter. Also, the R_V values for a pure YSZ sample and for a pure Fe_2O_3 sample measured at 298 K are reported. For intermediate temperatures, dashed lines connect measurements that were taken in a non-stabilized temperature configuration.

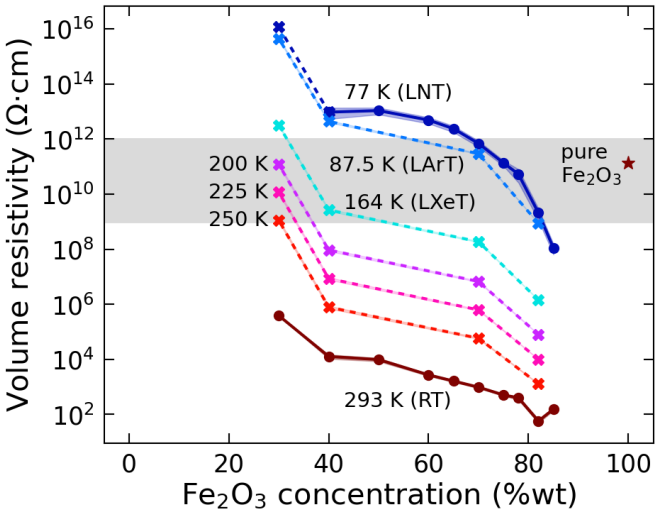

Figure 34: Characterization of the bulk resistivity as a function of Fe_2O_3 concentration measured at different temperatures. Figure taken from [116].

It is interesting to note how the mixture of two materials with R_V in the range MΩ-GΩ could give rise to a material whose R_V can be in the Ω scale. It is clear that the R_V of these YSZ/Fe_2O_3 can be tuned by varying the concentration of Fe_2O_3. It is also possible to note that the change in R_V with Fe_2O_3 concentration shows the same trend both at stabilized and at not stabilized temperatures. It is possible to conclude that a sample suitable for operation at 90K should possess a Fe_2O_3 concentration in the range 65-78% in weight.

In Fig. 35, the bulk resistivity of several ceramic plates with different Fe_2O_3 concentrations is reported as a function of the applied electric field across the plate at 298 K, left, and at 77 K, right.

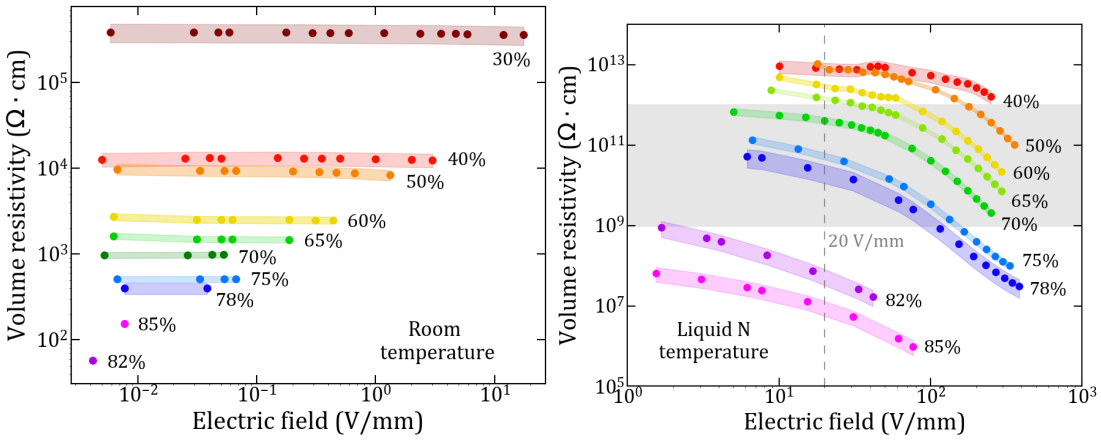

Figure 35: Characterization of R_V as a function of the applied electric field across the ceramic plates for different concentrations of Fe_2O_3, comprised in the range 40-85% in weight, measured at **Left:** 298 K, **Right:** 77 K. Figure taken from [116].

It is possible to observe that, systematically, the higher the Fe_2O_3 concentration is, the lower the measured R_V for the same applied electric field. In Fig. 35, left, a flat trend of R_V with E was measured. In Fig. 35, right, at low-applied electric fields, R_V tends to saturate (ohmic regime) while at high-applied electric fields, R_V tends to deviate from the flat trend and decrease. The investigated samples that at 77 K showed a value of R_V in the desired range of 10^9-10^{12} Ω·cm were the ones with 70%, 75% and 78% Fe_2O_3. It is reasonable to expect that these samples be adequate also at 90 K.

Carbon nanotubes-doped 3D-printed materials In addition to ceramic materials, thermoplastic materials made of Acrylonitrile Butadiene Styren (ABS) and of Polyethylene Terephthalate Glycol PETG, doped with carbon nanotubes CNT, were found to be a suitable alternative. These materials are commonly used for 3D-printing purposes. Several samples were fabricated for testing with thicknesses of 1.6 mm and 0.6 mm. The characterizations of the material properties in terms of R_V as a function of the electric field at RT and at LN_2 temperature (77 K) were done using the Electric Transport Measuring System (ETMS) installed at the Department of Chemical Research Support at the Weizmann Institute of Science. Electrical measurements were carried out in the micro-manipulated cryogenic probe station[13] using source-measure units[14] included in the semiconductor characterization system[15]. The results of the R_V vs E characterizations of both samples are reported in Fig. 36:

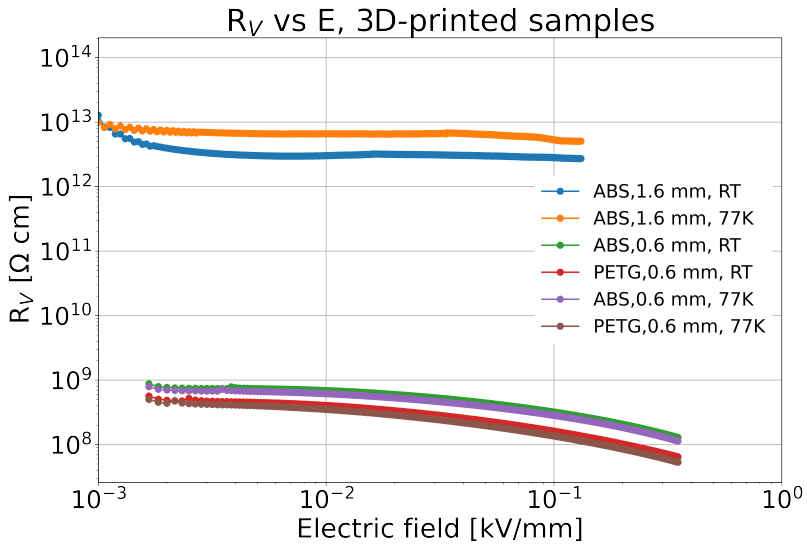

Figure 36: Characterization of bulk resistivity R_V of ABS samples (0.6 mm thick and 1.6 mm thick) and of a PETG one (0.6 mm thick) as a function of the applied electric field across the resistive plate at RT and at LN_2 temperature (77K).

[13] Janis Research Company, Model ST-500-2
[14] 4200-SMU
[15] Keithley Instruments, Model 4200A-SCS

One can observe that the 1.6 mm thick ABS sample develops large resistivity values, $R_V \sim 7x10^{12}$ Ω·cm at 90 K; the 0.6 mm thick samples reach $R_V \approx 10^9$Ω·cm for the ABS and $R_V \sim 6x10^8$Ω·cm for the PETG at 90 K. Unlike other materials previously investigated [21, 117], it was observed that R_V is not strongly temperature dependent. The application of an electric field across the plate results in a decrease of R_V, up to an order of magnitude for ~200 V. Prior to operation in cryogenic conditions, the materials were tested in an RPWELL detector assembly operated at room temperature in $ArCO_2$ 93:3 under x-rays irradiation. The results of this detector characterization will be reported in a dedicated publication.

7.2.2 Operations at cryogenic temperature

Setup During this study, four MPGD structures were investigated: RWELL, RPWELL, THWELL and THGEM [60]. A schematic picture of the investigated structures is shown in Fig. 37.

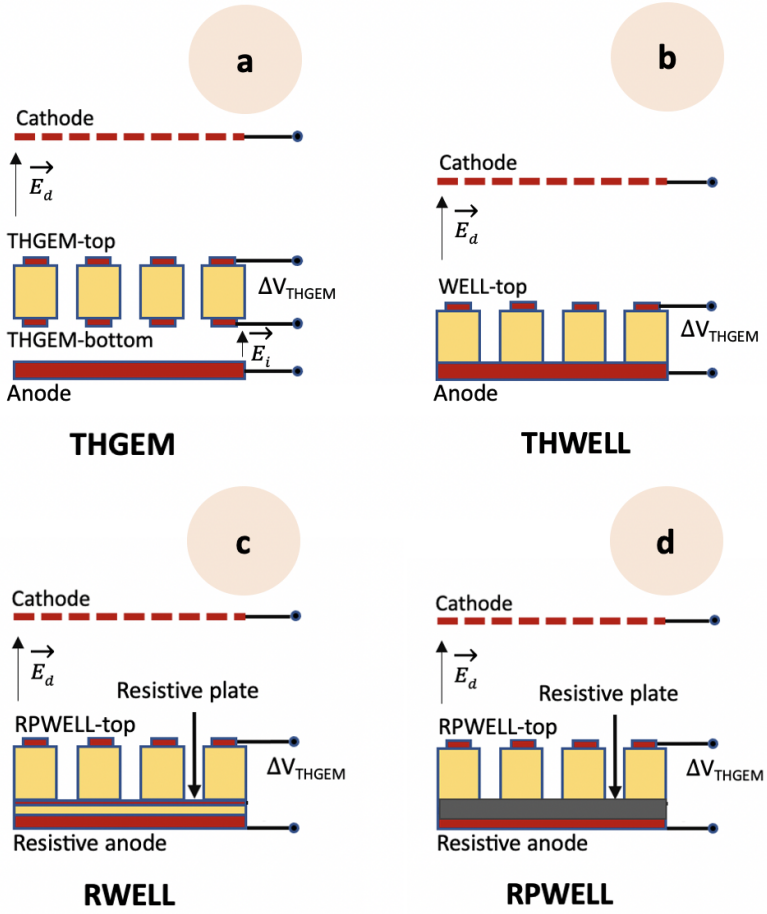

Figure 37: Scheme of **(a)** a THGEM (LEM) detector followed by an induction gap and a readout anode; **(b)** a THWELL detector, with a metallic anode at its bottom; **(c)** a RWELL detector, with a thin-film resistive anode decoupled from the readout electrode by an insulating plate; **(d)** a RPWELL detector. In all four cases the drift gap was equal to 15 mm and the electrode (double-sided in a) and single-sided in b), c) was 0.8 mm thick.

The first investigated configuration consisted of a double-sided 3x3 cm^2, 0.8 mm thick THGEM (0.5 mm diameter holes distributed in a hexagonal pattern with 1 mm pitch, and ~0.1 mm hole rim) followed by an induction gap of 2 mm; and an induction field E_i = 5 kV/cm (see Fig. 37a). In all the cases, the drift field was E_d = 0.5 kV/cm. The second structure was a 0.8 mm thick THWELL detector: a 3x3 cm^2, 0.8 mm thick single-sided THGEM structure with the same geometry directly coupled to a metallic anode (see Fig. 37b). The RWELL was realized with a 3x3 cm^2, 0.8 mm thick single-sided THGEM electrode pressed onto a metallic anode via a resistive layer deposited on a 0.1 mm thick Kapton insulating foil (see Fig. 37c). The responses of RWELL configurations with lower resistivity (e.g., R_S^{DLC} ~165 kΩ/□ at 298 K and R_S^{DLC} ~10MΩ/□ at 90 K) were found similar to those of non-resistive readouts and thus are not reported here. In Table 6, the

values for the relevant R_S at 298 K and at 90 K are given.

DLC layer	R_S^{DLC} at 298 K	R_S^{DLC} at 90 K
Sample 1	~ 14 MΩ/□	~ 20 GΩ/□
Sample 2	~ 1 MΩ/□	~ 200 MΩ/□

Table 6: Surface resistivity at 298 K and at 90 K for two DLC samples with different R_S.

To create electrical contacts, the DLC-coated Kapton foil was fixed onto a PCB and the DLC layer was connected to two sides of copper lines using cryogenic conductive epoxy[16]. An electrically-insulating cryogenic epoxy[17], was subsequently used to encapsulate the components (see Fig. 38).

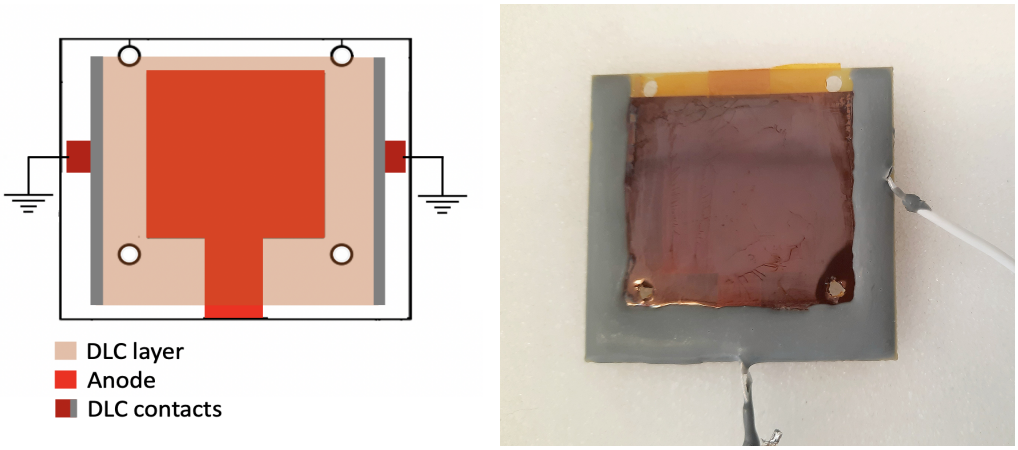

Figure 38: **Left:** scheme of a resistive anode composed by a DLC layer fixed on a PCB board with electrically-insulating cryogenic epoxy; **Right:** resistive anode used in the experiments, with the electric connections encapsulated with cryogenic conductive epoxy and connected with coaxial wires.

The RPWELL was realized with a 3x3 cm^2, 0.8 mm thick single-sided THGEM electrode pressed onto a metallic anode via a resistive plate (see Fig. 37d). In Table 7, the values for the relevant R_v at 298 K and at 90 K are given.

[16] Master Bond EP21TDCS-LO
[17] Stycast 2850FT

Resistive plate	Thickness	R_v at 298 K	R_v at 90 K
75% Fe_2O_3/YSZ	2 mm	$5x10^2\Omega$·cm	$8x10^{10}\Omega$·cm
65% Fe_2O_3/YSZ	2 mm	$2x10^3\Omega$·cm	$10^{12}\Omega$·cm
ABS	1.6 mm	$7x10^{12}\Omega$·cm	$7x10^{12}\Omega$·cm
ABS	0.6 mm	$10^9\Omega$·cm	$10^9\Omega$·cm
PETG	0.6 mm	$6x10^8\Omega$·cm	$6x10^8\Omega$·cm

Table 7: Surface resistivity at 298 K and at 90 K for different resistive plate samples.

All the electrodes (i.e. cathode, THWELL, resistive layer/plate and readout electrode) were biased by a HV power supply[18] or via a charge-sensitive preamplifier[19]. The latter was equipped with a protection circuit composed of discharge-suppressor elements in parallel and a series resistor of 220 Ω. The time evolution of the detector gain was studied in order to establish stable operation conditions. For gain stabilization studies, the signals from the preamplifier were fed to an amplifier[20]; the amplified signals were digitized by a multi-channel analyzer[21]. For all the other measurements, waveforms from the preamplifier were acquired using a digital oscilloscope[22] and post-processed using dedicated Matlab scripts. Histograms of the preamplifier signal amplitude were also acquired using the oscilloscope. Currents from the electrodes were read out by a digitizer[23] and monitored using LabVIEW SignalExpress [118].

Cryostat The measurements were performed in a dedicated LAr cryostat, WISArD (Weizmann Institute of Science liquid Argon Detector) described in detail in [77]. In all the experiments, an ^{241}Am source emitting 5.5 MeV alpha particles with a rate of about 10 Hz was installed on a metallic plate cathode at a distance of 15 mm from the multiplying electrode. The source emission was opportunely confined using a metallic collimator of 4 mm thickness and 5 mm diameter. A 12 μm Mylar foil was installed at the collimator's emitting face to attenuate the alpha energy to about 4 MeV. This granted full containment of the alpha-particles in the drift volume (≈10 mm range in gaseous argon at 90 K, 1.2 bar calculated with SRIM [119]). Each detector configuration was operated in the saturated vapor phase of argon at 90 K. This was realized by inserting the detector assembly inside a Teflon cup, as depicted in Fig. 39. The level of the liquid was monitored using temperature sensor located in the proximity of the detector anode. This prevented the liquid from penetrating into the detector region. The chosen operation within the vapor enclosed in the cup rather than in the liquid phase permitted avoiding electron recombination and

[18] CAEN N1471H
[19] Cremat: Model CR-110 with CR-150-R5 evaluation board
[20] Ortec Model 450
[21] Amptek MCA 8000D
[22] Tektronix MSO 5204B
[23] NI USB-6008

extraction (see Fig. 3 in [18]), thus yielding a higher number of ionization electrons and facilitating the measurements. The temperature inside the system was constantly monitored using a temperature controller[24]. A conceptual scheme of a cryogenic setup with a RWELL/RPWELL detector is depicted in Fig. 39.

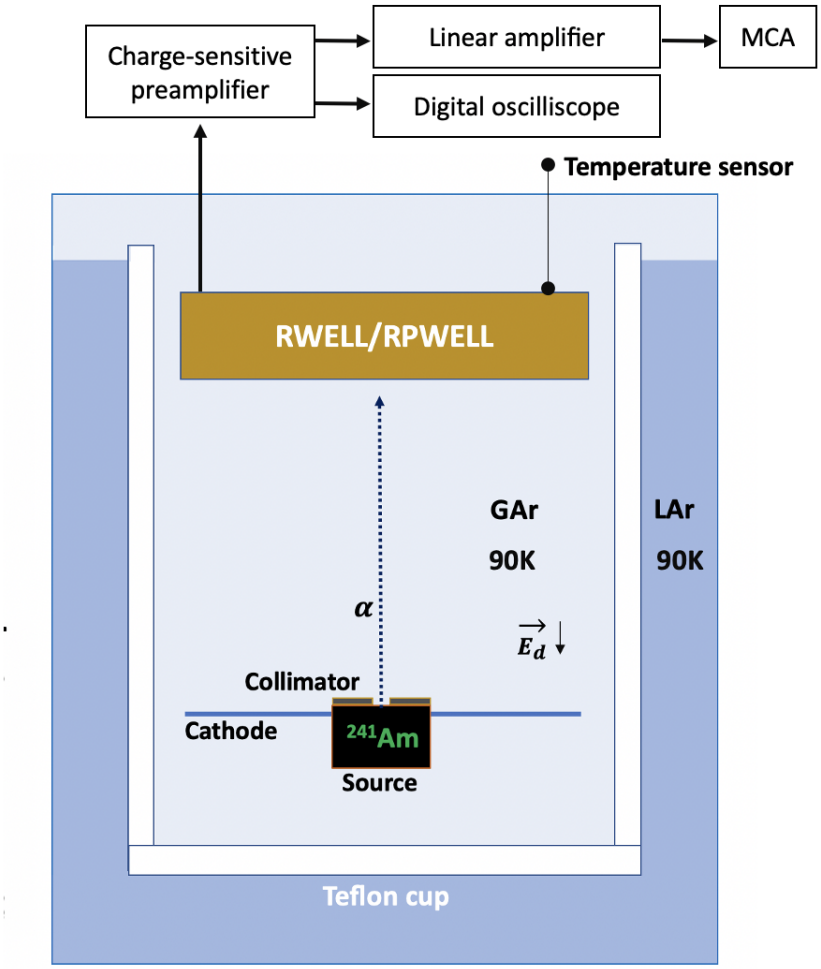

Figure 39: Scheme of the cryogenic setup for investigating the detectors (here an RWELL/RPWELL). The assembly and the involved physical processes are detailed. The detector was operated at 90K, 1.2 bar.

Methodology

Gain estimation The 4 MeV alpha particles (attenuated ^{241}Am source) generate ~10^5 primary electrons in the drift region mostly in a track perpendicular to the detector surface (W-value of 26.3 eV in Ar [120]). These are drifted towards the THGEM holes under

[24]CryoCon model 24

a field E_d = 0.5 kV/cm. Increasing the bias across the multiplier electrode, defined as ΔV_{THGEM} results in a high electric field within the holes, allowing for the onset of avalanche multiplication of the primary charges. The amplification factor (i.e. detector gain) increases exponentially with ΔV_{THGEM}, typically in the range of 2.7-3.2 kV in our configuration. Charge from avalanche electrons is evacuated to the ground through the anode in the THGEM and THWELL multipliers, across the resistive-anode surface in the RWELL and through the resistive plate in the RPWELL (see Fig. 37). An electrical signal is induced onto all the electrodes by the movement of charges (electrons and ions) during the entire process, as described by the Shockley-Ramo theorem [121]. We refer to the collection signal as the one induced by the movement of the primary charges in the drift gap. This was recorded from the cathode in specific measurements where ΔV_{THGEM} = 0 kV. We refer to the amplification signal as the one induced by the movement of the avalanche charges. It was recorded from the anode with ΔV_{THGEM} in the range of detector operation. The effective detector gain can be estimated by the following normalization:

$$G_{Eff} = \frac{P_{Amplif}}{P_{Coll}} \tag{7.10}$$

where P_{Amplif} and P_{Coll} are the Gaussian mean values of the spectra of amplification and collection signals, respectively. Notice that, the anode signal of a THGEM operated in multiplication mode is mostly due to the fast movement of electrons within the induction gap - typically of 4 μs in our setup at cryogenic temperature - whereas in THWELL and RWELL the signals contain both electron and slower ion components [49]. For this reason, a linear amplifier shaping time of 10 μs was used for the measurements. It is important to mention that the resistive anode, decoupled from the readout electrode by a thin insulator (here 0.1 mm thick Kapton), causes a small decrease in the effective gain because of a reduced weighting potential. This effect is negligible when the insulator is thin [62].

Gas purity Gas purity plays a crucial role in large-volume LAr-TPCs, where a sub-ppb level of electronegative impurities is targeted [122] in order to minimize electron capture during the drift in the liquid or gas. The maximum achievable gain of gaseous multipliers in Ar is strongly affected by the presence of impurities, quenching avalanche-induced VUV photons, that are responsible for secondary avalanche feedback [123]. Therefore, for a realistic comparison of the multipliers, they should be investigated in similar conditions, in very pure Ar vapor. For this reason, prior to any measurement, the system was vacuum-pumped for at least 12 h reaching a pressure of $\sim 1\times10^{-4}$ mbar. A residual gas analyzer[25] was used to measure the level and composition of residual impurities. It was found that the main sources of contamination were H_2O, Ne, HF, N_2, CO. When filling the system with ~1 bar of Ar, the residual impurities got diluted to a concentration of 0.1 ppm. This should be compared with the level of impurities in the Ar gas bottle: 99.999% with

[25] SRS RGA200

$H_2O \leq 2$ ppm, $O_2 \leq 2$ ppm, $C_nH_m \leq 0.5$ ppm and $N_2 \leq 5$ ppm, as specified by the producer.

Liquefaction and thermal stabilization The cryostat was filled up with liquid argon until a temperature of 90 K was measured in the gaseous phase at the level of the assembly (temperature sensor in Fig. 39). The pressure inside the cryostat throughout all the operations corresponded to the saturation pressure P_s = 1.2 bar at 90 K. In order to grant thermal stability, according to our experience, the detector was not operated during the first six hours following liquefaction. During this period, the gas was purified with a hot getter[26] at 2 L per hour for at least 24 hours, in order to grant a nominal impurity content of the order of 1 ppb.

Gain stabilization and voltage scan The gain of each detector configuration was characterized by scanning the voltage across the amplification structure (e.g. for the RWELL, ΔV_{RWELL}), in the operational range while E_d = 0.5 kV/cm was kept constant. An increase of ΔV_{RWELL} corresponded to an increase of the detector gain followed by a small reduction (about 20%), up to stabilization after several hours. This effect is due to the accumulation of charges on the THGEM's insulating substrate (holes' walls and rims) [124, 125]. For each voltage configuration, a minimum of 10^2 spectra of 120 s each were acquired. In Fig. 40, the gain stabilization for the RWELL detector operated at 90 K, 1.2 bar is shown as an example. ΔV_{RWELL} was set to 2.7 kV, sufficient to obtain well-defined spectra above noise, and it was subsequently increased up to 3.175 kV in steps of 50 V or 100 V. After a certain value of ΔV_{RWELL}, the detector entered a region of electrical instability. This was different for each detector configuration. For the RWELL, discharges were quenched by the resistive layer and the detector could be operated stably despite a loss in energy resolution due to small gain fluctuations (e.g. ΔV_{RWELL} = 3.15 and 3.175 kV in Fig. 40). Three regions of operation were identified: i) discharge-free behavior up to 3 kV, ii) stable operation in the presence of quenched discharges for 3 kV < ΔV_{RWELL} < 3.175 kV and iii) presence of constant currents above 3.175 kV. The measurement was stopped when the detector entered the latter region.

[26] Entegris HotGetter PS3-MT3-R-2

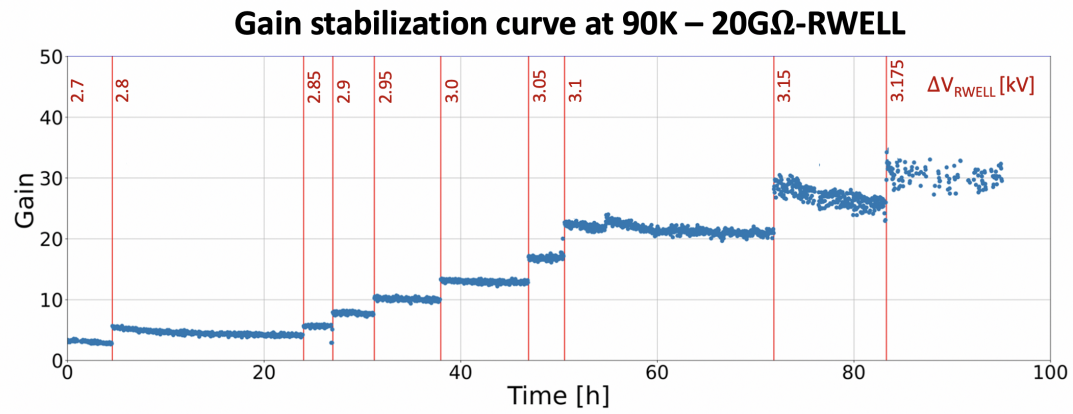

Figure 40: Gain stabilization for the 20GΩ-RWELL detector operated with alpha-particles at 90 K, 1.2 bar. The voltage configurations are indicated by red vertical bars and the corresponding values in kV are reported above them. The gain decreased over time (20% gain reduction) until stabilization. For 3 kV < ΔV_{RWELL} < 3.175 kV, the detector operated in the presence of quenched discharges. Gain fluctuations are also visible at ΔV_{RWELL} = 3.15 and 3.175 kV.

For the THGEM and THWELL, a single discharge event was able to remove charging-up making a stable gain operation not viable. Moreover, the discharge currents were large enough to inhibit the power supply operation until restarted. Two regions of operation were identified: discharge-free behavior up to ΔV_{THGEM} = 3.2 kV and ΔV_{THWELL} = 2.9 kV, and an unstable region of intense discharges above it; there the measurements were stopped.

For the 75% Fe_2O_3-RPWELL, the gain stabilization was conducted in a similar way, with E_d = 0.5 kV/cm and scanning ΔV_{RPWELL} = 2.7 - 3.28 kV, as reported in the blue bar in Fig. 41, top. In parallel, power supply currents were monitored from the cathode, RPWELL top, and anode using SignalExpress, as reported in Fig. 41, bottom, to correlate gain instabilities with the presence of discharges in the RPWELL. The results of the 65%Fe_2O_3-RPWELL and of the thermoplastics-RPWELLs are reported in the discussion and presented for reference in the Appendix.

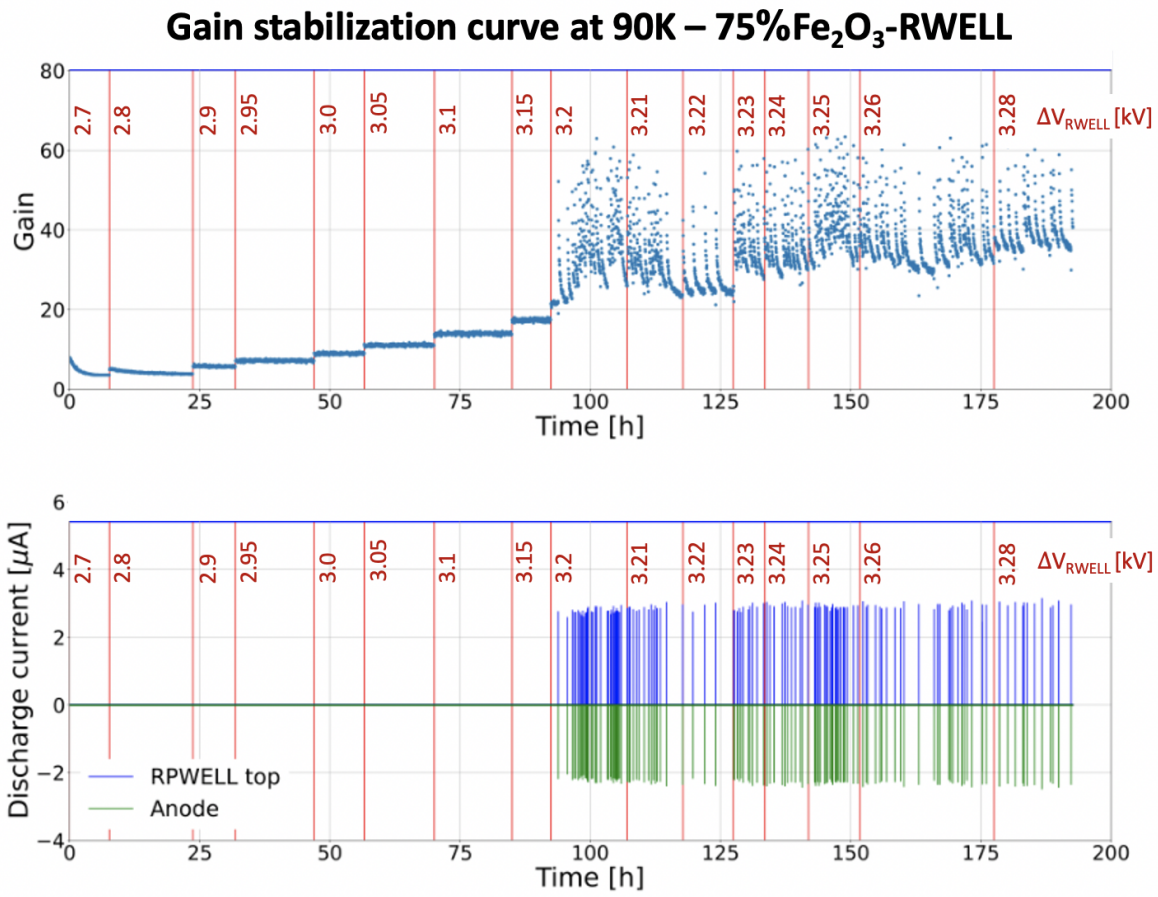

Figure 41: **Top**: Gain stabilization curve of approximately 200 hours of a 75%Fe_2O_3-RPWELL operated at 90 K, 1.2 Bar. The voltage configurations are indicated by red vertical bars and the corresponding values are reported above them. **Bottom**: Power supply currents recorded from the RPWELL top electrode (blue) and anode (green) for a 75%Fe_2O_3-RPWELL operated at 90 K, 1.2 Bar. Note the presence of discharges above ΔV_{RPWELL} = 3.2 kV on.

It is possible to observe that, during the initial stabilization at ΔV_{RPWELL} = 2.7 kV, there was a gain drop of ~ 60% due to the charging-up of the electrode substrate [124, 125]. No further stabilization transients were recorded up to ΔV_{RPWELL} = 3.2 kV. At higher potentials, instabilities appeared; they were due to the presence of discharges capable of affecting the equilibrium charge distribution stabilized in the THGEM holes (charging-up). Recovery time after a discharge was ≈30 mins. The detector was able to sustain these discharges for 3.2 kV < ΔV_{RPWELL} < 3.28 kV but gain stability was severely affected. In Fig. 42 depicts an expanded gain stabilization graph in the presence of discharges.

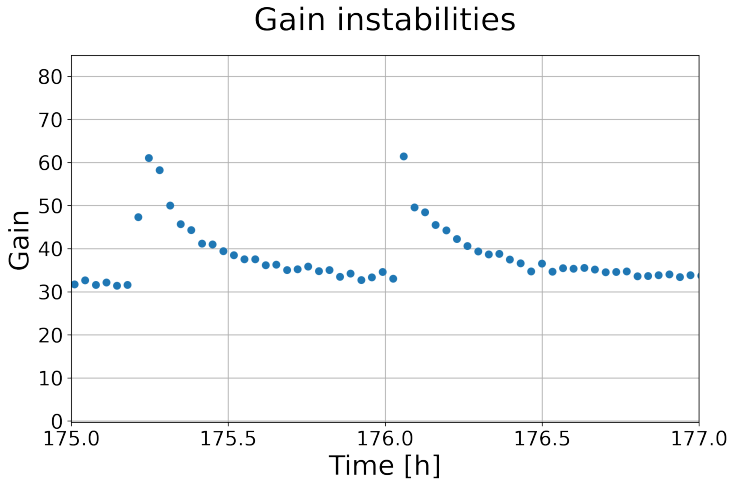

Figure 42: Expanded view of the gain stabilization curve of during a 2 hours period, in 75%Fe_2O_3-RPWELL operated in Ar at 90 K, 1.2 Bar at ΔV_{RPWELL} = 3.26 kV: the presence of instabilities seems to affect the gain stabilization for ≈ 30 mins.

Above ΔV_{RPWELL} = 3.28 kV, a discharge pile-up induced a full detector tripping and the operation was interrupted.

Collection signals, spectra, and efficiency The process of primary charge drift and collection is independent of the adopted detector configuration. An average collection signal from a dataset of 10^3 waveforms is shown in Fig. 43, left. The average risetime of the typical collection signal (around ~5.5 μs) is in agreement with the theoretical value (around ~5.8 μs) calculated for this geometry within a 5% error (from Magboltz [126], v_e = 2.6 mm/μs at 90 K, 1.2 bar with E_d = 0.5 kV/cm). In Fig. 43, right, a typical spectrum of collection-signal amplitudes recorded for a sample of 4.5 × 10^3 waveforms is shown. The spectrum was normalized to its maximum and calibrated by injecting a known amount of charge through a 2 pF capacitor. The mean value of the distribution corresponds to ~1.5 x 10^5 primary electrons.

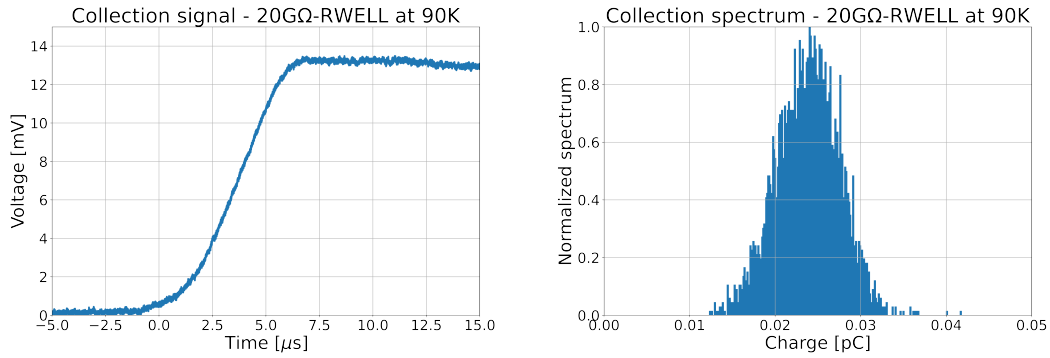

Figure 43: **Left**: Average charge-collection waveform from the preamplifier, for an RWELL detector operated with alpha-particles at 90 K, 1.2 bar; **Right**: signal amplitude spectrum calibrated to charge.

In Fig. 44, left, a scan of the WELL detector operated at 90 K, 1.2 bar was carried out in terms of the anode-signal amplitude from the preamplifier as a function of ΔV_{WELL}, with E_d = 0.5 kV/cm. The drift cathode-signal amplitude recorded at ΔV_{WELL} = 0 kV and E_d = 0.5 kV/cm, is also reported for comparison; it is the same for the RWELL (Fig. 43, left). Each point was recorded using the digital oscilloscope and represents the mean value of the signals' amplitudes distribution, each one containing 10^3 entries. The uncertainties were extrapolated as the σ of the charge distributions. One can observe in Fig. 44, right, a rise of the collection efficiency reaching a plateau at about ΔV_{WELL} = 1.2 kV, remaining constant until the onset of charge multiplication at about ΔV_{WELL} = 1.5 kV. A charge gain ~8 can be derived from Fig. 44, left, at ΔV_{WELL} = 2.9 kV.

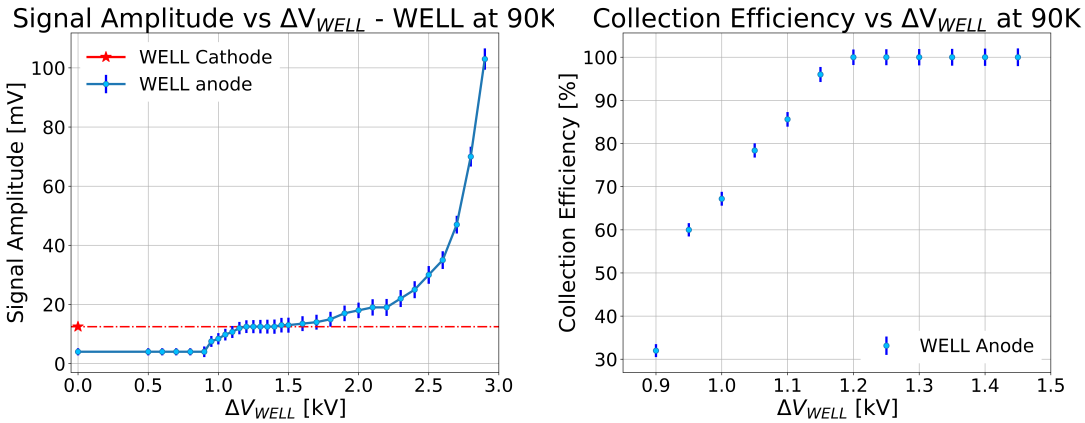

Figure 44: **Left**: Scan of the WELL detector operated at 90 K, 1.2 bar in terms of the anode signals' amplitudes from the preamplifier as a function of ΔV_{WELL}, with E_d = 0.5 kV/cm. The cathode signal amplitude is also reported for comparison (see red star); **Right**: WELL collection efficiency as a function of ΔV_{WELL}, with E_d = 0.5 kV/cm.

Thus, for $\Delta V_{\mathrm{WELL}} \geq 1.5$ kV, the detector operates with full collection efficiency and,

consequently, G_{Eff} (defined in Eqn. 7.10) is equivalent to the absolute detector gain G_{Abs}. These conclusions apply to the RWELL case as well.

20GΩ-RWELL at 90K - Amplification signals and spectra In Fig. 45, left, averages of $\sim 10^3$ normalized waveforms recorded from the RWELL anode are shown. The detector voltage was scanned in the range ΔV_{RWELL} = 2.7-3.2 kV. The waveforms were prepared for averaging by applying a smoothing moving-average algorithm and subsequently by removing the signal pedestal, normalizing to the waveform maximum and subtracting time offsets at a fixed amplitude fraction. In Fig. 45, right, the calibrated charge spectra are shown. The histograms were recorded using the MCA and each one contained $\sim 5 \times 10^3$ entries. All spectra were normalized to their area and to the maximum at ΔV_{RWELL} = 2.7 kV. The low-energy tail is attributed to the partial energy deposition of alpha particles exiting the collimator at large angles.

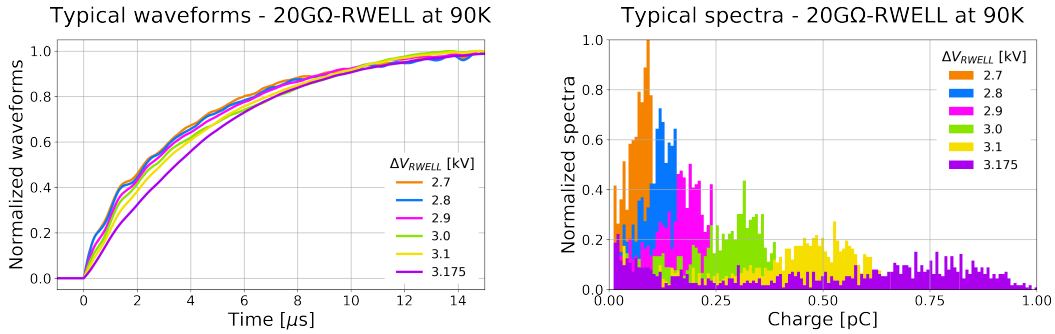

Figure 45: **Left**: average waveforms recorded from a RWELL detector irradiated with α-particles at 90 K, 1.2 bar; **Right**: example of reconstructed α-spectra obtained in the same conditions.

For detailed risetime studies, a waveform-by-waveform analysis was made, and the most probable value was taken from the risetime distribution (defined from 10% to 90% of the signal maximum). An increase of the risetime as a function of ΔV_{RWELL} was observed in Fig. 46 (orange circles), from around 4 μs to 8 μs. A drift velocity analysis was carried out using the technique introduced in [127] for α-particles and a constant value of 2.52 $\cdot 10^3$m/s at E_d = 0.5 kV/cm was found (about 30% less than the nominal value). This confirms that the main contribution to the observed risetimes comes from the α-particles emission, while the additional increase with ΔV_{RWELL} stems from the detector response. A quadratic subtraction of the zero-field risetimes, performed in order to isolate the effect, is superimposed in Fig. 46 (blue circles). The time constant associated with photon feedback [128, 129] is shown for illustration (magenta dashed line). Even if a good match is visible, the observed agreement might be coincidental. Field modifications due to ion space charge or charge accumulation at the plate may induce a similar effect given that the contribution from the ion drifts to the total signal width is about 1 μs. Field reductions down to 20%, even if too extreme, would cause a similar increasing trend with ΔV_{RWELL}. Ion feedback from the cathode, in the timescale of ms, would lead to spurious signals that were only

present at ΔV_{RWELL} = 3.175 kV (up to 40% of the events, with a discharge rate of ≈ 1%). In closing, the exact mechanisms leading to the breakdown above this value could not be unambiguously elucidated.

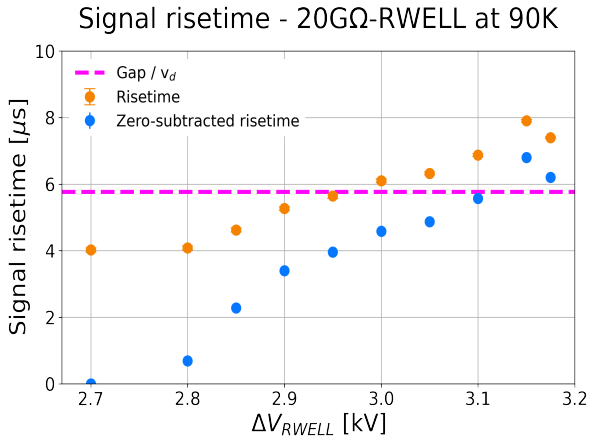

Figure 46: Most probable signal risetime as a function of the applied voltage for the RWELL detector operated at 90 K, 1.2 bar, with E_d = 0.5 kV/cm (orange circles). The zero-subtracted risetime (blue circles) and the photon feedback time constant (magenta dashed line) are also reported.

Fig. 47 depicts the RWELL gain as a function of ΔV_{RWELL} at different temperatures (presented in Fig. 2a of [79]). The gain uncertainties represent the gain variations of the stabilization curve. Since the gas pressure was kept constant along the experiments, in first approximation the gas density is only temperature-dependent, $\rho_g \sim T^{-1}$. The DLC resistivity decreased with increasing temperature, from 20 GΩ/□ at 90 K to 10 GΩ/□ at 100 K and 3.5 GΩ/□ at 115 K [113]. The detector characterization was performed first at 90 K, then the LAr level was reduced by warming up the system and extracting gas until the temperature reached the levels of 100 K and 115 K. The maximal achievable stable gain in the presence of quenched discharges was approximately 30 regardless of the temperature and DLC resistivity.

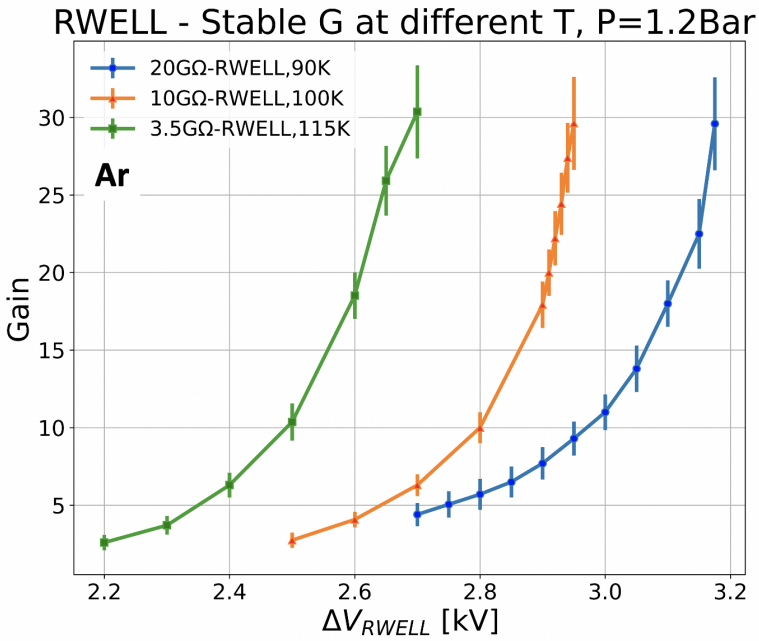

Figure 47: RWELL gain, measured in stable operation conditions, as a function of the applied voltage at different temperatures. The resistivity of the DLC layer at each temperature is also reported. Reprinted from [79].

The three curves manifest the same exponential trend, which is a feature of avalanche multiplication. Above a detector gain close to 18, the presence of quenched discharges was observed (≈0.25 μA); they did not prevent the RWELL operation and did not affect its performance. Above 3.2 kV, the appearance of constant currents led to the detector tripping.

75% Fe_2O_3-RPWELL at 90K - Amplification signals and spectra For each voltage configuration, a dataset of 5k waveforms was recorded. Typical average signals were reconstructed by applying a smoothing moving-average algorithm and subsequently by removing the offset and jitter. Each average waveform was normalized to its own maximum. In Fig. 48, left, the typical waveforms for 2.7 kV < ΔV_{RPWELL} < 3.15 kV are shown. In Fig. 48, right, the calibrated charge-amplitude spectra are shown. The histograms were recorded using the MCA, for 120 s each. All the spectra were normalized to their area and to the maximum at ΔV_{RPWELL} = 2.7 kV. The low-energy tail is attributed to the partial energy deposition of alpha particles exiting the collimator at large angles. With increasing voltage, the shape of waveforms and spectra was preserved, with no indication of distortions due to secondary effects.

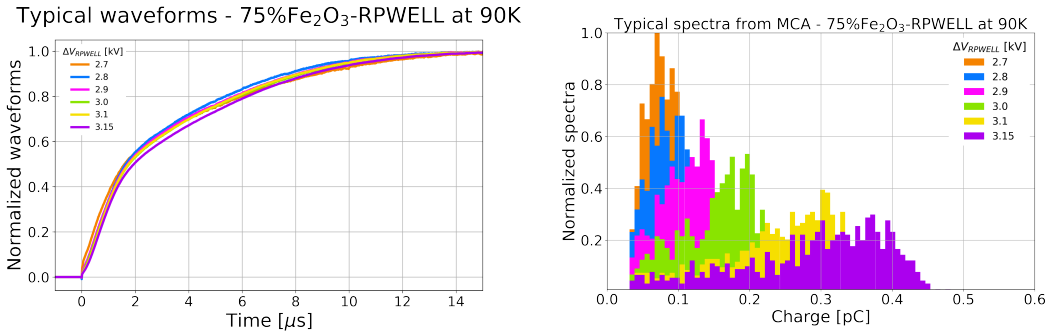

Figure 48: **Left**: Typical RPWELL signals recorded for 2.7 kV < ΔV_{RPWELL} < 3.15 kV at 90 K, 1.2 Bar; **Right**: Example of reconstructed α-spectra obtained in the same conditions.

Note also the well-defined "fast" and "slow" components in the waveforms, typical of WELL-like configurations [130]; the fast one, here of the order of several hundred ns, relates mostly to the movement of the electrons from the top of the hole toward the resistive plate, while the slow one, of more than ten μs, originates from the back-flow of ions in the opposite direction (Fig. 37d).

In Fig. 49, it can be observed that the signal risetime slowly increases from 6.1 μs at ΔV_{RPWELL} = 2.7 kV to 7.3 μs at ΔV_{RPWELL} = 3.15 kV; similarly, the risetime uncertainty decreased with ΔV_{RPWELL}, from ≈30 % to ≈14%, respectively. Compared to the RWELL case (see orange curve in Fig. 46), the RPWELL risetime for 2.7 kV ≥ ΔV_{RPWELL} < 3 kV was ≈30% higher, while for 3 kV ≥ ΔV_{RPWELL} ≤ 3.15 kV was in agreement with the RWELL's one. This difference observed at low-voltages was imputable to a lower S/N for the RPWELL detector.

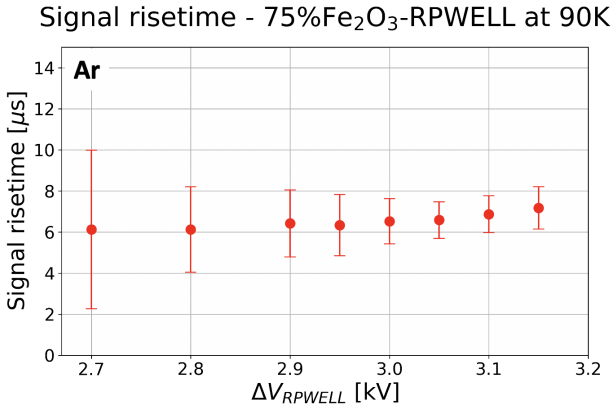

Figure 49: RPWELL signals risetime recorded for 2.7 kV < ΔV_{RPWELL} < 3.15 kV in Ar at 90 K, 1.2 Bar.

Comparative study Past studies with LEM structures in DP LAr-TPCs were carried out in different conditions: 87 K, 0.98 bar, cosmic muons, and unknown argon purity [122, 131]. Thus, their results in terms of maximum achievable gain can not be directly compared to the ones obtained in this study. In order to demonstrate the potential advantages of the resistive configurations, the RWELLs and RPWELLs detector response were compared with that of THWELL and THGEM (LEM) in the same experimental system, irradiation source and conditions, at 90 K and 1.2 bar. Note that the RWELL was operated with DLC anodes of 200 MΩ/□ and 20 GΩ/□ and the RPWELL with ceramic plates in 65%- and 75%- Fe_2O_3 concentrations. The data were recorded after gain-stabilization cycle in purified Ar (see above). In all cases, E_d was kept at 0.5 kV/cm and the induction field E_I in THGEM configuration was set at 5 kV/cm, as per DUNE's configuration [56].

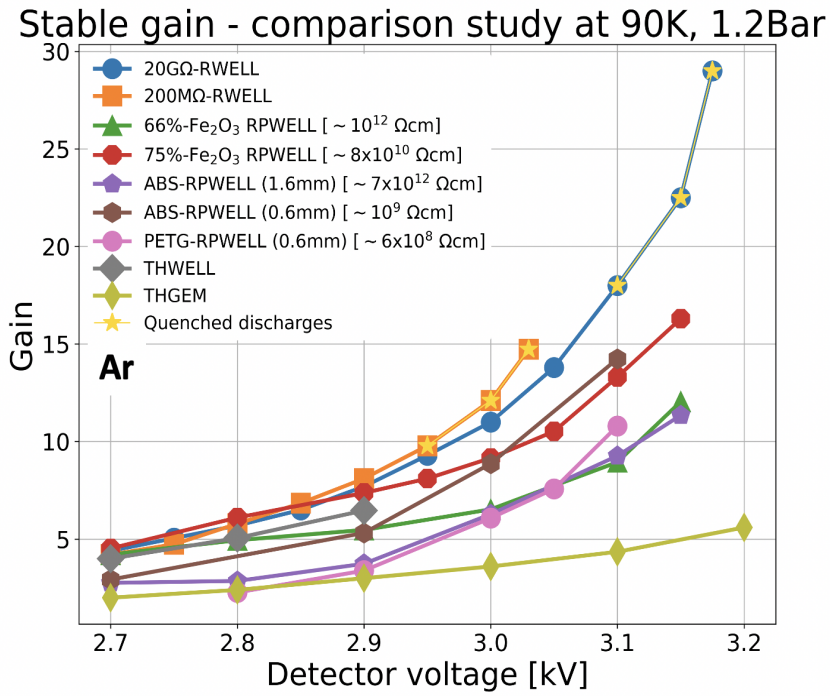

Figure 50: Comparison study showing the stable gain for a THGEM+2mm induction gap, a THWELL, a 200MΩ-RWELL, a 20GΩ-RWELL, a 65% Fe_2O_3-RPWELL, a 75% Fe_2O_3-RPWELL, the ABS-RPWELLs (with 0.6 mm and 1.6 mm thick plate) and a PETG-RPWELL, at 90 K and 1.2 bar. In all cases, the THGEM structure was 0.8 mm thick (see text).

Gain curves increase monotonically with ΔV_{THGEM} for all the investigated detectors as shown in Fig. 50. It is possible to observe that all the resistive detectors perform better than their non-protective counterparts.

The 20GΩ-RWELL was found to be the best configuration with a maximum gain of 30. The respective 2- and 4-fold gain increase of the RWELL configuration compared

to the THWELL (gain of ~8) can be explained by the discharge quenching features of the resistive layer. For the RPWELLs, the maximum gain, G ≈16, was reached with the 75%Fe_2O_3-RPWELL at ΔV_{RPWELL} = 3.15 kV. At the same operational voltage, the 65% Fe_2O_3-RPWELL and the 1.6 mm thick ABS-RPWELL reached G ≈12.

Discharges occurring in the two non-protected detectors, WELL and THGEM, generally led to the tripping of the detector and often damaged the preamplifier. In both RWELL configurations, the presence of quenched discharges was observed: at 10 < G < 15 for the 200 MΩ-RWELL and 18 < G < 30 for the 20 GΩ-RWELL. Discharges could be sustained throughout the detector operation without affecting the stable gain (for ~45 hours), the discharge charge (≈ 0.25 μC) was ~15-fold lower than the one of unprotected detectors (≥ 3.75 μC), thus destructive effects to the electronics were strongly mitigated. Beyond ΔV_{RWELL} = 3.05 kV for the 200 MΩ-RWELL and ΔV_{RWELL} = 3.175 kV for the 20 GΩ-RWELL, both RWELL configurations were not operable due to the presence of constant currents. For the ceramic RPWELLs and the 1.6 mm thick RPWELL, discharges started occurring above V_{RPWELL} = 3.15 kV and were measured by monitoring currents from the power supply. The detectors continued operating in the presence of discharges but gain stability was lost (Fig. 42). The measurements were interrupted arbitrarily at ΔV_{RPWELL} = 3.28 kV for the 75%Fe_2O_3-RPWELL, at ΔV_{RPWELL} = 3.25 kV for the 65%Fe_2O_3-RPWELL and at ΔV_{RPWELL} = 3.3 kV for the 1.6 mm thick ABS-RPWELL; the ABS-RPWELL and the PETG-RPWELL based on a 0.6 mm thick plate were both able to operate in discharge-free mode up to ΔV_{RPWELL} = 3.1 kV reaching G ≈14 and G ≈11, respectively. Beyond this voltage configuration, discharges led to the tripping of the detector like in the non-protected case. This behavior suggests a connection between the detector quenching properties and the plate resistance, and advocates for further investigation.

Discharge probability We define the discharge probability P_d as the number of discharges occurring per event per unit of time:

$$P_d = \frac{N_d}{E_r \times t}$$

where N_d represents the number of discharges recorded, E_r is the rate of detected events and t is the measurement time. E_r was measured using a surface-barrier silicon detector[27]. In Fig. 51, the discharge probability of the RWELL is depicted as a function of gain at different temperatures (90 K - 200 MΩ/□, 90 K - 20 GΩ/□, 100 K - 10 GΩ/□, 115 K - 3.5 GΩ/□).

[27]Ortec F Series Partially Depleted Silicon Surface Barrier Radiation Detector

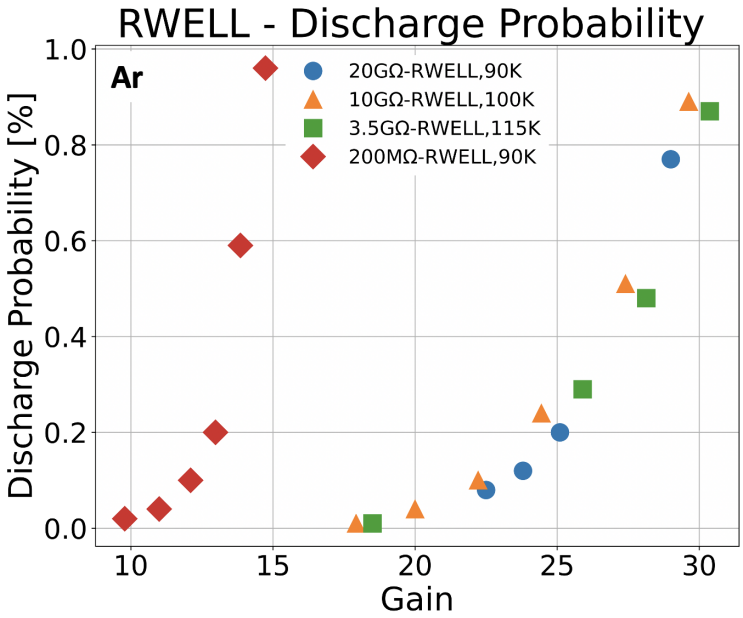

Figure 51: Discharge probability as a function of the RWELL gain for four different configurations: 200MΩ/□ at 90 K and 20 GΩ/□ at 90 K, 10 GΩ/□ at 100 K, 3.5 GΩ/□ at 115 K. Irradiation done with 4 MeV alpha particles, pressure: 1.2 bar.

Note the fast rise in discharge probability with the lowest resistivity RWELL, while the other three behave similarly. This is related to the fact that, for a higher R_S, the charge evacuation process is slower and consequently, the effective electric field at the bottom of the hole is reduced during the development of the avalanche, leading to quenching. In all cases, at maximal gain values, the discharge probability reaches ∼1%, with consequent interruption of the operation.

For all the investigated RPWELLs, the discharge probability is depicted in Fig. 52 as a function of ΔV_{RPWELL}.

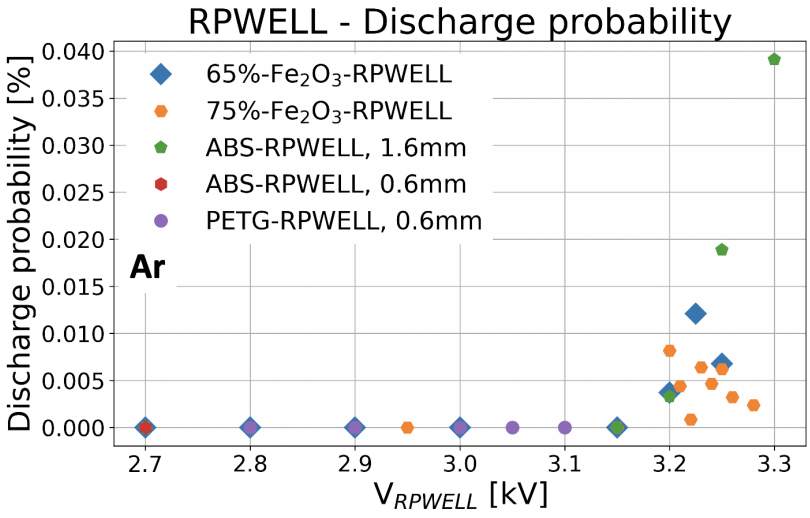

Figure 52: Discharge probability as a function of ΔV_{RPWELL} for all the RPWELL investigated configurations.

One observes that in the stable region, of 2.7 kV < $\Delta V_{RPWELL} \leq$ 3.15 kV, he detectors with the different plates are discharge-free. A phase transition occurs around $\Delta V_{RPWELL} \geq$ 3.15 kV, where a region of instability begins in all cases. Discharges occurred but at a low probability. These discharges were observed only for the thicker plates, e.g. 1.6 mm, and their nature is still unclear. The detector's stability was affected but the detector was able to recover and continue its operation.

Summary This study, developed in collaboration with USTC and USDC, encompassed the development of new materials for liquid argon detectors: DLC coatings and ceramic resistive plates (YSZ/Fe_2O_3). The DLC samples and the ceramic plates were characterized down to 77K and their electric properties were explored. In addition, the characterization of CNT-doped 3D-printed plates (ABS, PETG) was carried out.

With DLC layers of 200 MΩ/□ and of 20 GΩ/□, cryogenic RWELLs were assembled and operated for the first time in purified gaseous argon at 90K, 1.2 bar under collimated and attenuated alpha particle irradiation. This choice resulted in a number of electrons/hole compatible with the one generated by a μ track in LAr and permitted to avoid all the electron extraction-related issues. Cryogenic RPWELLs based on YSZ+Fe_2O_3 ceramic plates (with Fe_2O_3 in the concentration of 65% and of 75%) and on CNT-doped thermoplastic materials (ABS, PETG) were built and operated in the same experimental conditions. A comparison with a THWELL and with a THGEM + 2mm induction gap was carried out; it proved the superiority of the resistive detectors in terms of stability and gain. A summary of the detectors' performances is displayed in Table 8. The data are structured in terms

of the maximal reachable voltage at stable detector operation V_{Max}, maximal achievable stable gain G_{Max}, discharge probability at the maximal achievable stable gain $P_d|_{G_{Max}}$ and quenching factor, the latter being the coefficient of discharge charge reduction (measured on the power supply) compared to the THGEM's discharge charge.

Detector	**V_{Max} [kV]**	**G_{Max}**	**$P_d|_{G_{Max}}$**	**Quenching factor**
75%Fe_2O_3-RPWELL	3.15	16	0	~2.85 for $V_{RPWELL} > V_{Max}$
65%Fe_2O_3-RPWELL	3.15	12	0	~3.6 for $V_{RPWELL} > V_{Max}$
ABS-RPWELL, 1.6mm	3.15	11	0	~3 for $V_{RPWELL} > V_{Max}$
ABS-RPWELL, 0.6mm	3.1	14	0	N/A
PETG-RPWELL, 0.6mm	3.1	11	0	N/A
20GΩ-RWELL	3.175	30	0.9%	~15
200MΩ-RWELL	3.025	15	0.98%	~15
THWELL	2.9	8	0	N/A
THGEM	3.2	6	0	N/A

Table 8: Comparison of the performances of several WELL-based detectors and of a THGEM in Ar at 90 K, 1.2 Bar. Results for the RWELLs, RPWELLs, THWELL and THGEM were taken from Fig. 50

.

It was found that all the resistive detectors outperform the non-resistive ones, i.e. the THGEM and the THWELL. Among them, the 20 GΩ-RWELL was the detector with the best performance in terms of maximal achievable stable gain. Discharges in RPWELLs had a magnitude ~ 3-fold smaller than the one recorded for a THWELL ($\geq 3.75\ \mu$C) but they inhibited the detector for ≈30 minutes at the appearance of a discharge. From the reconstruction of discharge probability as a function of ΔV_{RPWELL} (Fig. 52), it was possible to notice the presence of a "phase transition", from a region where the discharge removal was complete to a region where the detector was affected by the presence of discharges. The nature of such discharges is still under investigation: the complete randomness displayed by the discharge probability for $\Delta V_{RPWELL} \geq 3.15$ kV and the presence of a small discharge quenching may point towards a partial breakdown mechanism. CNT-doped 3D-printed materials proved to be an alternative to ceramic tiles and had the advantage of having an almost temperature-independent R_V. However, it is known that these materials present problems of outgassing and aging [132]. It was observed that after a cryogenic cycle, these materials became more brittle and that discharges were able to cause local abrasions to the material surface.

In conclusion, in a small 3x3 cm^2 prototype, the RWELL detector was able to operate at 90K, 1.2 Bar up to a stable gain of ≈18 without discharges and up to ≈30 with 1% discharge probability. In discharge-free mode, the RWELL performed better than the RPWELLs,

THWELL and THGEM. In the direction of a scaled-up prototype, the main challenge that has to be faced from a technological perspective is the production of uniform, large-area resistive anodes: so far, it was possible to sputter with DLC surfaces of 20×100 cm^2 [133] while only 2x2 cm^2 Fe_2O_3+YSZ defect-free ceramic tiles were realized. It follows that a scaled-up version of the RWELL can be more easily envisioned.

7.2.3 Discharge quenching with the cryogenic RWELL

In this section, the nature of the discharges occurring in RWELL detectors will be detailed.

Isobaric warming-up - R_S scan The DLC layers' surface resistivity R_S depends on temperature, as it was detailed in Sec. 7.2.1. In order to study the resistivity-dependent detector response to discharges, the pressure inside the cryostat was kept fixed at 1.2 bar. The cooling was interrupted and the system was allowed to warm up to room temperature. This transient was very slow, ~10 hours. The detector was operated in discharge-mode and currents through the electrodes were monitored. By fixing the pressure at 1.2 bar (equal to the saturation pressure at 90 K, P_{sat}^{90K}, the problem's complexity was reduced by one degree of freedom: the discharge currents I_{disch} recorded by the current monitor depended on the applied voltage in the proximity of breakdown V_{BD}, and by R_S. V_{BD} also depends on T via the gas density. It reads:

$$I_{disch} \sim f(V_{BD}(\rho_{gas}(T), R_S(T)))|_{P_{sat}^{90K}} \tag{7.11}$$

In this way, the quenching properties were explored.

In order to cover a large range of R_S, two experiments were carried out making use of resistive layers specified in Table 9:

DLC layer	R_S^{DLC} at 298 K	R_S^{DLC} at 90 K
Sample 1	~ 1 MΩ/□	~ 200 MΩ/□
Sample 2	~ 40MΩ/□	~ 200GΩ/□

Table 9: Surface resistivity at 298 K and at 90 K for two different DLC samples.

At 90 K, the first develops a R_S ~ 200 MΩ-RWELL and the second ~ 200 GΩ-RWELL . In Fig. 53 the discharge currents as a function of V_{BD} and T recorded during the isobaric warming-up from the RWELL top, from the resistive layer, and from the anode are reported for the two experiments.

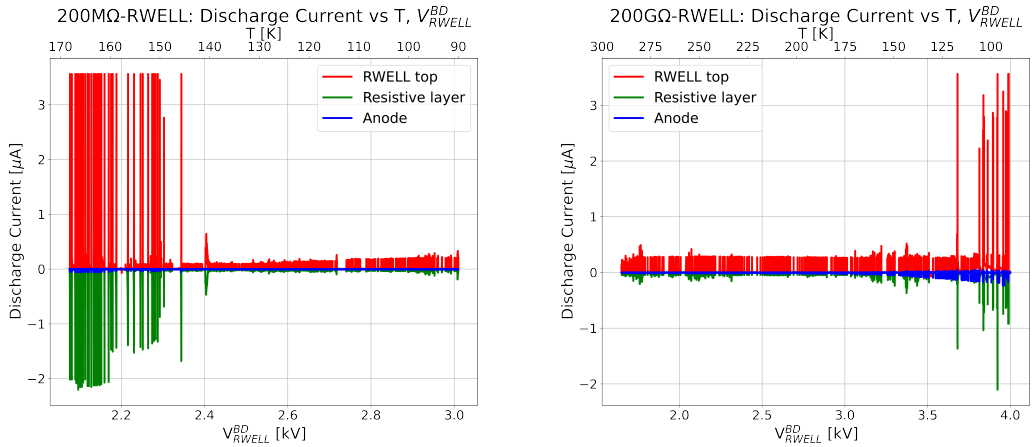

Figure 53: Discharge currents from RWELL top (red), resistive layer (green) and anode (blue) vs V_{BD}, T at P = 1.2 Bar for **Left** a 200 MΩ/□-RWELL detector; **Right** a 200 GΩ/□-RWELL detector.

In Fig. 53, left, it is possible to see that the 200 MΩ-RWELL was operated from 90 K to 150 K under the presence of discharges. The magnitude of these discharges, I_{disch} ≈0.25 μA, at 90 K is reduced by a factor ≥15 compared to a non-quenched event occurring in the same condition. At 170 K, with R_S ≈5M Ω/□, the detector is not able to quench anymore. A disruptive event occurring in this condition is visible as a spike able to saturate completely the current monitor dynamics, read I_{disch} ≈3.75 μA. During this transient, also the voltage applied to the RWELL in the proximity of breakdown changed from V_{BD} = 3.01 kV at 90 K to V_{BD} = 2.08 kV at 170 K. In Fig. 53 right, the 200GΩ-RWELL was operated from 90 K, R_S = 200 GΩ/□ to 298 K, R_S = 40 GΩ/□. The detector was operated in discharge mode. At 90 K, the detector was not able to operate properly because of the presence of constant currents flooding the electrodes. Above 110 K to room temperature, the presence of quenched discharges was observed. The voltage applied to the RWELL in the proximity of breakdown changed from V_{BD} = 4.01 kV at 90 K to V_{BD} = 1.65 kV at 298 K.

In Fig. 54, the discharge current as a function of R_S is shown - this result was obtained by combining the trends shown in Fig. 53 with the R-T scans. The x-axis for R_S is shown in logaritmic scale.

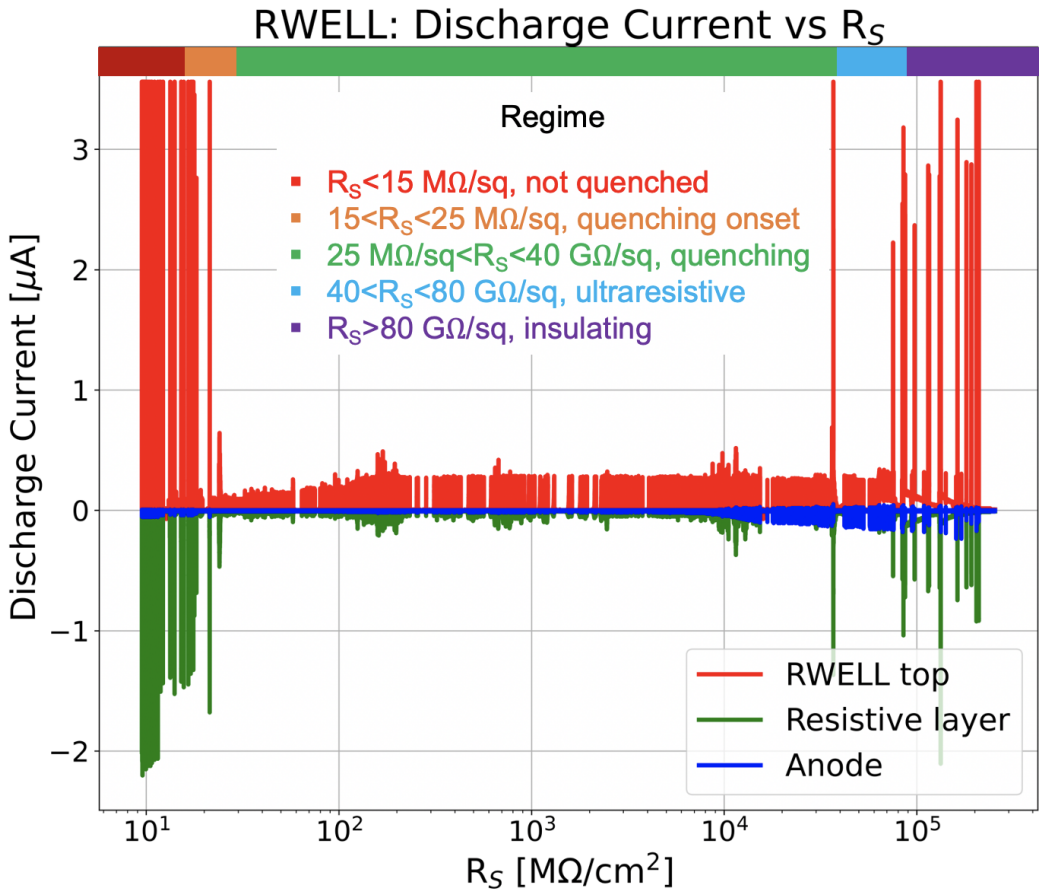

Figure 54: Discharge current from RWELL top (red), resistive layer (green) and anode (blue) vs surface resistivity.

From Fig. 54, it is possible to observe the presence of five distinct behaviors of the discharge current according to the value of R_S, as highlighted by the color bar above the plot:

- for R_S < 15 MΩ/□, discharges are not quenched and induce a full detector tripping;
- for 15 Ω/□ < R_S < 25 MΩ/□, the co-presence of non-quenched and quenched discharges is observe. This region sets the onset of discharge quenching;
- for 25 MΩ/□ < R_S < 40GΩ/□, discharges are quenched;
- for 40 GΩ/□ < R_S < 80 GΩ/□, the DLC is ultra resistive: induced discharges start appearing from the anode;
- for R_S > 80 GΩ/□, the DLC behaves like an insulator, preventing current evacuation: the presence of constant currents, ≈0.1 μA, from the RWELL top is recorded and not-fully quenched discharges can be observed; the latter often results out of a discharge pile-up process. The detector in this regime was not operable.

From Fig. 54, for 25 MΩ/□ < R_S < 150 MΩ/□, a linear trend in the discharge current is visible while for 150 MΩ/□ < R_S < 40 GΩ/□, the trend is flat. The origin of this phenomenon has not been clarified yet.

In Fig. 55, single discharge current pulses are shown for different values of R_S.

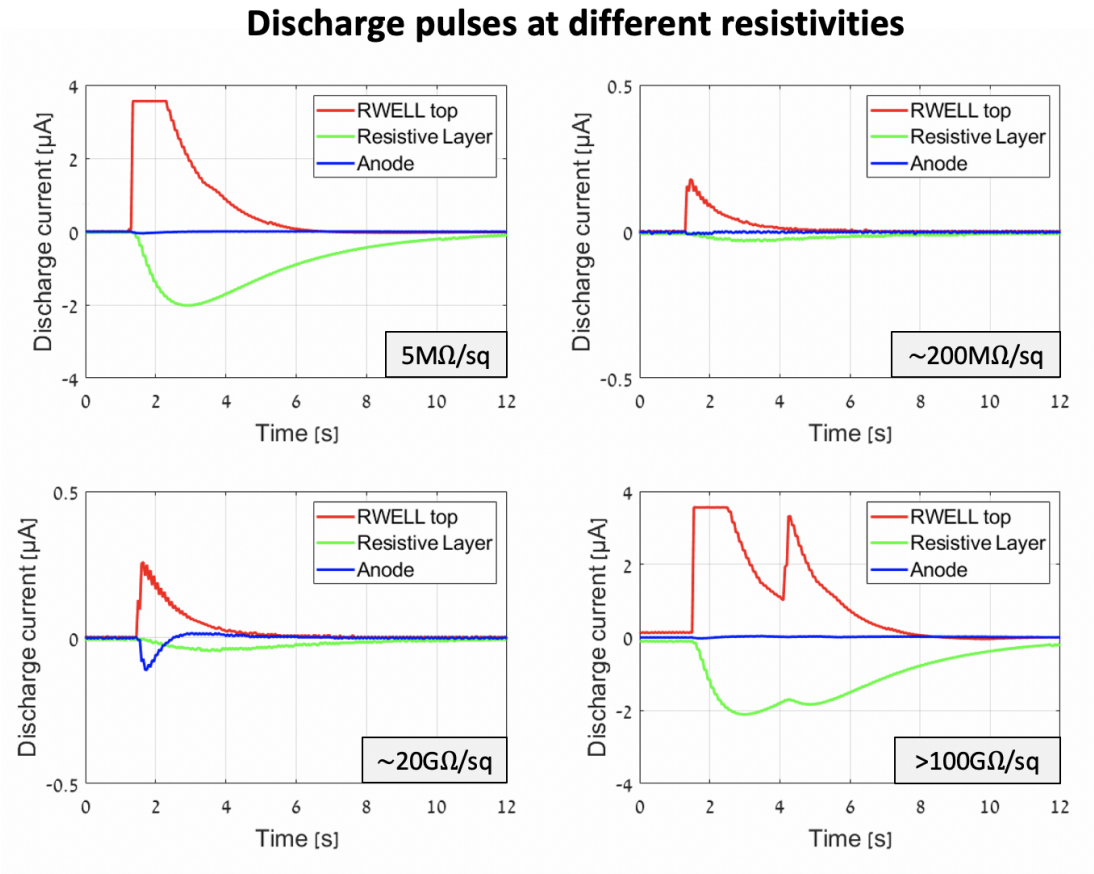

Figure 55: RWELL discharge current pulses recorded from RWELL top (red), resistive layer (green) and anode (blue) for **(Top left)** R_S = 5MΩ/□, non-quenching regime, **(Top right)** R_S ~200 Ω/□, quenching regime, **(Bottom left)** R_S ~20 GΩ/□, ultra resistive quenching regime, **(Bottom right)** R_S > 100 GΩ/□, insulating regime.

In Fig. 55, top left, an example of non-quenched discharge is shown for R_S = 5MΩ/□; in Fig. 55, top right, an example of quenched discharge is shown for R_S ~200 MΩ/□; in Fig. 55, bottom left, an example of quenched discharge is shown for R_S ~20 GΩ/□ (ultra resistive), the presence a discharge signal from the anode is visible in blue; in Fig. 55, bottom right, an example of piled-up discharge is shown for R_S > 100 GΩ/□, insulating regime.

In order to compute the discharge charge, an algorithm was implemented to integrate the currents recorded from the power supply: the discharge current peaks as a function of time were identified, "peak(t)", and a variable integration window for each discharge was defined, "w(peak)", by taking the half-distance between the reference distance and its previous and following discharge. The first and last discharges were treated with an arbitrary integration window. This reads:

$$w(peak) = \frac{|t(peak-1) - t(peak|)}{2} + \frac{|t(peak+1) - t(peak)|}{2} \tag{7.12}$$

The numerical integration was then performed after baseline removal:

$$Q(peak) = I_{\text{Disch}}(t) * w(peak) \tag{7.13}$$

In Fig. 56, the discharge charge of the 200MΩ-RWELL at 90 K is shown as a function of T and V_{BD}. Two distinct populations are visible. Both were fitted using linear regressions, with a coefficient C equal to 0.24 and 0.46, respectively. The population associated with C = 0.46 corresponds to double discharges.

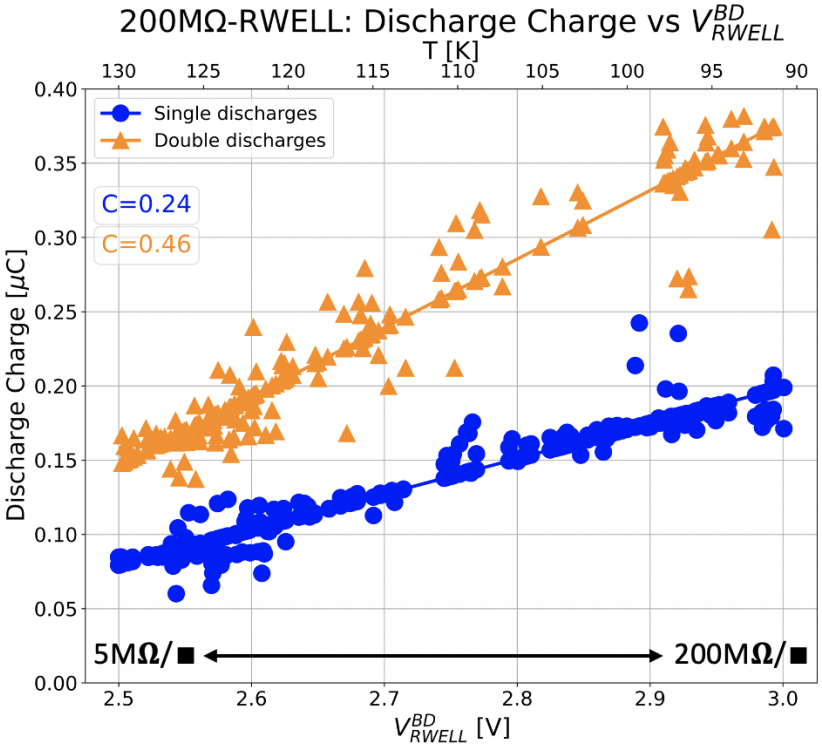

Figure 56: Discharge charge as a function of T, V_{BD} for a 200 MΩ-RWELL at 90 K.

In Fig. 57, the discharge charge of the 200GΩ-RWELL at 90 K is shown as a function of T and V_{BD}. Three distinct populations are visible. The trends are composed of a linear part (40 < R_S < 110 MΩ/□) followed by a flat one (110 MΩ/□ < R_S < 80 GΩ/□). The linear

trends were fitted using linear regressions, with a coefficient C equal to 1.68, 3.37, and 5.2, respectively. The population associated with C = 3.37 corresponds to double discharges, and the one with C = 5.2, to triple discharges.

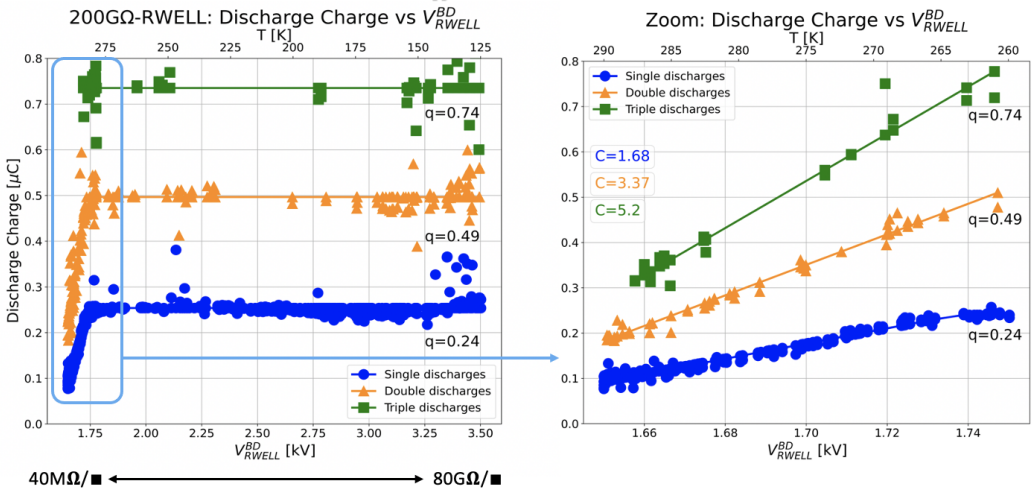

Figure 57: **Left)**: Discharge charge as a function of T, V_{BD} for the 200GΩ-RWELL at 90 K. The plot shows up to R_S ~ to 80 GΩ; **Right)**: Linear trend of the discharge charge as a function of T (zoom of the window shown in the left figure), V_{BD} for a 200GΩ-RWELL at 90 K (40 < R_S < 110 MΩ/□).

For the flat behavior of the discharge charge an exhaustive explanation is currently missing: is it a feature of the discharge quenching with resistive layers with R_S > 40 MΩ/□ or a current-monitor limitation? In order to answer these questions, a TPB-coated PMT was added to the system to record discharge light. The investigation is currently ongoing.

7.2.4 Simulations

In order to validate the experimental results shown in Fig. 50 on the results with LEMs present in literature, a set of simulations was implemented via Garfield++ [134, 135]. The effective gain measured using a 0.8 mm THGEM in the present work, G = 6, has been found to be lower compared to that reported in [136], Fig. 3.17, for a LEM of the same dimension operated at 87 K and 0.98 bar, G = 20 (stabilized).

Methodology The number of primary ionization produced along the 4 MeV alpha track in gaseous argon was computed using SRIM [119, 137] and found to be about 10^5 electrons (note for comparison: a μ track in LAr gives ≈5000/mm). The drift field map, computed in COMSOL Multiphysics® [138] and the primary ionization data from SRIM, were imported in Garfield++. The electron transport data for gaseous argon at 90 K, 1.2 bar were supplied via supplied by Magboltz [139], and this allowed for the computation of charge multiplication for any given voltage configuration. The *AvalancheMicroscopic()* routine

of Garfield++ was used to model the avalanche formation by performing a collision-to-collision tracking of electrons. For any electron starting at the drift region and getting multiplied inside the THGEM holes, the avalanche size is not expected to have any significant dependence on the distance of its starting point from the THGEM electrode. Primary electrons were grouped in several clusters, of 2000 electrons/cluster. The avalanche size for a single electron starting from the position of a given cluster was calculated and weighted by the number of electrons in that cluster. The contributions from all the clusters were summed up to find the total charge produced by all the primary electrons. The gas gain was calculated by dividing the total produced charge by the primary charge produced by the alpha track. This was repeated for several alpha tracks, and the mean of the gain distribution was compared with the data. To use the computational resources economically, the simulation was performed to find the total charge multiplication inside the gas volume, whereas the measured gain values are found from the charge induced on the readout anode. This is expected to give rise to a difference between the two. Differences in gas purity and in the spatial distribution of the primary charge were not accounted for.

Results In Fig. 58 left, the preliminary simulated gain curves for our case and the 0.8 mm thick LEM in reference [136] are displayed as a function of voltages across the THGEM. The corresponding measured curves are also shown.

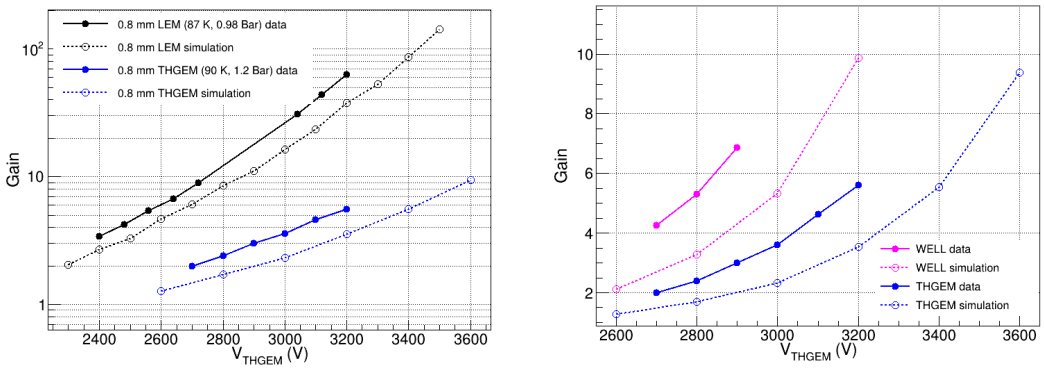

Figure 58: **Left:** Comparison of the simulated gain curves with the present measurements on a THGEM at 90 K, 1.2 bar and the measurements on a 0.8 mm thick LEM at 87 K, 0.98 bar, as reported in Fig. 3.15 in reference [136], **Right:** Comparison of simulated and measured gain curves in WELL and THGEM at 90 K, 1.2 bar.

The trend of the simulated curves follows the data points closely and establishes the different operating conditions (temperature and pressure) as the cause for the lower gain measured at 90K, 1.2 bar. The same computational methods were used to understand the difference in gain values from a THGEM and a THWELL (Fig. 50). The simulated gain curves and the data points for the two configurations are shown in Fig. 58 right. This difference can be attributed to the different values of the electric field inside the THGEM holes in these two configurations for any given voltage difference across the THGEM.

8 Summary: Discussion and Outlook

The aim of this PhD work was to develop new light and charge readout concepts for DP LAr-TPCs. This generic research was directed towards three different detector concepts: the bubble-assisted LHM detector for light readout and the cryogenic RWELL and RPWELL for charge readout. Being another milestone in detector physics, this work brought new insights and a deeper understanding of the field of cryogenic noble-liquid detectors.

8.1 LHM

The bubble-assisted LHM detector, originally conceived as a readout for the combined detection of ionization charge and scintillation light in LXe [73], was demonstrated in LAr [82] and the mechanism governing the detector performance (bubble electrodynamics) was investigated [85]. The results discussed in 7.1 covered a characterization of the LHM detector based on a THGEM and proved the detector's imaging capabilities with SiPMs. For the same electrode, the LAr-LHM's performance (energy resolution and imaging) was poorer than the LXe-LHM's one. It was suspected that this is caused, on one hand, by the lower electroluminescence-photon yield of LAr, and, on the other hand, by the inefficient transfer of ionization electrons and photoelectrons through the interface from liquid-into-gas. The loss of electrons, reflected in a relatively low-energy resolution and low photodetection efficiency (PDE) in LXe-LHM [83], could have resulted from the interface shape. Subsequently, the LHM's bubble electrodynamics was addressed and the work consisted of four main parts: a theoretical description of the bubble equilibrium configurations, characterization of the materials composing the LHM's assembly, numerical simulations of the bubble electrodynamics in LAr and in H_2O and silicon oil (to permit voltage application across the electrode) at RT, μ-CT experiments to validate the simulations in H_2O and silicon oil at RT. It was found that the presence of electric fields had a non-negligible effect on the bubble equilibrium configuration and on the final detector photoemissivity, effectively acting as an additional pressure. However, the electron transfer efficiency through the bubble interface was not addressed in this work.
In conclusion, to make the concept available for LXe-based DP detectors, a serious improvement of the PDE value (e.g. >15%) would allow designing large-volume local-DP LHM-based TPCs [140], e.g. for future dark-matter searches [31]. This requires advanced R&D to solve the problem of the electron transfer through the bubble interface. LAr-LHM, being more recent, still requires basic R&D, among the others the measurement of the quantum efficiency of CsI in LAr at 125 nm for the estimation of the detector PDE.

8.2 RWELL & RPWELL

For the first time, two novel charge-readout concepts the "cryogenic RWELL" and "cryogenic RPWELL" were investigated in an attempt to increase the detector gain by discharge quenching. They are based on resistive materials respectively in the shape of thin layers

(DLC) and thick plates (made of Fe_2O_2-YSZ ceramics or of CNT-doped thermoplastics) and were operated at cryogenic temperature (90 K, 1.2 bar) in argon vapor. It was found that these resistive multipliers perform better than their non-protected counterparts (THGEM, THWELL) in the same experimental conditions in terms of gain and stability. The 20GΩ-RWELL was able to operate up to a stable gain G = 18 in discharge-free mode and up to G = 30 with 1% discharge probability in quenched-discharge mode while the 75Fe_2O_3-RPWELL (8×10^{10}Ω·cm) reached a stable gain of 16 in discharge-free mode. The 20GΩ-RWELL gain was a factor 3.75 higher than the gain obtained with a THWELL, G = 8 (no discharges), and a factor 5 better than the one with a THGEM, G = 6 (no discharges). During the RWELL operation, quenched discharges were recorded and their nature was investigated, outlining the role played by the surface resistivity R_S in the discharge quenching process (isobaric R-T scans). Five regimes of RWELL operation were identified according to the value of surface resistivity: no quenching (R_S < 15 MΩ/cm^2), quenching onset (15 < R_S < 25 MΩ/cm^2), quenching (25 MΩ/cm^2 < R_S < 40 GΩ/cm^2), ultraresistive (40 GΩ/cm^2 < R_S < 80 GΩ/cm^2) and insulating (R_S > 80 GΩ/cm^2). It was observed that the shape and intensity of the discharges vary according to the discharge regime of operation. A linear trend followed by a flat trend of the discharge charge as a function of R_S was observed in the quenching regime. In the ultraresistive and insulating regimes, induced-discharges started being visible also from the anode. In the case of RPWELLs, no discharges were recorded (P_d = 0) in the same operational voltage range. Beyond this range, slightly quenched discharges able to destabilize the detector started appearing. The RPWELL discharge probability showed a phase transition around V_{RPWELL} = 3.15 kV. The nature of these discharges is not clear and it is still under investigation.

In conclusion, the results presented in 7.2.2 establish some superiority of resistive-multiplier readout elements vs non-resistive ones. The results of these studies, and further ones, may pave the way for a regain of interest in charge-readout of DP LAr-TPCs. Higher stable gain, compared to the one currently reachable with LEM detectors, could make an impact on future neutrino experiments. In fact, the higher charge gain could help overcome the charge attenuation over large-drift paths and allow for the detection of lower-energy particles, e.g., supernovae neutrinos.

As part of the current R&D, the optical properties of quenched discharges (avalanche-induced EL) are being investigated using a TPB-coated PMT coupled with a cryogenic RWELL. An agreement between charge and light readout could shed light on the, yet unclear, observed flat trend in Fig. 54. A future direction of investigation could also encompass the realization of the so-called "all-in-one" ceramic RPWELL, see Fig. 59: it is composed of a semi-perforated resistive ceramic plate whose electrodes can be realized via chromium evaporation and the holes via laser-drilling [141].

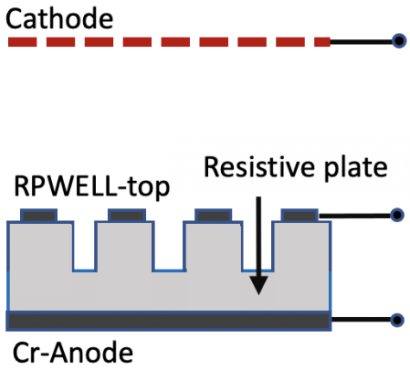

Figure 59: Scheme of a all-in-one ceramic RPWELL detector.

The idea that led to the formulation of this concept lies in the possibility of having an amplification element directly embedded in the quenching structure of the resistive plate. Foreseen advantages of such a readout are the absence of charging-up, due to the fact that its holes are made of resistive material, and its intrinsic easy-scalability, since no gluing process is needed. On the other hand, as reported in Fig. 35, R_v at cryogenic temperature depends on the applied voltage: this requires fabricating ceramic plates with a Fe_2O_3 concentration of ~30% (the latter being brittle) in order to operate the detector at $\Delta V_{\mathrm{RPWELL}}$ ≈3kV with $10^9\Omega\cdot$cm < R_v < $10^{12}\Omega\cdot$cm. Efforts in this direction are ongoing.

This PhD work made novel light and charge readout concepts available for LAr-TPCs. Conclusions regarding applicability require further studies.

9 Additional Results

9.1 Bubble-assisted LXe-LHM

This work was developed during the first year of the Ph.D. in collaboration with Dr. Eran Erdal.

Summary A study of the bubble-assisted LHM in liquid xenon was carried out in Mini Xenon apparatus (Minix) [81] and it consisted of:

- a comparison between four different types of LHM electrodes: THGEM, standard double-conical GEM, 50 μm-thick single-conical GEM and 125 μm-thick single-conical GEM;
- demonstration of major amplification of the EL light yield by setting a strong transfer field across the bubble;
- Imaging results using SiPMs.

It was demonstrated that the electrode geometry plays a crucial role in determining the effective EL yield (number of EL photons emitted over 4π per electron entering the electrode's hole), and the resulting energy resolution. Currently, the 125μm-thick SC-GEM (with 300 μm diameter upper holes) yielded the best results. Compared to the others, it shows more than 3-fold larger EL yield for both ionization electrons and VUV photons. The difference in the LHM-electrode's response to electrons is still a subject of extensive studies. One of the hypotheses recently raised focuses on the transfer of electrons through the liquid-to-gas interface. Subsequently, a demonstration of the promising imaging capabilities of the LHM detector (up to 200 μm resolution) was provided using a quad-SiPM.

The results were summarized in [77, 83].

9.2 Single-UV photon detection with RPWELL at RT

This work was developed during the first year of my PhD in collaboration with Dr. Purba Bhattacharya.

Summary In this work, we investigated single-electron spectra obtained with single-stage and double-stage RPWELL-based detectors. The goal was to evaluate the potential advantage of their operation in conditions yielding Polya-like single distributions; the latter result from charge-avalanche saturation in the RPWELL holes. The detectors' response was single-photoelectrons emitted from a CsI photocathode deposited on the multiplier's surface. Their performance was studied in various gas mixtures and electric-field settings.

The results of this study were reported in [142].

9.3 Novel Resistive-Plate WELL sampling element for (S)DHCAL

In 2018 I joined the SDHCAL project coordinated by my colleague Dr. Dan Shaked-Renous. During this activity, I took part in the large RPWELL (48×48 cm^2) fabrication at WIS and in their operation under 150 GeV muon and high rate 2-6 GeV pion beams at CERN/PS facility.

The first results of this experimental campaign were summarized in [143]. The data permitted validating a GEANT4 simulation framework of a DHCAL, and evaluating the expected pion energy resolution of a full-scale RPWELL-based calorimeter, as reported in [144].

10 Appendix

10.1 Hydrostatic model for the position of the interface in LHM

We assess the admissible positions of a bubble meniscus within the THGEM hole using some approximations and a graphical solution approach. We refer to the configurations shown schematically in Fig. 16. We identify univocally the menisci by the value of z_t of the center of the cap on the symmetry axis, where the origin of z is at the bottom face of the support. We assume that for every possible position, the meniscus is a spherical cap, attaching to the solid boundaries with the prescribed contact angle θ. In doing this we implicitly assume that the curvature $\kappa = 1/r$ of the meniscus is, for a given position, constant, and we neglect the hydrostatic pressure difference between the top and the contact line of the meniscus. In first approximation this difference is, in the relevant cases, of the order of or smaller than $(\rho_l - \rho_g)gR$, to be compared with $(\rho_l - \rho_g)gH$, and thus minor. Due to convenience, we solve Eq. **??** graphically by plotting separately $p_b = p_1 - p_2$ and p_L, see Fig. 61. The intersections between the two curves give the sought solutions. Both pressure terms can be expressed as functions of the top bubble height z_t. The pressure difference between the liquid at the top of the bubble and the gas inside is simply $p_b = (\rho_g - \rho_l)g(z_t + H)$; the term $p_L(z_t)$ has a more complex dependence as a function of its location and concavity imposed by the contact angle constraint. To model the latter, we distinguish the three cases:

1. Meniscus attached to the upper face: for $z_t > z_4 = h + \frac{1-\cos\theta}{\sin\theta}(R+s)$, the meniscus has a negative curvature $\kappa = \frac{\cos\theta - 1}{z_t - h}$. This corresponds to $p_L(z) = 2\gamma\frac{\cos\theta-1}{z_t-h}$, which is always directed downwards. Its lowest negative value is $p_L(z_4) = -2\gamma\frac{\sin\theta}{R+s}$.

2. Meniscus in the hole: at any height $z_2 = s + \frac{1-\sin\theta}{\cos\theta}R < z_t < z_3 = h - s + \frac{1-\sin\theta}{\cos\theta}R$ the meniscus attains a curvature $\kappa = -\frac{\cos\theta}{R}$, which accounts for $p_L = -2\gamma\frac{\cos\theta}{R}$, independent on z_t. This pressure is directed downwards for $\theta < 90°$ and upwards for $\theta > 90°$.

3. Meniscus attached to the lower face: for $z_t < z_1 = \frac{\cos\theta-1}{\sin\theta}(R+s) < 0$, the meniscus has positive curvature $\kappa = \frac{1-\cos\theta}{z_t}$, corresponding to an upward pressure $p_L(z_t) = 2\gamma\frac{\cos\theta-1}{z_t}$. The highest value of p_L in this branch is obtained by the smallest spherical cap which attaches out of the rounded edge, that is $p_L(z_1) = 2\gamma\frac{\sin\theta}{R+s}$.

The relevant relations are obtained considering the circular arcs in Fig. 60, which meet the solid wall with the prescribed angle θ. To account for the transitions between the cases, we assume that the edge of the hole is smooth and defined through a small radius of curvature $s \ll R$, see Fig. 60. The actual value of s and the more irregular shape of a real hole are out of scope to this discussion. The smoothness of the edge is further important because it allows the attachment of a hemispherical meniscus of radius $\simeq R$ on the top side for $\theta < 90°$ (bottom for $\theta > 90°$), which corresponds to the maximal attainable curvature

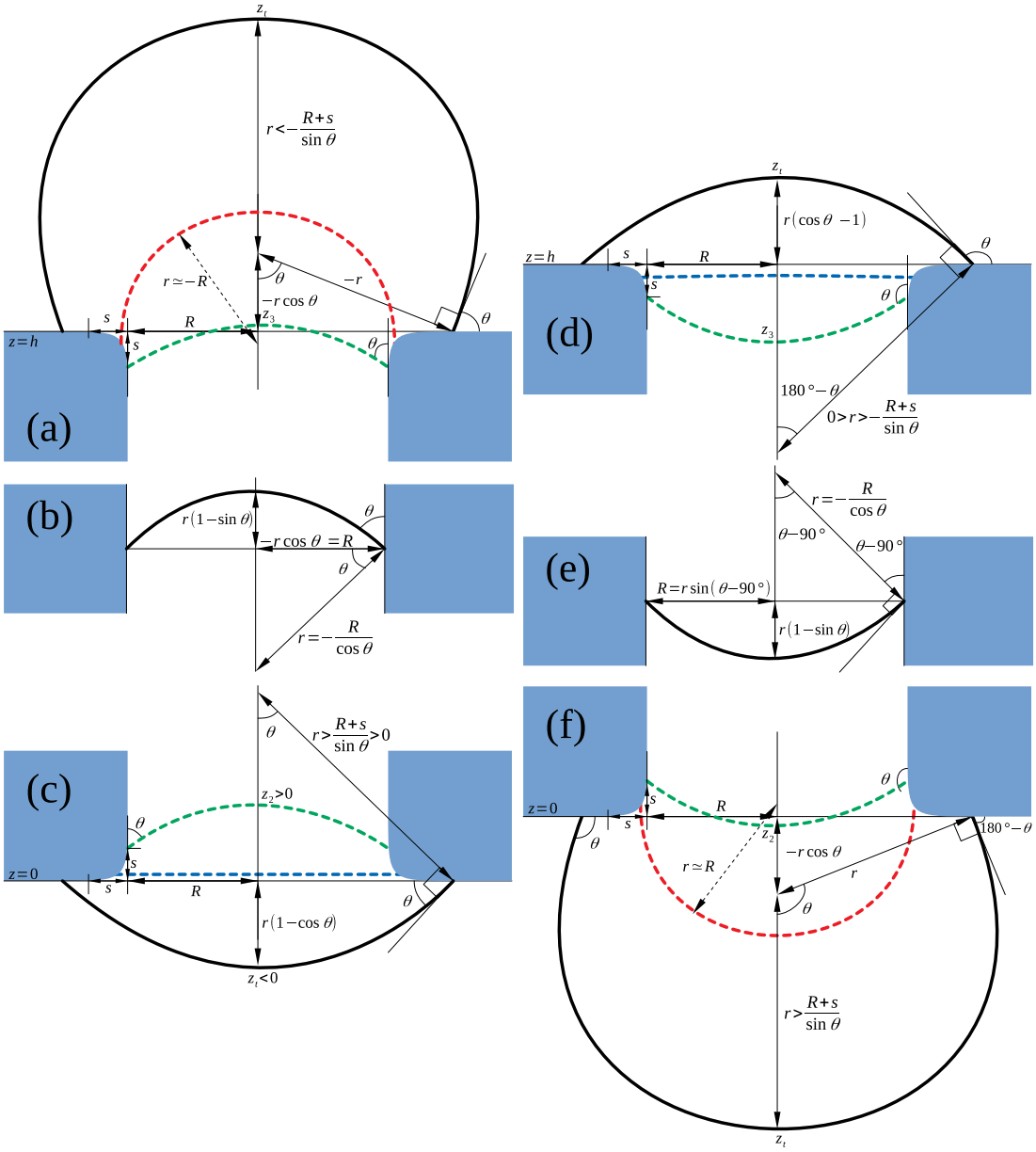

Figure 60: Geometrical relations for the relevant meniscus positions: a)...c) for $\theta < 90°$, d)...f) for $\theta > 90°$, at the top, middle and bottom of the hole respectively. The green lines depict the topmost and lowermost acceptable menisci attached to the hole; the red lines show the maximally curved menisci attached to the smoothed edge, and the blue lines are admissible flat menisci.

$\kappa = 1/R$, which is generally higher than the curvature in branch I (for $\theta < 90°$) or III (for $\theta > 90°$). This corresponds to a maximal containment pressure $p_L = -2\gamma/R$ in the first case (Fig. 60(a)), and to a maximal (unstable) contrasting pressure $p_L = 2\gamma/R$ in the other (Fig. 60(f)).

Summing up, a realization of the curves $p_L(z_t)$ and $p_b(z_t)$ is plotted in Fig. 61. The curves depend on all the parameters of the problem, and can accordingly intersect in 1 or 3 points, or even 5 for $\theta < 90°$. Moreover, an intersection corresponds to a stable equilibrium solution if $\frac{d(p_L - p_b)}{dz} < 0$, because a perturbation of the meniscus height z would translate in a resulting restoring pressure, whereas the solution is unstable for $\frac{d(p_L - p_b)}{dz} > 0$. The graphical solution sketched in Fig. 61 shows that stable solutions, if they exist, fall within the transition zones I–II and II–III. While their existence is granted, their location is entirely dependent on the details of the edge smoothing. We thus expect that they are poorly defined in a real device, where the edges of the drilled holes are unavoidably irregular and different one from the other.

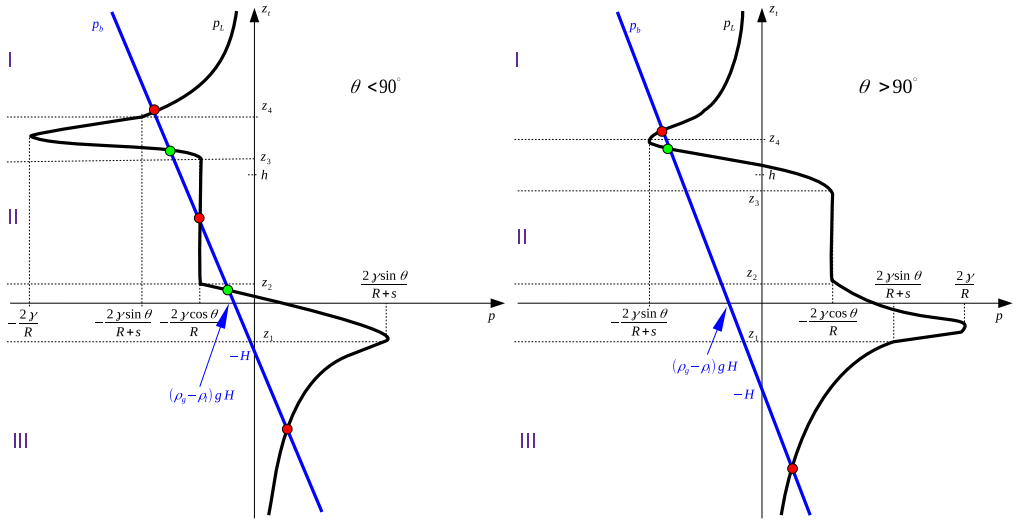

Figure 61: Sample graphical solutions for $\theta < 90°$ (left) and for $\theta > 90°$ (right). The solid black curve and the blue line represent $p_L(z_t)$ and $p_b(z_t)$ respectively. Green dots represent stable solutions and red dots unstable ones. An interactive version of this figure, which allows to vary all the problem parameters, is available online as GeoGebra activity file [145].

In the ideal smooth edge case, some analytical conditions for the existence of stable solutions could be derived, but would lead to a complex set of inequalities, involving all the parameters of the problem and a transcendental dependence on θ. We do not list here the expressions for all possible cases. As an example, however, for $\theta < 90°$ the condition for a stable meniscus pinned at the bottom side can be written as

$$(\rho_g - \rho_l) g (z_2 + H) > -2\gamma \frac{\cos\theta}{R}, \tag{10.1}$$

which translates into a condition for the bubble thickness H:

$$0 < H < 2\gamma \frac{\cos\theta}{R(\rho_l - \rho_g)g} - s - \frac{1-\sin\theta}{\cos\theta} R \tag{10.2}$$

By the same token, a stable meniscus pinned at the top side would exist, for $\theta < 90°$, if

$$(\rho_g - \rho_l)(z_3 + H)g < -2\gamma \frac{\cos\theta}{R} \tag{10.3}$$

and

$$(\rho_g - \rho_l)(z_4 + H)g > -2\frac{\gamma}{R} \tag{10.4}$$

i.e.

$$2\frac{\gamma\cos\theta}{R(\rho_l - \rho_g)g} - h + s - \frac{1-\sin\theta}{\cos\theta} R < H < 2\frac{\gamma}{R(\rho_l - \rho_g)g} - h - \frac{1-\cos\theta}{\sin\theta}(R+s) \tag{10.5}$$

Using the material parameters of argon in the experimental conditions ($\gamma = 11.83\,\mathrm{mN/m}$, $\rho_l - \rho_g = 1393\,\mathrm{kg/m^3}$), $\theta = 48°$ as measured for Ar/FR4, and the typical dimensions of THGEM ($R = 150\,\mu\mathrm{m}$, $h = 400\,\mu\mathrm{m}$, $s \to 0$) the first condition (Eq.10.2) evaluates to $0\,\mathrm{mm} < H < 7.7\,\mathrm{mm}$, and the second (Eq.10.5) to $7.3\,\mathrm{mm} < H < 11.1\,\mathrm{mm}$.

10.2 Methodology of the simulations

Simulations were performed using the microfluidics module of the commercial package COMSOL™(v. 5.4). To solve the two-phase flow problem, the Arbitrary Lagrangian-Eulerian grid (ALE) method was adopted. In this framework the computation is done in terms of Eulerian variables defined on a mesh whose deformation was somewhat arbitrary, while preserving faithfully the moving interface between the fluid and the gas domain. This is a sharp interface method; it was found that the other methods provided by COMSOL for two phase flow which make use diffuse interfaces, i.e. Level-Set or Phase-Field, suffer from known drawbacks which degrade the solution quality for the purposes of our investigation. Notably, diffuse interface methods are affected by spurious currents, which hinder the computation of quasi-static, capillarity-dominated flows, and require a high resolution in order to resolve fluid interfaces, which translates in prohibitive computational times. In contrast, ALE cannot not cope with large domain deformations, nor with domain topology changes, such as those taking place for systems of coalescing or bursting bubbles. Therefore we limited this investigation to the relaxation of the bubble meniscus in vicinity of the THGEM hole, which generally entailed small displacements. For computational efficiency, a single bore THGEM was simulated using a 2D axysimmetric minimal domain, as depicted in Fig. 62. The coupled system of the Laplace equation for the electric potential V and the Navier-Stokes equation for fluid velocity $\vec{u}$ and pressure p was solved. The material properties of argon at the operating conditions of Sec. 7.1 were used. For the fluid part, open flow pressure boundary conditions were assigned to the top and bottom boundaries. A prescribed static angle of 48°, corresponding to the value measured on FR4,

was assigned to the meniscus contact on the hole wall. For the electrostatic part, boundary conditions were assigned in order to emulate typical fields employed in THGEM detectors. Potentials were assigned at the top boundary, at the faces of the upper and lower electrode, and at the bottom boundary. The main control parameter was the voltage difference V_0 between the upper and the lower electrode. The top and bottom boundary potentials were assigned relatively to them, so that the mean electric field was 100 V/cm above the THGEM and 250 V/cm below it. These are typical values for the fields used in detectors, which drive the migration of electrons produced above the THGEM, and their actual value was of little importance in the present study. The electric force (7.1) on the interface between gas and liquid was implemented, in COMSOL parlancy, as a weak contribution on the fluid-fluid boundary, using test functions. The focus of this investigation is the effect of the electric field on the meniscus position, and hence the schematic boundary conditions imposed on the reduced domain may be somewhat inadequate for a real detector with a 3D structure. Complete simulations with the full geometry may eventually be done in the future; the setup of fields used here allows us already to shed light on the basic electro-hydrodynamics.

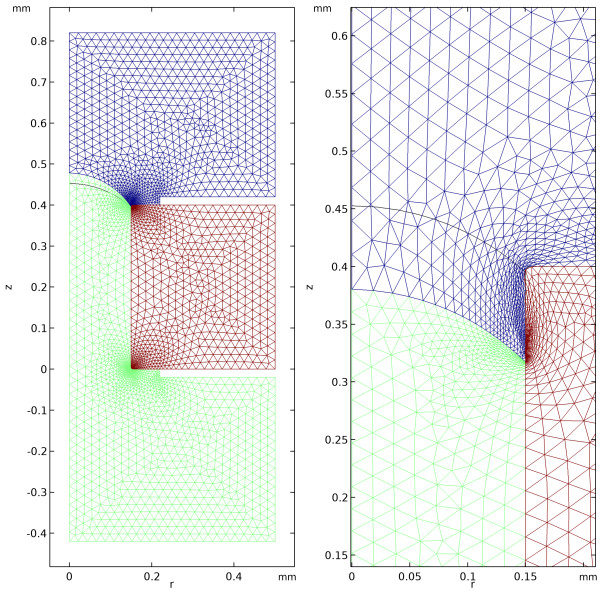

Figure 62: Computational mesh for the case of meniscus at the top of the hole. Edges in blue, green and red refer to the liquid, gas and FR4 domain respectively. The black line is the initial meniscus position, in this case chosen arbitrarily as the topmost meniscus in the hole with contact angle θ, corresponding to the hydrostatic solution for $H = 7.7$ mm. The plot on the left shows the mesh at the final time, for $H = 10$ mm and $V = 1200$ V. The plot on the right shows a zoom of the deformed mesh for the non-converging simulation with $H = 10$ mm and $V = 2800$ V.

Since the sought equilibrium is unknown, the simulations were primed with the interface initially close to the expected equilibrium position, and the system was allowed to evolve dynamically. Control parameters of the simulation include the electrode voltages, the boundary pressures (equivalent to the bubble height H) and the contact angle θ. The

system was then integrated till $t = 100\,\text{ms}$ physical time. This simulation protocol was applied to bubble menisci placed either by the upper or by the lower face of the THGEM. This procedure was empirically seen as viable to let the system relax to the equilibrium, after a few damped meniscus oscillations. The lack of relaxation of the meniscus within this time (usually accompanied by an early numerical divergence, or by nonphysical results) was interpreted as an absence of a stable equilibrium for the meniscus for the probed parameter values. Fig. 62 exemplifies the well-behaved computational mesh produced at final time by a converging simulation, vs. the much too deformed mesh attained at an early time by a non-converging case, in which the meniscus is pushed downwards instead of settling at the top of the hole. This classification is certainly empirical, of relative value, and somehow dependent on the actual initial condition chosen, but it is still a criterion. Repeating the procedure for different values of the control parameters it was possible to discriminate intervals of existence of the equilibrium like shown in Fig. 63 for varying H and V_0.

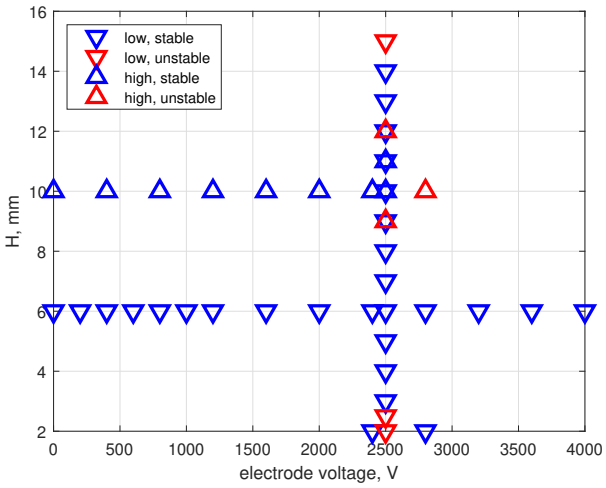

Figure 63: Simulations converging to a stable equilibrium point or not converging, for various values of the bubble depth H and the potential V_0 on the electrodes. Upwards-pointing triangles refer to simulations with the meniscus pinned at the top of the hole, and downwards-pointing triangles at the bottom.

10.3 Additional results for the cryogenic RPWELL

A compilation of results for the gain stabilizations of the RPWELLs is here reported.

65%Fe_2O_3-RPWELL In Fig. 64 top, the gain stabilization curve for the 65% Fe_2O_3-RPWELL is presented and in Fig. 64 bottom, the discharge currents registered from the power supply from the RPWELL top and anode are reported in time-correlation.

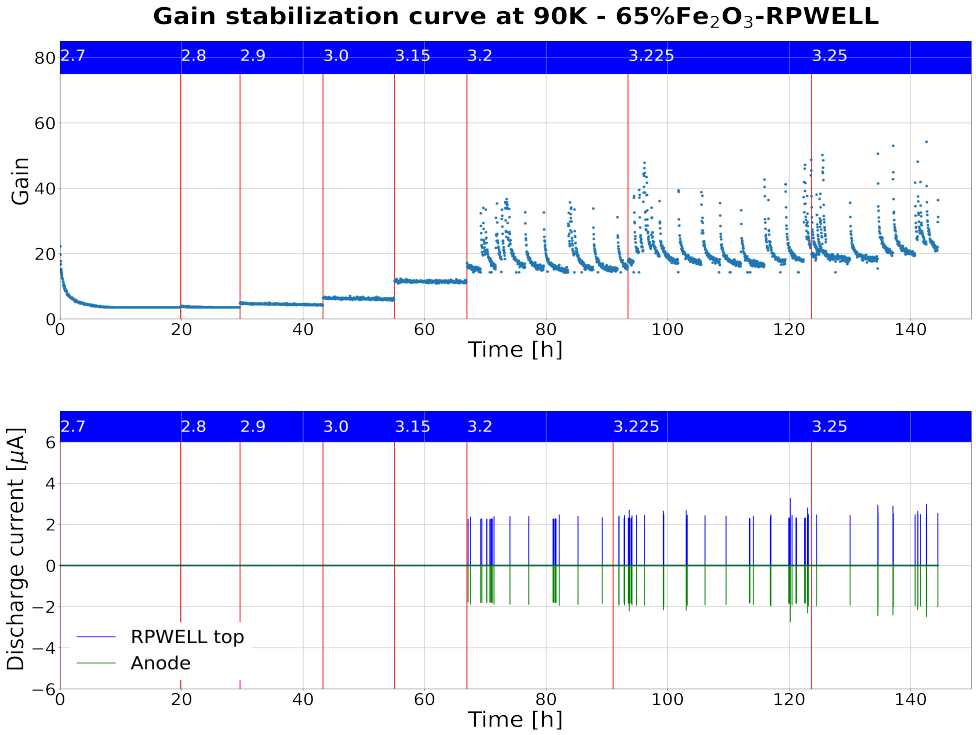

Figure 64: **Top**: Gain stabilization curve over 140 hours for a 65% Fe_2O_3-RPWELL operated at 90 K, 1.2 Bar. **Bottom**: power supply currents recorded from the RPWELL top (blue) and from the anode (green) for a 65% Fe_2O_3-RPWELL operated at 90 K, 1.2 Bar. Presence of discharges from ΔV_{RPWELL} > 3.2kV on.

It is possible to observe the presence of gain instabilities correlated with electrical discharges for ΔV_{RPWELL} > 3.2kV.

ABS-RPWELL, 1.6mm In Fig. 65 top, the gain stabilization curve for the ABS-RPWELL, 1.6 mm thick plate, is presented and in Fig. 65 bottom, the discharge currents registered from the power supply from the RPWELL top and anode are reported in time-correlation.

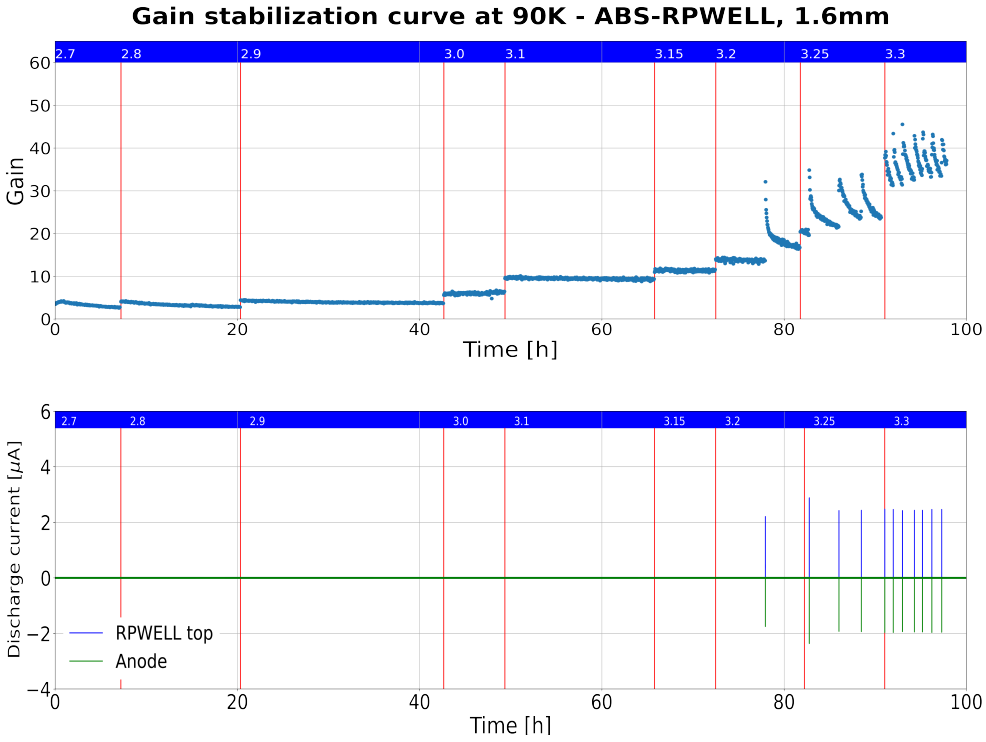

Figure 65: **Top**: Gain stabilization curve over ∼100 hours for a ABS-RPWELL with 1.6 mm thick plate operated at 90 K, 1.2 Bar. **Bottom**: power supply currents recorded from the RPWELL top (blue) and from the anode (green) for the same RPWELL operated in the same conditions. Presence of discharges from $\Delta V_{RPWELL} > 3.2$ kV on.

The same considerations as above apply also for this case. The maximal stable gain achieved with this configuration was G ≈ 11.

ABS-RPWELL, 0.6mm In Fig. 66 top, the gain stabilization curve for the ABS-RPWELL, 0.6 mm thick plate, is presented.

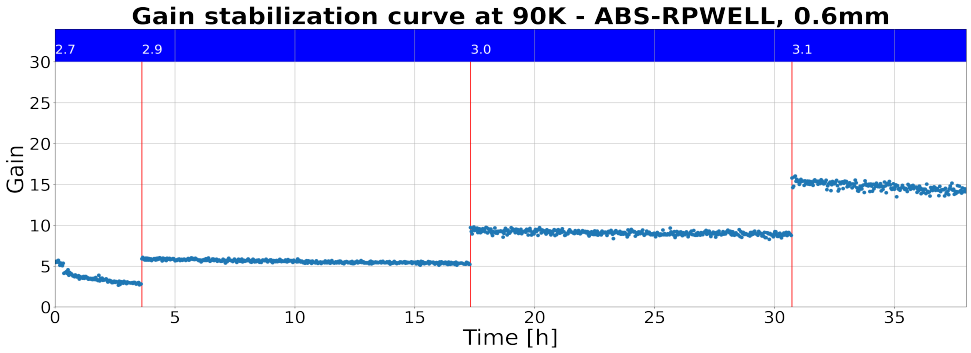

Figure 66: Gain stabilization curve over ~ 35 hours for a ABS-RPWELL with 0.6 mm thick plate operated at 90 K, 1.2 Bar.

The detector was able to operate in discharge-free mode up to $\Delta V_{\mathrm{RPWELL}}$ = 3.1 kV with G ≈ 14 prior to full tripping.

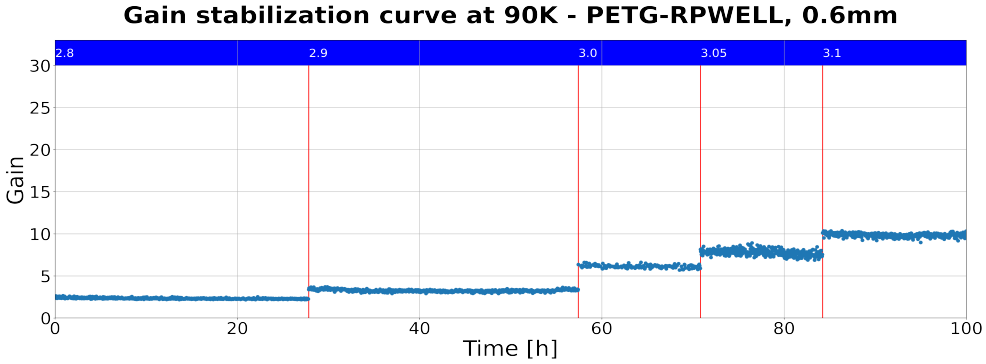

Figure 67: Gain stabilization curve over ~100 hours for a PETG-RPWELL with 0.6mm thick plate operated at 90 K, 1.2 Bar.

PETG-RPWELL, 0.6mm Also in this case, the detector was able to operate in discharge-free mode up to $\Delta V_{\mathrm{RPWELL}}$ = 3.1 kV with G ≈ 11 prior to full tripping.

11 List of publications

1. E. Erdal, L. Arazi, **A. Tesi**, A. Roy, S. Shchemelinin, D. Vartsky and A. Breskin, Recent advances in bubble-assisted Liquid Hole-Multipliers in liquid xenon. 2018 JINST 13 P12008

2. E. Erdal, **A. Tesi**, D. Vartsky, S. Bressler, L. Arazi and A. Breskin, First Imaging Results of a Bubble- assisted Liquid Hole Multiplier with SiPM readout in Liquid Xenon. 2019 JINST 14 P01028

3. E. Erdal, **A. Tesi**, A. Breskin, D. Varsky and S. Bressler, First demonstration of a bubble-assisted liquid-hole multiplier operation in liquid argon, 2019 JINST 14 P11021

4. E. Erdal, L. Arazi, A. Breskin, S. Schemelinin, A. Roy, **A. Tesi**, D. Vartsky and S. Bressler, Bubble-assisted liquid hole multipliers in LXe and LAr : towards "local dual-phase TPCs", 2019 JINST 15 C04002

5. S. Bressler, P. Bhattacharya, A. Breskin, A.E.C. Coimbra, D. Shaked-Renous, **A. Tesi**, L. Moleri, M. Chefdeville, G. Vouters, J. Karyotakis, C. Drancourt, M. Titov, T. Geralis, Novel Resistive-Plate WELL sampling element for (S)DHCAL, 2019 NIM A 958 162861

6. P. Bhattacharya, **A. Tesi**, D. Shaked-Renous, L. Moleri, A. Breskin and S. Bressler, Single electron spectra in RPWELL-based detectors, 2021 JINST 16 P05004

7. **A. Tesi**, E. Segre, S. Leardini, A. Breskin, S. Kapishnikov, L. Moleri, D. Vartsky and S. Bresser, Bubble Dynamics in Liquid Hole Multipliers, 2021 JINST 16 P09003

8. D. Shaked-Renous, F. D. Amaro, P. Bhattacharya, A. Breskin, M. Chefdeville, C. Drancourt, T. Geralis, Y. Karyotakis, L. Moleri, **A. Tesi**, M. Titov, J. Veloso, G. Vouters, S. Bressler, Test-beam and simulation studies towards RPWELL-based DHCAL, 2022 JINST TH 004

9. S. Leardini, Y. Zhou, **A. Tesi**, M. Morales, D. Gonzalez-Diaz, A. Breskin, S. Bressler, L. Moleri, V. Peskov, Diamond-like carbon coatings for cryogenic operation of particle detectors, 2022 NIM A D00988

10. S. Bressler, L. Moleri, A. Jash, **A. Tesi**, D. Zavazieva, The Thick Gas Electron Multiplier and its derivatives: physics, technologies and applications, 2022 Progress in Particle and Nuclear Physics

11. L. Olano-Vegas, I. Pardo, S. Leardini, M. Morales, A. Carreira b, Ruben, **A. Tesi**, S. Bressler, D. Gonzalez-Diaz,F. Guitian, Development of YSZ-Fe2O3 ceramic plates for cryogenic operation of resistive-protected gaseous detectors, 2023 Frontiers in Detector Science and Technology

12. **A. Tesi**, L. Moleri, S. Leardini, A. Breskin, D. Gonzalez-Diaz, L. Olano-Vegas, A. Jash and S. Bressler,, Novel resistive charge-multipliers for dual-phase LAr-TPCs: towards stable operation at higher gain, 2023 JINST C06017

Currently under review/in preparation:

1. **A. Tesi**, S. Leardini, L. Moleri, D. Gonzalez-Diaz, A. Jash, A. Breskin and S. Bressler, The cryogenic RWELL: a stable charge multiplier for dual-phase liquid argon detectors - submitted to EPJC, Arxiv: https://arxiv.org/abs/2307.02343

2. **A. Tesi**, S. Leardini, D. Gonzalez-Diaz, L. Moleri, A. Jash, A. Breskin and S. Bressler, Cryogenic RPWELL: a dual-phase charge readout with discharge-free stable gain - prepared for submission to JINST

12 Bibliography

References

[1] G.S. Karagiorgi, *Current and future liquid argon neutrino experiments*, in *NuINT12: the 8th International Workshop on Neutrino-Nucleus Interactions in the FEW-GeV Region*, vol. 1663 of *American Institute of Physics Conference Series*, p. 100001, May, 2015, DOI.

[2] EXO Collaboration collaboration, *Search for neutrinoless double-beta decay in* ^{136}Xe *with exo-200*, *Phys. Rev. Lett.* **109** (2012) 032505.

[3] C. Rubbia et al., *Underground operation of the ICARUS T600 LAr-TPC: first results*, *JINST* **6** (2011) P07011 [1106.0975].

[4] S. Mihara, *Meg liquid xenon detector*, *Journal of Physics: Conference Series* **308** (2011) 012009.

[5] C. Grignon, J. Barbet, M. Bardiès, T. Carlier, J. Chatal, O. Couturier et al., *Nuclear medical imaging using β+γ coincidences from 44sc radio-nuclide with liquid xenon as detection medium*, *Nuclear Instruments and Methods in Physics Research Section A: Accelerators, Spectrometers, Detectors and Associated Equipment* **571** (2007) 142.

[6] A. Breskin, I. Israelashvili, M. Cortesi, L. Arazi, S. Shchemelinin, R. Chechik et al., *A novel liquid-Xenon detector concept for combined fast-neutrons and gamma imaging and spectroscopy*, *Journal of Instrumentation* **7** (2012) C06008.

[7] D. Vartsky, I. Israelashvili, M. Cortesi, L. Arazi, A. Coimbra, L. Moleri et al., *Liquid-xe detector for contraband detection*, *Nuclear Instruments and Methods in Physics Research Section A: Accelerators, Spectrometers, Detectors and Associated Equipment* **824** (2016) 240.

[8] I. Israelashvili, M. Cortesi, D. Vartsky, L. Arazi, D. Bar, E. Caspi et al., *A comprehensive simulation study of a liquid-xe detector for contraband detection*, *Journal of Instrumentation* **10** (2015) P03030.

[9] V. Chepel and H. Araújo, *Liquid noble gas detectors for low energy particle physics*, *Journal of Instrumentation* **8** (2013) R04001.

[10] V. Lepeltier, *Review on TPC's*, *J. Phys. Conf. Ser.* **65** (2007) 012001.

[11] A. Ereditato and A. Rubbia, *The liquid argon tpc: a powerful detector for future neutrino experiments and proton decay searches*, *Nuclear Physics B - Proceedings Supplements* **154** (2006) 163.

[12] S. Cebriá n, *Review on dark matter searches*, *Journal of Physics: Conference Series* **2502** (2023) 012004.

[13] A. Mastbaum, F. Psihas and J. Zennamo, *Xenon-doped liquid argon TPCs as a neutrinoless double beta decay platform*, *Physical Review D* **106** (2022) .

[14] SBND collaboration, *Status of the Short-Baseline Near Detector at Fermilab*, *PoS* **NuFact2021** (2022) 184.

[15] S. Vagnozzi, L. Visinelli, P. Brax, A.-C. Davis and J. Sakstein, *Direct detection of dark energy: The xenon1t excess and future prospects*, *Phys. Rev. D* **104** (2021) 063023.

[16] P. Hamilton, *First measurement of neutrino interactions in microboone*, 2016.

[17] R. Acciarri, M.A. Acero, M. Adamowski, C. Adams, P. Adamson, S. Adhikari et al., *Long-baseline neutrino facility (lbnf) and deep underground neutrino experiment (dune) conceptual design report, volume 4 the dune detectors at lbnf*, 2016.

[18] E. Aprile and T. Doke, *Liquid xenon detectors for particle physics and astrophysics*, *Reviews of Modern Physics* **82** (2010) 2053.

[19] T. Igarashi, M. Tanaka, T. Washimi and K. Yorita, *Performance of VUV-sensitive MPPC for liquid argon scintillation light*, *Nuclear Instruments and Methods in Physics Research Section A: Accelerators, Spectrometers, Detectors and Associated Equipment* **833** (2016) 239.

[20] A. Bondar, A. Buzulutskov, A. Dolgov, E. Shemyakina and A. Sokolov, *MPPC versus MRS APD in two-phase Cryogenic Avalanche Detectors*, *JINST* **10** (2015) P04013 [1502.03663].

[21] A. Roy, M. Morales, I. Israelashvili, A. Breskin, S. Bressler, D. Gonzalez-Diaz et al., *First results of Resistive-Plate Well (RPWELL) detector operation at 163 K*, *JINST* **14** (2019) P10014 [1907.05057].

[22] L. Arazi, A. Coimbra, E. Erdal, I. Israelashvili, M. Rappaport, S. Shchemelinin et al., *First results of a large-area cryogenic gaseous photomultiplier coupled to a dual-phase liquid xenon TPC*, *Journal of Instrumentation* **10** (2015) P10020.

[23] E. Aprile and X. collaboration, *The xenon1t dark matter search experiment*, 2012.

[24] D. Akerib, X. Bai, S. Bedikian, E. Bernard, A. Bernstein, A. Bolozdynya et al., *The large underground xenon (lux) experiment*, *Nuclear Instruments and Methods in Physics Research Section A: Accelerators, Spectrometers, Detectors and Associated Equipment* **704** (2013) 111.

[25] Y. Yang, *Search for dark matter from the first data of the pandax-ii experiment*, 2016.

[26] A. Marchionni, C. Amsler, A. Badertscher, V. Boccone, A. Bueno, M.C. Carmona-Benitez

et al., *ArDM: a ton-scale LAr detector for direct dark matter searches*, *Journal of Physics: Conference Series* **308** (2011) 012006.

[27] C.E. Aalseth, F. Acerbi, P. Agnes, I.F.M. Albuquerque, T. Alexander, A. Alici et al., *DarkSide-20k: A 20 tonne two-phase LAr TPC for direct dark matter detection at LNGS*, *The European Physical Journal Plus* **133** (2018) .

[28] A. Badertscher, A. Curioni, U. Degunda, L. Epprecht, A. Gendotti, S. Horikawa et al., *First operation and performance of a 200 lt double phase LAr LEM-TPC with a 40 × 76 cmsup2/supreadout*, *Journal of Instrumentation* **8** (2013) P04012.

[29] C. Cuesta, *Status of protodune dual phase*, 2019.

[30] E. Erdal, *Development of novel concepts of noble-liquid detectors for rare-event searches*, Ph.D. thesis, Weizmann Institute of Science, 2021.

[31] J. Aalbers, F. Agostini, M. Alfonsi, F. Amaro, C. Amsler, E. Aprile et al., *DARWIN: towards the ultimate dark matter detector*, *Journal of Cosmology and Astroparticle Physics* **2016** (2016) 017.

[32] A. Breskin, *Novel electron and photon recording concepts in noble-liquid detectors*, *Journal of Instrumentation* **17** (2022) P08002.

[33] A. Marchionni, D. Autiero, D. Duchesneau and F. Cavalier, "Status of the dune project." http://atrium.in2p3.fr/nuxeo/nxpath/default/Atrium/sections/Public/CSI/Conseil%20Scientifique%20Oct/Rapports/7-Docs-DUNE-Marchianni-A@view_documents?page=galaxy%2Fprint&conversationId=0NXMAIN11,, 2021.

[34] M. Berger, J. Hubbel, S. Seltzer, J. Chang, J. Coursey, R. Sukumar et al., *Xcom: Photon cross section database (version 1.5)*, 2010.

[35] S.K. Allison and S.D. Warshaw, *Passage of heavy particles through matter*, *Rev. Mod. Phys.* **25** (1953) 779.

[36] *NIST Chemistry WebBook*, World Scientific.

[37] V. Solovov, V. Chepel, M. Lopes, A. Hitachi, R.F. Marques and A. Policarpo, *Measurement of the refractive index and attenuation length of liquid xenon for its scintillation light*, *Nuclear Instruments and Methods in Physics Research Section A: Accelerators, Spectrometers, Detectors and Associated Equipment* **516** (2004) 462.

[38] M. Babicz, S. Bordoni, T. Cervi, Z. Collins, A. Fava, A. Ferrari et al., *Propagation of scintillation light in liquid argon*, *Journal of Instrumentation* **15** (2020) C03035.

[39] E. Aprile, H. Contreras, L.W. Goetzke, A.J. Melgarejo Fernandez, M. Messina, J. Naganoma et al., *Measurements of proportional scintillation and electron multiplication in liquid xenon using thin wires*, *JINST* **9** (2014) P11012 [1408.6206].

[40] A. Buzulutskov, *Electroluminescence and electron avalanching in two-phase detectors*, *Instruments* **4** (2020) 16.

[41] J. Kim, S. Dardin, R. Kadel, J. Kadyk, V. Peskov and W. Wenzel, *Electron avalanches in*

liquid argon mixtures, *Nuclear Instruments and Methods in Physics Research Section A: Accelerators, Spectrometers, Detectors and Associated Equipment* **534** (2004) 376.

[42] E. Aprile, J. Aalbers, F. Agostini, M. Alfonsi, L. Althueser, F. Amaro et al., *Excess electronic recoil events in XENON1t*, *Physical Review D* **102** (2020) .

[43] A. Bolozdynya, *Emission Detectors*, World Scientific (2010).

[44] A. Bondar, A. Buzulutskov, A. Grebenuk, D. Pavlyuchenko and Y. Tikhonov, *Electron emission properties of two-phase argon and argon-nitrogen avalanche detectors*, *Journal of Instrumentation* **4** (2009) P09013.

[45] A. Buzulutskov and A. Bondar, *Electric and photoelectric gates for ion backflow suppression in multi-GEM structures*, *Journal of Instrumentation* **1** (2006) P08006.

[46] P. Jeanneret, *Time Projection Chambers and detection of neutrinos*, Ph.D. thesis, Neuchatel U., 2001.

[47] L. Periale, V. Peskov, P. Carlson, C. Iacobaeus, T. Francke, N. Pavlopoulos et al., *Evaluation of various planar gaseous detectors with CsI photocathodes for the detection of primary scintillation light from noble gases*, *Nucl. Instrum. Meth. A* **497** (2003) 242 [physics/0106070].

[48] R. CHECHIK, A. BRESKIN, C. SHALEM and D. MORMANN, *Thick GEM-like hole multipliers: properties and possible applications*, *Nuclear Instruments and Methods in Physics Research Section A: Accelerators, Spectrometers, Detectors and Associated Equipment* **535** (2004) 303.

[49] S. Bressler, L. Moleri, A. Jash, A. Tesi and D. Zavazieva, *The thick gas electron multiplier and its derivatives: Physics, technologies and applications*, *Progress in Particle and Nuclear Physics* **130** (2023) 104029.

[50] M. Alexeev et al., *Detection of single photons with hybrid ThickGEM-based counters*, *PoS* **PhotoDet2012** (2012) 057.

[51] A. Breskin, R. Alon, M. Cortesi, R. Chechik, J. Miyamoto, V. Dangendorf et al., *A concise review on THGEM detectors*, *Nuclear Instruments and Methods in Physics Research Section A: Accelerators, Spectrometers, Detectors and Associated Equipment* **598** (2009) 107.

[52] R. Chechik and A. Breskin, *Advances in gaseous photomultipliers*, *Nuclear Instruments and Methods in Physics Research Section A: Accelerators, Spectrometers, Detectors and Associated Equipment* **595** (2008) 116.

[53] F. Tessarotto, *Evolution and recent developments of the gaseous photon detectors technologies*, *Nuclear Instruments and Methods in Physics Research Section A: Accelerators, Spectrometers, Detectors and Associated Equipment* **912** (2018) 278.

[54] R. Alon, J. Miyamoto, M. Cortesi, A. Breskin, R. Chechik, I. Carne et al., *Operation of a thick gas electron multiplier (THGEM) in ar, xe and ar-xe*, *Journal of Instrumentation* **3** (2008) P01005.

[55] R. Chechik, A. Breskin and C. Shalem, *Thick GEM-like multipliers—a simple solution for large area UV-RICH detectors*, *Nuclear Instruments and Methods in Physics Research Section A: Accelerators, Spectrometers, Detectors and Associated Equipment* **553** (2005) 35.

[56] C. Cantini, L. Epprecht, A. Gendotti, S. Horikawa, L. Periale, S. Murphy et al., *Performance study of the effective gain of the double phase liquid argon LEM time projection chamber*, *Journal of Instrumentation* **10** (2015) P03017.

[57] C.K. Shalem, R. Chechik, A. Breskin, K. Michaeli and N. Ben-Haim, *Advances in thick GEM-like gaseous electron multipliers. Part II: Low-pressure operation*, *Nucl. Instrum. Meth. A* **558** (2006) 468 [physics/0601119].

[58] A. Buzulutskov, *Advances in Cryogenic Avalanche Detectors (review)*, *JINST* **7** (2012) C02025 [1112.6153].

[59] I. Israelashvili, A.E.C. Coimbra, D. Vartsky, L. Arazi, S. Shchemelinin, E.N. Caspi et al., *Fast-neutron and gamma-ray imaging with a capillary liquid xenon converter coupled to a gaseous photomultiplier*, *JINST* **12** (2017) P09029 [1707.04794].

[60] L. Arazi, M. Pitt, S. Bressler, L. Moleri, A. Rubin and A. Breskin, *Laboratory studies of THGEM-based WELL structures with resistive anode*, *Journal of Instrumentation* **9** (2014) P04011.

[61] A. Rubin, L. Arazi, S. Bressler, L. Moleri, M. Pitt and A. Breskin, *First studies with the resistive-plate WELL gaseous multiplier*, *Journal of Instrumentation* **8** (2013) P11004.

[62] A. Jash, L. Moleri and S. Bressler, *Electrical breakdown in thick-gem based well detectors*, *Journal of Instrumentation* **17** (2022) P11004.

[63] L. Arazi, , C.D.R. Azevedo, A. Breskin, S. Bressler, L. Moleri et al., *Beam studies of the segmented resistive WELL: A potential thin sampling element for digital hadron calorimetry*, *Nuclear Instruments and Methods in Physics Research Section A: Accelerators, Spectrometers, Detectors and Associated Equipment* **732** (2013) 199.

[64] G. Bencivenni, R.D. Oliveira, G. Morello and M.P. Lener, *The micro-resistive well detector: a compact spark-protected single amplification-stage mpgd*, *Journal of Instrumentation* **10** (2015) P02008.

[65] A. Badertscher, L. Knecht, M. Laffranchi, D. Lussi, A. Marchionni, G. Natterer et al., *Operation of a double-phase pure argon large electron multiplier time projection chamber: Comparison of single and double phase operation*, *Nuclear Instruments and Methods in Physics Research Section A: Accelerators, Spectrometers, Detectors and Associated Equipment* **617** (2010) 188.

[66] A. Badertscher, L. Knecht, M. Laffranchi, A. Marchionni, G. Natterer, P. Otiougova et al., *Construction and operation of a double phase lar large electron multiplier time projection chamber*, .

[67] A. Badertscher, A. Curioni, S. Horikawa, L. Knecht, D. Lussi, A. Marchionni et al., *Stable*

operation with gain of a double phase Liquid Argon LEM-TPC with a 1 mm thick segmented LEM, *J. Phys. Conf. Ser.* **308** (2011) 012016 [1010.2482].

[68] A. Badertscher et al., *First operation and performance of a 200 lt double phase LAr LEM-TPC with a 40x76 cm^2 readout*, *JINST* **8** (2013) P04012 [1301.4817].

[69] D. Lussi, *Study of the response of the novel LAr LEM-TPC detector exposed to cosmic rays and a charged particle beam*, Ph.D. thesis, Zurich, ETH, 2013. 10.3929/ethz-a-010008070.

[70] D. Gonzalez-Diaz, F. Monrabal and S. Murphy, *Gaseous and dual-phase time projection chambers for imaging rare processes*, *Nucl. Instrum. Meth. A* **878** (2018) 200 [1710.01018].

[71] F. Resnati, A. Badertscher, A. Curioni, S. Horikawa, L. Knecht, D. Lussi et al., *Stable operation with gain of a double phase liquid argon LEM-TPC with a 1 mm thick segmented LEM*, *Journal of Physics: Conference Series* **308** (2011) 012016.

[72] A. Breskin, *Liquid hole-multipliers: A potential concept for large single-phase noble-liquid tpcs of rare events*, *Journal of Physics: Conference Series* **460** (2013) 012020.

[73] L. Arazi, E. Erdal, A. Coimbra, M. Rappaport, D. Vartsky, V. Chepel et al., *Liquid hole multipliers: bubble-assisted electroluminescence in liquid xenon*, *Journal of Instrumentation* **10** (2015) P08015.

[74] L. Arazi, A.E.C. Coimbra, R. Itay, H. Landsman, L. Levinson, B. Pasmantirer et al., *First observation of liquid-xenon proportional electroluminescence in THGEM holes*, *Journal of Instrumentation* **8** (2013) C12004.

[75] E. Erdal, L. Arazi, M. Rappaport, S. Shchemelinin, D. Vartsky and A. Breskin, *First demonstration of vuv-photon detection in liquid xenon with thgem and gem-based liquid hole multipliers*, *Nuclear Instruments and Methods in Physics Research Section A: Accelerators, Spectrometers, Detectors and Associated Equipment* **845** (2017) 218.

[76] F. Sauli, *Gem: A new concept for electron amplification in gas detectors*, *Nuclear Instruments and Methods in Physics Research Section A: Accelerators, Spectrometers, Detectors and Associated Equipment* **386** (1997) 531.

[77] E. Erdal, A. Tesi, D. Vartsky, S. Bressler, L. Arazi and A. Breskin, *First imaging results of a bubble-assisted liquid hole multiplier with SiPM readout in liquid xenon*, *Journal of Instrumentation* **14** (2019) P01028.

[78] S. Bressler, L. Arazi, L. Moleri, M. Pitt, A. Rubin and A. Breskin, *Recent advances with THGEM detectors*, *Journal of Instrumentation* **8** (2013) C12012.

[79] A. Tesi, L. Moleri, S. Leardini, A. Breskin, D. Gonzalez-Diaz, L. Olano-Vegas et al., *Novel resistive charge-multipliers for dual-phase lar-tpcs: towards stable operation at higher gains*, *Journal of Instrumentation* **18** (2023) C06017.

[80] A. Marchionni, *Status and new ideas regarding liquid argon detectors*, *Annual Review of Nuclear and Particle Science* **63** (2013) 269.

[81] E. Erdal, L. Arazi, V. Chepel, M.L. Rappaport, D. Vartsky and A. Breskin, *Direct*

observation of bubble-assisted electroluminescence in liquid xenon, 2015. 10.48550/ARXIV.1509.02354.

[82] E. Erdal, A. Tesi, A. Breskin, D. Vartsky and S. Bressler, *First demonstration of a bubble-assisted liquid hole multiplier operation in liquid argon*, *Journal of Instrumentation* **14** (2019) P11021.

[83] E. Erdal, L. Arazi, A. Tesi, A. Roy, S. Shchemelinin, D. Vartsky et al., *Recent advances in bubble-assisted liquid hole-multipliers in liquid xenon*, *Journal of Instrumentation* **13** (2018) P12008.

[84] C. Amsler, V. Boccone, A. Büchler, R. Chandrasekharan, C. Regenfus and J. Rochet, *Luminescence quenching of the triplet excimer state by air traces in gaseous argon*, *Journal of Instrumentation* **3** (2008) P02001.

[85] A. Tesi, E. Segre, S. Leardini, A. Breskin, S. Kapishnikov, L. Moleri et al., *Bubble dynamics in liquid hole multipliers*, *Journal of Instrumentation* **16** (2021) P09003.

[86] D.A. Saville, *Electrohydrodynamics: The taylor-melcher leaky dielectric model*, *Annual Review of Fluid Mechanics* **29** (1997) 27 [https://doi.org/10.1146/annurev.fluid.29.1.27].

[87] Y. Lin, P. Skjetne and A. Carlson, *A phase field model for multiphase electro-hydrodynamic flow*, *International Journal of Multiphase Flow* **45** (2012) 1.

[88] P. Concus, *Static menisci in a vertical right circular cylinder*, *Journal of Fluid Mechanics* **34** (1968) 481–495.

[89] F. Heib and M. Schmitt, *Statistical contact angle analyses with the high-precision drop shape analysis (hpdsa) approach: Basic principles and applications*, *Coatings* **6** (2016) .

[90] A. Stalder, G. Kulik, D. Sage, L. Barbieri and P. Hoffmann, *A snake-based approach to accurate determination of both contact points and contact angles*, *Colloids and Surfaces A: Physicochemical and Engineering Aspects* **286** (2006) 92.

[91] C.A. Schneider, W.S. Rasband and K.W. Eliceiri, *Nih image to imagej: 25 years of image analysis*, *Nat Meth* **9** (2012) 671.

[92] D.Y. Kwok, T. Gietzelt, K. Grundke, H.-J. Jacobasch and A.W. Neumann, *Contact angle measurements and contact angle interpretation. 1. contact angle measurements by axisymmetric drop shape analysis and a goniometer sessile drop technique*, *Langmuir* **13** (1997) 2880 [https://doi.org/10.1021/la9608021].

[93] M. Miyama, Y. Yang, T. Yasuda, T. Okuno and H.K. Yasuda, *Static and dynamic contact angles of water on polymeric surfaces*, *Langmuir* **13** (1997) 5494 [https://doi.org/10.1021/la960870n].

[94] E.L. Ritman, *Micro-computed tomography—current status and developments*, *Annual Review of Biomedical Engineering* **6** (2004) 185 [https://doi.org/10.1146/annurev.bioeng.6.040803.140130].

[95] L.M. Lander, L.M. Siewierski, W.J. Brittain and E.A. Vogler, *A systematic comparison of*

contact angle methods, *Langmuir* **9** (1993) 2237 [https://doi.org/10.1021/la00032a055].

[96] J. Drelich, *Guidelines to measurements of reproducible contact angles using a sessile-drop technique*, *Surface Innovations* **1** (2013) 248 [https://doi.org/10.1680/si.13.00010].

[97] Suwarno, T. Widyanugraha, P.H. Didit and Suharto, *Dielectric properties of silicone oil, natural ester, and mineral oil under accelerated thermal aging*, .

[98] *Silicone oil properties*, .

[99] V. Parkhomchuck, Y. Pestov and N. Petrovykh, *A spark counter with large area*, *Nuclear Instruments and Methods* **93** (1971) 269.

[100] R. Santonico and R. Cardarelli, *Development of resistive plate counters*, *Nuclear Instruments and Methods in Physics Research* **187** (1981) 377.

[101] P. Fonte, A. Smirnitski and M. Williams, *A new high-resolution tof technology*, *Nuclear Instruments and Methods in Physics Research Section A: Accelerators, Spectrometers, Detectors and Associated Equipment* **443** (2000) 201.

[102] M. Dixit and A. Rankin, *Simulating the charge dispersion phenomena in micro pattern gas detectors with a resistive anode*, *Nuclear Instruments and Methods in Physics Research Section A: Accelerators, Spectrometers, Detectors and Associated Equipment* **566** (2006) 281.

[103] W. Riegler, *Electric fields, weighting fields, signals and charge diffusion in detectors including resistive materials*, *Journal of Instrumentation* **11** (2016) P11002.

[104] D. Attié, M. Batkiewicz-Kwasniak, J. Boix, S. Bolognesi, S. Bordoni, D. Calvet et al., *Performances of a resistive micromegas module for the time projection chambers of the t2k near detector upgrade*, *Nuclear Instruments and Methods in Physics Research Section A: Accelerators, Spectrometers, Detectors and Associated Equipment* **957** (2020) 163286.

[105] I. Giomataris, M. Gros, I. Katsioulas, P. Knights, J.-P. Mols, T. Neep et al., *A resistive achinos multi-anode structure with dlc coating for spherical proportional counters*, *Journal of Instrumentation* **15** (2020) P11023.

[106] R. Bouclier, M. Capeáns, G. Million, L. Ropelewski, F. Sauli, T. Temmel et al., *High rate operation of micro-strip gas chambers on diamond-coated glass*, *Nuclear Instruments and Methods in Physics Research Section A: Accelerators, Spectrometers, Detectors and Associated Equipment* **369** (1996) 328.

[107] Y. Lv, Y. Zhou, J. Liu, M. Shao, Z. Zhang, G. Song et al., *Production and performance study of Diamond-Like Carbon resistive electrode in MPGD*, *Nucl. Instrum. Meth. A* **958** (2020) 162759.

[108] A.A. Abud, B. Abi, R. Acciarri, M.A. Acero, G. Adamov, D. Adams et al., *Deep underground neutrino experiment (dune) near detector conceptual design report*, *Instruments* **5** (2021) .

[109] T. Francke, P. Fonte, V. Peskov and J. Rantanen, *Potential of rpcs for tracking*, *Nuclear Instruments and Methods in Physics Research Section A: Accelerators, Spectrometers, Detectors and Associated Equipment* **508** (2003) 83.

[110] G. Bencivenni, R. De Oliveira, G. Felici, M. Gatta, G. Morello, A. Ochi et al., *Performance of μ-RWELL detector vs resistivity of the resistive stage*, *Nucl. Instrum. Meth. A* **886** (2018) 36.

[111] H. Ito, *Optical transmittance measurements of sheet resistors for the* CF_4 *scintillating light in a gaseous time-projection chamber*, .

[112] D. Gonzalez-Diaz and A. Sharma, *Challenges for resistive gaseous detectors towards rpc2014*, *Journal of Instrumentation* **8** (2013) T02001.

[113] S. Leardini, Y. Zhou, A. Tesi, M. Morales, D. González-Díaz, A. Breskin et al., *Diamond-like carbon coatings for cryogenic operation of particle detectors*, *Nuclear Instruments and Methods in Physics Research Section A: Accelerators, Spectrometers, Detectors and Associated Equipment* **1049** (2023) 168104.

[114] I. Miccoli, F. Edler, H. Pfnür and C. Tegenkamp, *The 100th anniversary of the four-point probe technique: the role of probe geometries in isotropic and anisotropic systems*, *Journal of Physics: Condensed Matter* **27** (2015) 223201.

[115] A.L.E. Boris I. Shklovskii, *Electronic properties of doped semiconductors*, .

[116] L. Olano-Vegas et al., *Development of* Fe_2O_3*/YSZ ceramic plates for cryogenic operation of resistive-protected gaseous detectors*, 2305.12899.

[117] M. Morales, C. Pecharroman, G. Mata-Osoro, L.A. Diaz and J.A. Garzon, *Conductivity and charge depletion aging of resistive electrodes for high rate RPCs*, *JINST* **8** (2013) P01022.

[118] R. Bitter, T. Mohiuddin and M. Nawrocki, *LabVIEW: Advanced programming techniques*, Crc Press (2006).

[119] J.F. Ziegler, M. Ziegler and J. Biersack, *Srim - the stopping and range of ions in matter (2010)*, *Nuclear Instruments and Methods in Physics Research Section B: Beam Interactions with Materials and Atoms* **268** (2010) 1818.

[120] H. Tawara, N. Ishida, J. Kikuchi and T. Doke, *Measurements of the w values in argon, nitrogen, and methane for 0.93 to 5.3 mev alpha particles*, *Nuclear Instruments and Methods in Physics Research Section B: Beam Interactions with Materials and Atoms* **29** (1987) 447.

[121] W. Riegler, *Electric fields, weighting fields, signals and charge diffusion in detectors including resistive materials*, *Journal of Instrumentation* **11** (2016) P11002.

[122] K. Majumdar and K. Mavrokoridis, *Review of Liquid Argon Detector Technologies in the Neutrino Sector*, *Appl. Sciences* **11** (2021) 2455 [2103.06395].

[123] J. Miyamoto, A. Breskin and V. Peskov, *Gain limits of a thick gem in high-purity ne, ar and xe*, *Journal of Instrumentation* **5** (2010) P05008.

[124] D.S. Renous, A. Roy, A. Breskin and S. Bressler, *Gain stabilization in micro pattern gaseous detectors: methodology and results*, *Journal of Instrumentation* **12** (2017) P09036.

[125] M. Pitt, P. Correia, S. Bressler, A. Coimbra, D.S. Renous, C. Azevedo et al., *Measurements of charging-up processes in THGEM-based particle detectors*, *Journal of Instrumentation* **13** (2018) P03009.

[126] S. Biagi, *Monte carlo simulation of electron drift and diffusion in counting gases under the influence of electric and magnetic fields*, *Nuclear Instruments and Methods in Physics Research Section A: Accelerators, Spectrometers, Detectors and Associated Equipment* **421** (1999) 234.

[127] D. Herrera, *Study of columnar recombination in xe+trymethilamine mixtures using a micromegas-tpc*, p. 057, 07, 2015, DOI.

[128] P. Fonte, V. Peskov and F. Sauli, *Feedback and breakdown in parallel plate chambers*, *Nucl. Instrum. Meth. A* **305** (1991) 91.

[129] V. Peskov, M. Cortesi, R. Chechik and A. Breskin, *Further evaluation of a THGEM UV-photon detector for RICH - comparison with MWPC*, *JINST* **5** (2010) P11004 [1008.0151].

[130] P. Bhattacharya, L. Moleri and S. Bressler, *Signal Formation in THGEM-like Detectors*, *Nucl. Instrum. Meth. A* **916** (2019) 125 [1810.12597].

[131] S. Wu, *Study of alternative double phase LAr TPC charge readout systems*, Ph.D. thesis, Zurich, ETH, 2017. 10.3929/ethz-b-000172413.

[132] P. Chiggiato, *Outgassing properties of vacuum materials for particle accelerators*, 2006.07124.

[133] G. Song, M. Shao, L. Shang, Y. Zhou, Y. Lv, X. Wang et al., *Production and properties of a charging-up "free" thgem with dlc coating*, *Nuclear Instruments and Methods in Physics Research Section A: Accelerators, Spectrometers, Detectors and Associated Equipment* **966** (2020) 163868.

[134] R. Veenhof, *Garfield, recent developments*, *Nuclear Instruments and Methods in Physics Research Section A: Accelerators, Spectrometers, Detectors and Associated Equipment* **419** (1998) 726.

[135] *Garfield++*, .

[136] S. Wu, *Study of alternative double phase LAr TPC charge readout systems*, Ph.D. thesis, Zurich, ETH, 2017. 10.3929/ethz-b-000172413.

[137] *Srim - the stopping and range of ions in matter*, .

[138] *Comsol - software for multiphysics simulation*, .

[139] S. Biagi, *Magboltz*, .

[140] E. Erdal, L. Arazi, A. Breskin, S. Shchemelinin, A. Roy, A. Tesi et al., *Bubble-assisted liquid hole multipliers in LXe and LAr: towards "local dual-phase TPCs"*, *Journal of Instrumentation* **15** (2020) C04002.

[141] J.F. READY, *CHAPTER 16 - APPLICATIONS FOR MATERIAL REMOVAL: DRILLING, CUTTING, ELECTRONIC COMPONENT FABRICATION, MARKING*, Academic Press (1978), https://doi.org/10.1016/B978-0-12-583960-0.50022-8.

[142] P. Bhattacharya, A. Tesi, D. Shaked-Renous, L. Moleri, A. Breskin and S. Bressler, *Single-electron spectra in RPWELL-based detectors*, *Journal of Instrumentation* **16** (2021) P05004.

[143] S. Bressler, P. Bhattacharya, A. Breskin, A. Coimbra, D. Shaked-Renous, A. Tesi et al., *Novel resistive-plate WELL sampling element for (s)DHCAL*, *Nuclear Instruments and Methods in Physics Research Section A: Accelerators, Spectrometers, Detectors and Associated Equipment* **958** (2020) 162861.

[144] D. Shaked-Renous, F.D. Amaro, P. Bhattacharya, A. Breskin, M. Chefdeville, C. Drancourt et al., *Test-beam and simulation studies towards rpwell-based dhcal*, 2022. 10.48550/ARXIV.2208.12846.

[145] E. Segre, "Geogebra: Equilibrium model for a bubble trapped underneath a hole." https://www.geogebra.org/m/ezqnenfg, Apr., 2021.